## ABSTRACT

## TWO-DIMENSIONAL REFLECTIVITY POLARIZATION ELASTOMETRY IMAGING TECHNIQUES (PIET) OF SOFT TISSUE

**by**
**Hee Chuan Lim**

A non-invasive polarized light reflection measurement method to measure the stretch of soft tissue, such as skin, is described. The technique utilizes changes in the reflectivity of polarized light intensity as a monitor of skin stretch. Measurements on in-vitro pigskin and in-vivo human skin show that the reflectivity of polarized light intensity increases linearly with stretch over a range. The changes in diffusive reflectivity properties of skin result from the alterations that take place in the roughness across the thickness of the skin layers due to stretch. Conceptually, as the roughness of a layer decreases with stretch, a smoother reflecting media is produced resulting in a proportional increase in the specular reflection. Results can be easily extended to a real time stretch analysis of large tissue areas that would be applicable for mapping the stretch of skin. Simple one- and two-dimensional sinusoidal theoretical surface roughness model correctly predicts the experimental measurements. In-vitro pigskins were also used for the tissue burn experiments and its measured reflectivity slope versus stretch increases with the burn duration up to a limited thermal excitation. Above this limit, the in-vitro sample becomes optically transparent, as its biomechanical properties is thermally altered and a negative reflectivity slope is observed.

# TWO-DIMENSIONAL REFLECTIVITY POLARIZATION ELASTOMETRY IMAGING TECHNIQUES (PIET) OF SOFT TISSUE

**By**
**Hee Chuan Lim**

**A Dissertation**
**Submitted to the Faculty of**
**New Jersey Institute of Technology and**
**Rutgers, The State University of New Jersey - Newark**
**In Partially Fulfillment of the Requirement for the Degree of**
**Doctor of Philosophy in Applied Physics**

**Federated Department of Physics**

**May 2002**

**APPROVAL PAGE**

**TWO-DIMENSIONAL REFLECTIVITY POLARIZATION ELASTOMETRY IMAGING TECHNIQUES (PIET) OF SOFT TISSUE**

**Hee Chuan Lim**

Dr. John F. Federici, Dissertation Advisor — Date
Associate Chair and Professor of Applied Physics Department, NJIT
Professor of Biomedical Engineering Department, NJIT

Dr. Robert B. Barat, Committee Member — Date
Professor of Chemical Engineering Department, NJIT

Dr. Avid Kamgar, Committee Member — Date
Research Associate Professor of Applied Physics, NJIT

Dr. Gordon A. Thomas, Committee Member — Date
Distinguished Professor of Applied Physics Department, NJIT
Professor of Biomedical Engineering Department, NJIT

Dr. Nejat Guzelsu, Committee Member — Date
Professor of Osteosciences, Robert Wood Johnson Medical School,
UMDNJ-New Brunswick

## BIOGRAPHICAL SKETCH

**Author:** Hee Chuan Lim

**Degree:** Doctor of Philosophy

**Date:** May 2002

**Undergraduate and Graduate Education:**

- Doctor of Philosophy in Applied Physics,
  New Jersey Institute of Technology and
  Rutgers, The State University of New Jersey, Newark, NJ, May 2002

- Master of Science in Physics
  Western Illinois University, Macomb, IL, May 1997

- Bachelor of Science in Microelectronics and Physics,
  Campbell University, Buies Creek, NC, May 1994

**Major:** Applied Physics

**Presentation and Publications:**

Federici JF, Guzelsu N, Lim HC, Jannuzzi G, Findley T, Chaudhry H R, Ritter AB, "Non-invasive Light Reflection Technique for Measuring Soft-Tissue Stretch", Appl. Optics vol. 38 no. 31, 6655-6668 (1999)

Hee C. Lim, John F. Federici
"Polarization Imaging Elastometry Techniques Spatial Resolution of Soft-Tissue Stretch", 1999 Summer Seminar Series of the New Jersey Center for Biomaterials. A Cooperative Research Initiative Sponsored by UMDNJ, New Jersey's University of the Health Sciences, Rutgers, The State University of New Jersey, New Jersey Institute of Technology in coordination with Princeton University with support from the New Jersey Commission on Science and Technology

Hee C. Lim, John F. Federici
"Spatial and Stretch Resolution of Soft-Tissue Stretch by 2-D Polarization Imaging", Ninth Annual UNI-TECH Conference Sponsored by SAMPE, AICHE and SPS, Biomedical and Biomedical Applications, Best Paper Award APR 2000

Hee C. Lim, Nejat Guzelsu, John F. Federici, Tom Findley, and Art B. Ritter, "Measurement of Skin Stretch via Light Reflection" (Submitted to Journal of Biophotonics)

Hee C. Lim, G. Jannuzzi, J. F. Federici, and N. Guzelsu, "Spatial and Stretch Resolution of Soft-Tissue Stretch by Polarization Imaging" (Submitted to Applied Optics)

Dedicated to

my beloved wife, *Yew Fong Hor,*

and to

my late grandmother, parent, brother and sister.

## ACKNOWLEGEMENT

I would like to express my appreciation and thanks to Dr. John Federici, who as my mentor not only served as my dissertation Advisor, providing insightful and intuitive suggestion, but also gave me support and encouragement throughout my tenure here.

I am thankful and grateful for the following people who facilitated and assisted my research; Dr. Jan Opyrchal and Mr. Herminio Ramirez for their expertise and help in the machine laboratory, and Dr. Nejat Guzelsu, who resided in my dissertation Committee, for his valuable, and informative discussion; Mrs. Renee Crawley and Mrs. Leslie Williams for their generous help; My fellow Ph.D graduate students from the physics department, who all participated in my research with their body parts in the name of science.

In addition to Dean Ronald Kane for his continuing support and assurance when the road ahead was unlit and uncertain. Special thanks are given to Dr. Robert Barat, Dr. Avid Kamgar, and Dr. Gordon Thomas, for actively participating in my research and serving in my dissertation Committee.

## TABLE OF CONTENTS

## TABLE OF CONTENTS
## (Continued)

## TABLE OF CONTENTS
## (Continued)

## LIST OF TABLES

## LIST OF FIGURES

## LIST OF FIGURES
## (Continued)

**Figure** **Page**

## LIST OF FIGURES
## (Continued)

**Figure** **Page**

## LIST OF FIGURES
## (Continued)

# CHAPTER 1

# PROLOGUE

## 1.1 Introduction

The dissertation presents a simple theory and applications of polarized light interaction with in-vitro and in-vivo soft tissue. In recent years of biomedical engineering research and development, photonics propagation in tissue, its reflectivity, and the resulting photothermal response has received considerable attention owning to the increased number of diagnostic and therapeutic applications of lasers in medicine.[1] This dissertation introduces a new diagnostic technique, polarization elastometry imaging.[2] The technique extends the 2-Dimensional polarization imaging[3] to examine mechanical properties of soft tissue. In order to address these issues systematically, the dissertation is subdivided into three parts: (1) Tissue Optics; (2) Theoretical Modeling; (3) Experimental Techniques and their Medical Application.

## 1.2 Objective

The aim of the dissertation project is to turn a novel promising idea that exploits the photonics and soft tissue interactions into practical usage, that would in turn benefit society through improved medical diagnostics. The project includes the investigations on laser irradiance reflectivity from dermis and epidermis layers, depth of tissue layer damaged due to carbonization and the tension and stress estimation of enclosed tissue such as vocal cord.

Several groups have used the reflection of polarized light to image tissues such as skin.[3,4,5,6,7,8] In using polarized light, one can take advantage of that fact that linearly polarized light becomes increasingly randomly polarized as it propagates through the skin due to its large scattering coefficient. Linearly polarized light with cross polarizers has been used in lens photography to investigate the skin surfaces and to improve anterior segment photography[4,5,6,7,8]. Light, which is reflected from the skin, has two components. The first one, which maintains the polarization of the incident light, is the regular reflectance that comes predominately from the surface of the skin. The second component comes from within the tissue due to backscattering of light from the various skin layers. The backscattered light is predominately randomly polarized due to the large scattering coefficient of the skin. Using a polarized light source and another polarizer in front of the camera parallel to first polarizer (in front of the light source) researchers observed skin surface details from the reflected light (surface reflection). In crossed-polarization, they eliminate the surface reflection and preferentially detect the diffusely backscattered light. From the backscattering light reflection they obtain information about pigmentation, erythema, infiltrates, vessels, and other intra-cutaneous structures.

The polarization properties of reflected or transmitted light depend on the number of scattering events that take place for each photon.[3] For photons that suffer virtually no scattering events (so called ballistic photons), their polarization properties are preserved. As photons participate in more and more scattering events, their final polarization state becomes more randomized. In the limit of many scattering events in a turbid tissue such as skin, the outgoing photons (diffusive photons) are unpolarized with equal intensity components parallel and perpendicular to the polarization of the incident light. Although

the diffusive photons can provide information along the tissue's thickness (depending on the penetration depth of the light source), it is difficult to determine which areas of tissue were sampled due to the multiple scattering events. On the contrary, ballistic photons are partially reflected whenever there is an index of refraction difference from one tissue layer into another. Hence, the diffusive photons generally contribute to a background noise in every direction, that masks the tissue imaging information carried by the ballistic photons. In the 2-D polarization imaging technique[3] as well as other similar polarization measurements the perpendicular component of diffusely reflected light is subtracted from the parallel component (ballistic plus diffusive) to remove the background noise.

The major innovation of this thesis is to apply 2-Dimensional polarization imaging to the measurement of the mechanical properties of soft tissues. This new optical technique[2] is based on a modification of the 2-D polarization imaging method[3] to measure skin stretch non-invasively by using the small changes that take place in the diffuse and specular reflective properties of skin due to applied mechanical load.

Currently, in-vivo surface deformation patterns of skin can be obtained optically by a video dimension analyzer (VDA) or video motion analyzer (VMA),[9,10,11] which will be discussed later in the subsequent chapter on the section of prior art measurements.

Optical properties of skin are related to its structure and chemical composition[12]. Techniques of light reflection have been used to study the intrinsic properties of skin (such as absorption and scattering coefficients) and mathematical models have been developed to take these into account[13,14,15,16,17,18,19,20,21]. These studies were mainly used to determine the effects of pigments and hemoglobin on the reflection and transmission characteristics of the skin due to changes in the skin structure. Specific areas of study

include skin erythema due to ultraviolet (UV) light exposure, and mechanical compression of the skin[13,15,16,20,21,22].

Previous experimental studies done by the dissertation researchers, on guinea pigs and the theoretical modeling suggested that changes in the roughness of the skin layers might be responsible for the observed dependence of reflectivity with stretch[2]. In this research dissertation, the experimental set up and the measuring technique, in addition to experimental data obtained from animal and in-vivo human skin experiments are discussed.

## 1.3 Background Information

The goal of this dissertation project is to develop a non-invasive, optical technique for measuring the stretch of soft-tissues such as skin. Three applications are envisioned for the technique: wound suturing and healing, diagnostic of burnt skin, and endoscopic diagnostics of vocal cords.

The proposed technique is a modification of Polarization Imaging.[23] In this technique, polarized light is reflected from the tissue. The reflected light is comprised of two components: specularly reflected light (which carries information about the interfaces from which it was reflected and maintains the polarization state of the incident light) and diffusively reflected light, which acts as a source of randomly, polarized noise. In the Polarization imaging technique, the diffusive component is subtracted from the total reflected component to isolate the specular component of the reflected light.

### 1.3.1 Wound Suturing and Healing

Visualization of skin deformations due to different surgical procedures is an important problem in plastic surgery. Large local deformations can be easily produced during suturing. Locally generated large deformations during the skin expansion and skin flap procedures can create undesirable consequences. Deformation of the skin is related to the mechanical forces that are generated in the skin due to external and/or internal forces.

High-tension forces that can generate local large deformations across a sutured wound, are likely to produce a stretched hyper tropic scar at that site[24,25]. Better scars are produced when the wound axis is placed parallel to Langer's lines (tension) compared to the case when the axis is across the lines[24,,26]. Dehiscence, ischemia or necrosis may be expected in regions of high stresses through compromise of circulation in the sub dermal vascular plexus. Blood flow is inversely proportional to wound closure tension as observed in animal studies[27]. Therefore, it is worthwhile to determine deformations and estimate stresses in skin tissue accurately for a given pattern of wound suturing and/or in other surgical procedures where large stretches are generated in skin.

Biomechanical models and finite element analysis have been used in skin research to compute large stretches and predict stress concentrations. Using this information, researchers have determined preferred suturing patterns and wound geometries[27,28,29,30,31]. In addition, finite element analysis has been applied to deformation patterns and to estimate the stress distributions in skin flaps[32]. It is constructive to point out here that the deformation patterns of in-vivo measurements will only help to estimate the stresses in skin because of skin's anisotropic mechanical properties[30,33,34,35] and also, the interaction between the dermis and hypodermis[36].

The real time measurement of skin stretch and estimation of stresses in skin is an important problem in wound closure, healing, and scar tissue formation. Excessive tensile stresses delay wound healing and cause scar tissue and granulation.[24,25,26] Therefore, it is worthwhile to determine deformations and predict stresses accurately for a given pattern of wound suturing. A preferred suturing pattern and wound geometry should produce low average stretch or tensile stresses with the lowest possible stress gradient at the critical points of the wound edges.[28,37] Stress/strain measurements of the biomechanical properties of connective tissues in ligaments and arterial walls[11,38] have lead to a better understanding of these properties. Improved measures and spatial resolution will allow closer examination of such factors as arterial wall stress that has been linked to atherogenesis. With the advent of artificial biomaterials, there is a need to assess and match their mechanical properties to biological tissues, especially with vascular grafts.[11]

### 1.3.2 Diagnostics of Burned Skin

The real-time measurement of soft-tissue viability for indeterminate burns is an important problem in plastic surgery and treatment of burns. For indeterminate burns, a key issue is to make a decision as quickly as possible whether or not to graft a burned area of skin or let it heal spontaneously. Currently, this decision is made by clinical judgment or waiting days to see whether or not the burn heals. A novel minimally invasive, in-situ imaging technique for measuring the polarized reflectivity of light as a function of soft-tissue stretch is described. It is proposed that this technique, which is a modification of Polarization Imaging,[23] be applied to burn soft tissue to predict whether or not surgical intervention is required.

Specifically, the slope (change in reflectivity per change in stretch) of the reflectivity versus stretch data is related to the mechanical properties of the skin. In turn, these properties are altered by the depth and degree of thermal damage to the skin. Since different colors of light penetrate to different depths in the skin tissue, the depth of a burn can be ascertained by wavelength dependent polarization imaging. By subtracting polarization images obtained at two different wavelengths, the 3-D reflectivity image from different tissue depths and skin layers can be obtained. By applying different amounts of stretch to the burned tissue, a 3-D map of the biomechanical characteristics of the burns can be constructed.

The technique is minimally invasive since stretch (<10%) can be applied in-vivo outside of the burned area that is imaged using light. In the experimental work, more attention is given to the capillary beds in dermis since this skin layer is vital to skin regeneration. If the viability of this layer after burning can be determined with polarization imaging, then a physician might be able to use this information to classify the burn and thereby quickly decide on a treatment protocol.

### 1.3.3 Endoscopic Investigation of Vocal Cords

The human vocal cord can be easily damaged by too much tension being assert to it, such as through prolonged vocalization of a singer or yelling. The healing process of the damaged vocal cord is currently monitored by the repeated pronunciation of the consonant with a standard set of pre-recorded data and patients' input of the pain while swallowing.[39] The mechanics of the treatment is dependent on the patient and the doctor. Proper monitoring of the stretch and tension that the vocal cord sub-glottal tissue experienced while vocalizing with help in the understanding of the damages and their

recoveries. Hence, the technique is suggested to investigate the biomechanics of the vocal box tissue as a function of stretching due to vibration and to help in determining the ideal healing process of human vocal cord with a modified endoscope from Columbia Medical School, NY.

## 1.4 Prior Art - Measurement of Tissue Stretch

The applications of polarization imaging described in this dissertation are to measure the mechanical properties of soft tissue such as stretch and stress. The physical mechanism by which the optical properties of the soft tissues change is stretch induced changes in the soft tissues topology or surface roughness. In this section, prior art measurements of soft tissue stretch/stress and topology are reviewed.

### 1.4.1 Prior Art Mechanical Properties

Several competing measurement techniques for soft tissue stretch and estimating the stresses have been developed in the health sciences to determine the biomechanical properties of soft tissue. They can be generally grouped into two main categories, namely, the direct contact systems and optical imaging systems[9,10,40,41,42,43], which are non-contact. In general, the non-contact case is defined as minima or no physical contact between the probing apparatus and its system with the wound or sample that is under investigation.

The direct contact systems, which are inherently invasive, contact measurement methods, involve physical contact with the wound or sample. In ultrasonic scattering[44,45] approach to measure the soft tissue stretch/stress, the position of the surface is imaged by measuring the backscatter of ultrasonic waves. The stretch of soft tissue is inferred by

applying a known displacement to the soft tissue and imaging the resulting deformation using ultrasound. By measuring successive deformations due to known displacements or forces, the elasticity and strain fields can be calculated.

The spatial resolution of the technique, 20-30 um is partially determined by the frequency of the ultrasound employed, 40-100 MHz. One advantage of the ultrasonic imaging system is that by using a 3-D transducer array, it is possible to image the surface of the tissue as well as probing several mm into the tissue. However, while the ultrasonic system is well suited for in-vivo measurements of tissue in an aqueous environment, the need to couple the ultrasonic waves from the transducer into the tissues and back requires an aqueous environment or acoustic matching gel surrounding the tissue and probe. Consequently, the ultrasonic imaging method is generally not applicable, to non-aqueous environment, without its selected matching gel, to suturing procedures and measurement of burns on human skin.

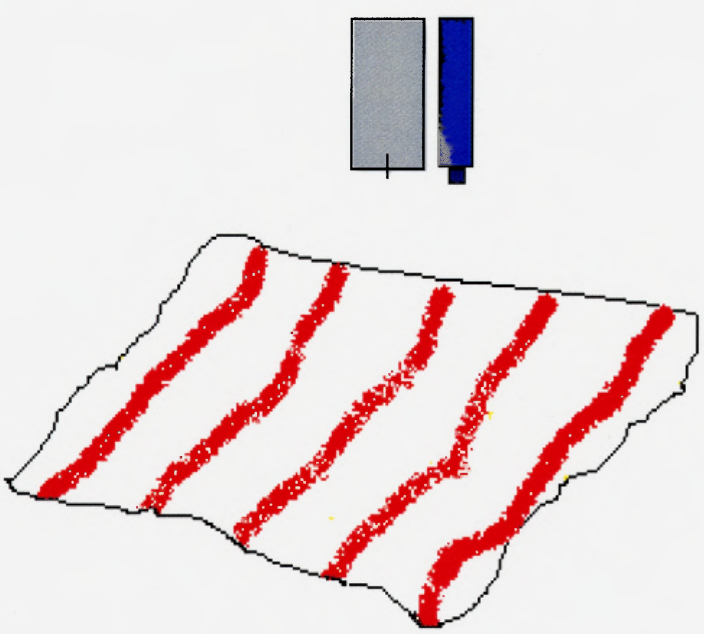

**Figure 1.1** A Video Dimension Analyzer (VDA) illustration.

Other optical imaging systems are video dimension analyzer (VDA) and video motion analyzer (VMA). In-vivo surface deformation patterns of skin can be obtained optically both by a VDA and VMA.[10,11,41] The VDA system consists of a TV camera, monitor and a dimensional analyzer, which is shown in the Figure 1.1. The dimensional analyzer converts the distance between parallel stain markers on the surface of a substrate under investigation to a proportional voltage.

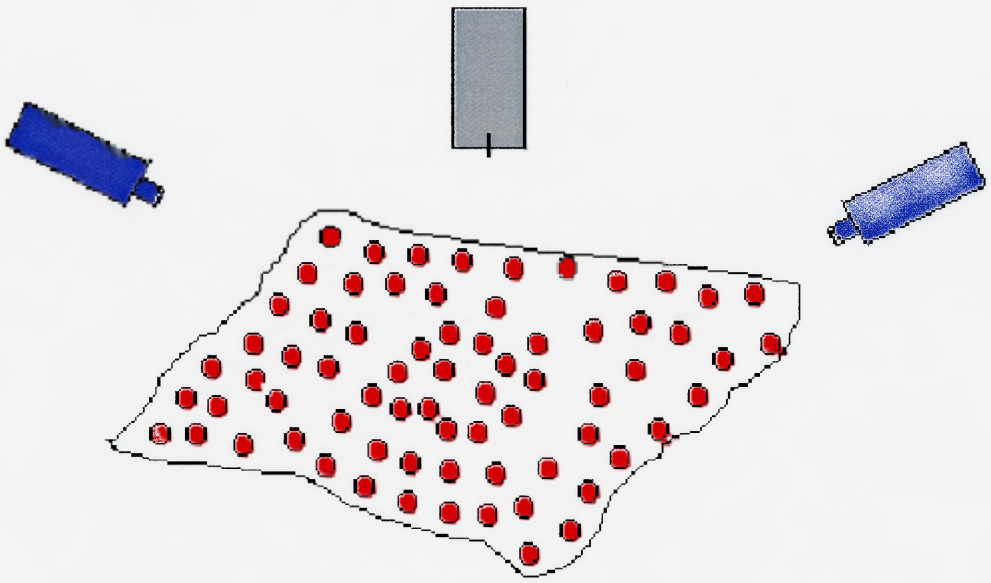

**Figure 1.2** Video Motion Analyzer (VMA) depiction.

In contrast, the VMA systems can generate a 3-D image of a stretch using fluorescent markers (or other physical markers) that are placed on a tissue under study. The markers are imaged with three different cameras and the information is stored in a computer. The stretches can be computed from two successive video frames via software. Its illustration is as shown in the Figure 1.2.

### 1.4.2 Prior Art Surface Roughness

Soft tissue surface topology or roughness determination is significant in many fields of science and engineering. Despite numerous methods of determining surface roughness properties, the oldest and only standard technique widely used and popularly accepted, involves the use of a mechanical profilometer. A simple illustration of the mechanical profilometer is as depicted in the following Figure 1.3.

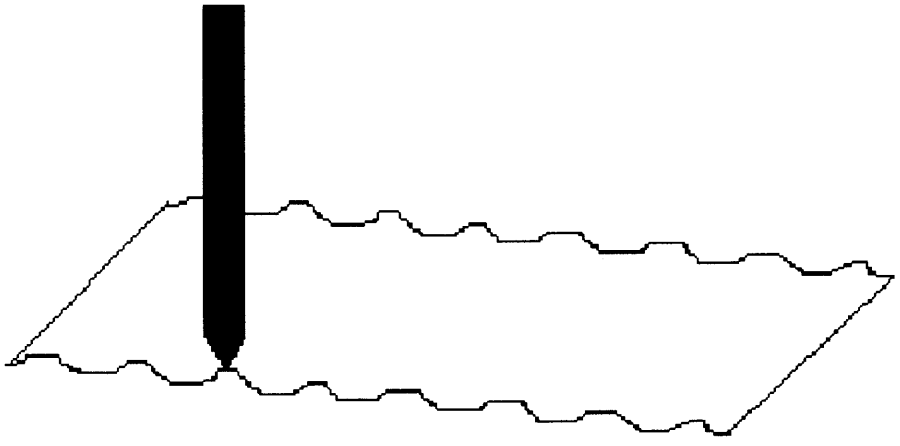

**Figure 1.3** Mechanical profilometer illustration.

The instrument produces a positive hard replica of the skin surface[46,47,48] by lightly and directly tracing with a narrow diamond stylus, which in turns generates a time varying analog voltage output proportional to the height of the surface profile, before each stretch.

This described method has several disadvantages: low speed of data acquisitions due to the need for physical contact between the stylus diamond tip and the surface. It can even damaged the object under investigation. It usually measures the average surface height derivation independent of the correlation length or average gradient of the surface

roughness. Furthermore, this method allows only 1-D results at a time, and therefore impractical for surveying/ mapping of the entire 2-D rough surface. Its surface roughness is as accurate and true as the size of the stylus tip, since a wider tip would not trace out the lateral size of the surface irregularities.

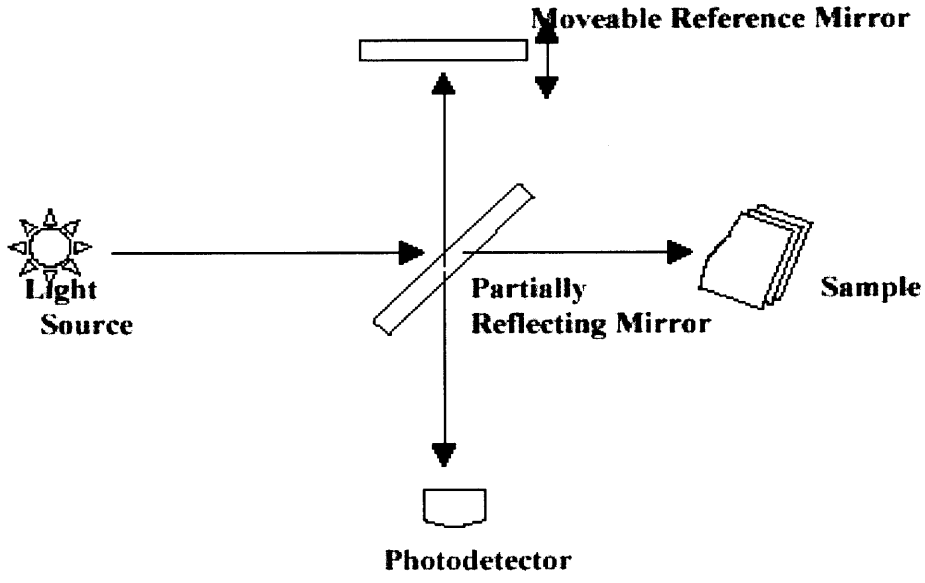


**Figure 1.4** Typical Optical Coherence Tomography (OCT) setup, which mimics the Michelson interferometer approaches.

Due to the drawbacks, subsequence investigations have shifted gear to focus on the development of the non-contact, optical base techniques for surface roughness measurement. The most current and popular optical method is non other than the optical coherence tomography (OCT)[49], which utilizes interferometry[50]. A typical setup of this OCT method used is shown in the following Figure 1.4.

The interferometry techniques, based on the fringes contrast measurement, requires that the height of the surface roughness must be multiple number of wavelength, and is therefore limited in use, since in-situ specimen movement artifacts, vibration and other random noises overshadow the true signals. OCT also requires that the sample to be "mounted" perfectly flat[49] before measurement can be made; even tough it is a non-contact method, making it unportable. On the other hand, the light scattering techniques, generally requires a gaussian distribution of surface height[51,52]. Another method utilizes the study of the statistical properties of laser speckle patterns to measure the surface roughness; pioneered by Sprague[53] and later by Asakura and his colleagues.[54]

# CHAPTER 2

# TISSUE OPTICS

## 2.1 Introduction

The development of a unified theory for the photonics tissue response or interaction with laser irradiation is in its infancy.[55] This dissertation's chapter describes the current understanding of the physical events that can occur when laser light source interacts with tissue. Followed by, a sequence of formulations that acts as a simple theoretical model of light reflected from the soft tissue interface, which estimates the optical responses of stretched tissue to laser radiation.

## 2.2 Characteristics of Laser Source

The optical techniques presented in this dissertation require the responses of tissue to laser irradiation. Moreover, the optical response is highly dependent upon the characteristics of the laser source. It is appropriate, therefore to describe various laser parameters and their effects upon the tissue response.

Fundamental laser irradiation parameters for establishing dosimetry requirements for any laser applications to therapeutic procedure are, namely the power, irradiation duration, and cross section spot size for a continuous wave (CW) laser. Conceivably, the most important parameter for the 2-D Polarization Imaging Elastometry Technique[2] is irradiance, measured in $W/m^2$ units.

The irradiance is a function of the power delivered and the laser spot size on the tissue. Low irradiances that do not significantly increase tissue temperature are associated

with diagnostics applications, photochemical processes, and biostimulation. Alternatively, high irradiances can ablate tissue and create mechanical damage in tissue. The depth at which laser light effects tissue depends upon the optical properties of tissue, which vary with wavelength.

The available spectrum of commercially available laser for diagnostics and therapeutic medical applications ranges from the ultraviolet (UV) domain, 193 nm, to the far mid-infra-red (IR) domain, 10,600 nm. Since the absorption and scattering of any tissue varies with wavelength, there are dramatic differences in the penetration depth of the radiation from various laser sources. Light with a wavelength of at either 193 nm or 29,600 nm is totally absorbed in the first few micron of tissue owing to amino acid absorption in the UV and water absorption in the IR range. In contrast, wavelengths from 600 nm to approximately 1,100 nm can penetrate several millimeters inside the tissue. Within this described wavelength ranges, there is a lack of strongly absorbing tissue chromophores. As a collimated beam passes through tissue, it is exponentially attenuated by absorption and scattering. The scattered light forms a diffuse conic volume around the reflected direction. In addition, thermal heat is generated wherever light is absorbed.

Optical parameters, such as index of refraction, absorption, and other properties are not constant, but can dynamically change depending upon the condition of the tissue.[55] Temperature, dehydration and/or hydration, thermal damage can alter the absorption and scattering properties of tissue. The most prominent example is the egg albumin. The clear albumin becomes solid and white when irradiated and heat coagulates the medium. During coagulation processes, the scattering increases dramatically and hence the optical and mechanical properties of tissue may significantly change during laser irradiation.

Soft tissue is a complex medium, and many of the optical events produced by laser irradiation are interdependent. In spite of that, it was found that many of the assumptions used throughout the dissertation to make formulations tractable, produce solutions that are reasonably describe the behavior of laser irradiated tissue. Obviously, the mathematical formulations are not intended to model tissue at the microscopic level. Nevertheless, the governing equations provide the basis for successful models used for describing the experimental data.

## 2.3 Photonics Interaction with Soft Tissue

It is essential to understand the photonics interaction with soft tissue in order to exploit its usefulness. In general, the soft tissue investigated can be treated as an absorbing and scattering turbid medium.[12] In addition, light scattering from collagen has been used to infer the orientation and the size of collagen fibers.[56]

The interaction of radiation with matter is the fundamental for any imaging method.[57] Basically, two classes of interactions occurs; the first, is related to the discontinuities of optical properties at the interface between the two different medium, while the second is volume related and depends on the optical properties of the material (i.e. refractive index). At the interface of the two optical media, according to Snell's law the transmitted beam is refracted.

$$n_1 \sin\theta_1 = n_2 \sin\theta_2 \tag{2.3.1}$$

where $\theta_1$ and $\theta_2$ are the angles of incidence and refraction.

In additions, an optically flat surface behaves like a partly reflecting mirror. Light irradiated in the direction $(\theta_i,\phi_i)$ is reflected back in the direction $(\theta_i,\phi_i+\pi)$ in 3-D

spherical coordinate. This means that the angle of reflectance is always equal to the angle of incidence and that the incident and reflected ray and the normal of the surface lie in a plane. The ratio of the reflected radiant flux to the incident flux at the surface is called the reflectivity, r.

Specular reflection only occurs when all parallel incident rays are reflected as parallel rays. A surface needs to be perfectly smooth for specular reflectance because of the wave-like nature of the electromagnetic radiation. It is sufficient that the residual surface roughness irregularities are significant smaller than the wavelength (when comparing with Mie scattering theory). The reflectivity r, depends on the angle of incidence, the refractive indices, $n_1$ and $n_2$, of the two media meeting at the interface and the polarization state of the incident beam.

Light is called parallel or perpendicular polarized if the electric field vector is parallel or perpendicular to the plane of incidence, i.e. the plane consisting of the directions of incidence, refraction, and the surface normal.

Fresnel's equations give the reflectivity for parallel polarized[61] light to be;

$$r_{//} = \frac{\tan^2(\theta_1 - \theta_2)}{\tan^2(\theta_1 + \theta_2)} \tag{2.3.2}$$

and for perpendicular polarized light

$$r_{\perp} = \frac{\sin^2(\theta_1 - \theta_2)}{\sin^2(\theta_1 + \theta_2)} \tag{2.3.3}$$

At polarizing or Brewster angle of incidence ($\theta_b$), the parallel polarized light is not reflected at all. This condition occurs when the refracted and reflected rays would be perpendicular to each other.

$$\theta_b = \arcsin\left(\frac{1}{\sqrt{1+n_1^2/n_2^2}}\right) \tag{2.3.4}$$

Most natural and artificial objects do not reflect light directly but show a diffuse reflectance. The diffuse reflectance can be due to scattering in the bulk material or from surface roughness as the light propagates across layer boundaries. Microscopic surface roughness causes reflection in various directions depending on the slope distribution of the reflecting facets. Some materials produce strong forward scattering effects while others scatter almost equally in all directions. Other materials show a kind of mixed reflectivity, which is partly specular due to reflection at the smooth surface and partly diffuse, caused by the escape of diffusively scattered photons in the tissue. In this case, light penetrates partly into the object where it is scattered at optical inhomogeneities. Part of this scattered light leaves the object again, causing a diffuse reflection.[23]

Skin physiology can be described as a tough, supple membrane that covers the entire surface of the body.[58] It is the largest organ of the body and is composed of five layers of cells. Each layer is named for its unique function, texture, or position. The deepest layer is the stratum basale. It anchors the more superficial layers to the underlying tissues, and it provides new cells to replace the cells lost by abrasion from the outermost layer. The cells of each layer move upward as they mature. Above the stratum basale lies the stratum spinosum. The cells in this layer have tiny spines on their surfaces. As the cells move to the next layer, the stratum granulosum, they become flat, lying parallel with the surface of the skin. Over this layer lies a clear, thin band of tissue called the stratum lucidum. The boundaries of the cells are not visible in this layer. The outermost layer, the stratum corneum, is made up of scaly, squamous plaques of dead

cells that contain keratin. This horny layer is thick over areas of the body subject to abrasion, as the palms of the hands, and thin over other more protected areas. The color of the skin varies according to the amount of melanin in the epidermis. Genetic differences determine the amount of melanin. The ultraviolet rays of the sun stimulate the production of melanin, which absorbs the rays and at the same time darkens the skin. Altered skin continues into various parts of the body as mucous membrane, as in the lining of the vagina, the bladder, the lungs, the intestines, the nose, and the mouth. Mucous membrane lacks the heavily keratinized layer of the outside skin. It releases the mucus that lubricates and protects nearby structures. The skin helps to cool the body when the temperature rises by radiating the heat flow in widened blood vessels and by providing a surface for the evaporation of sweat. When the temperature drops, the blood vessels narrow and the production of sweat lessens.

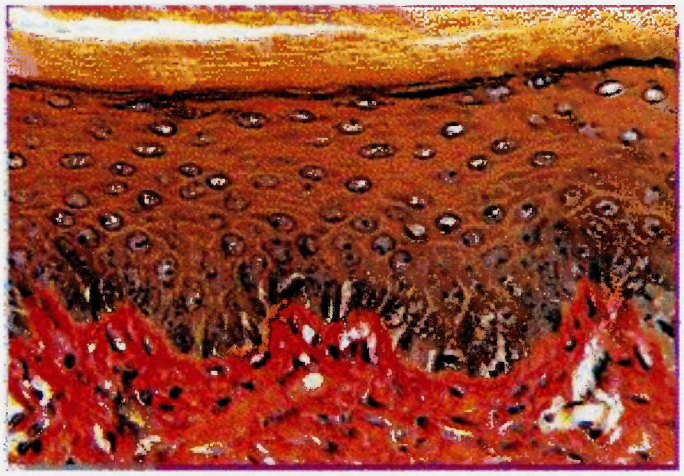

**Figure 2.1** Photomicrograph of skin physiology (adapted from Thibodeau 1993).

When a beam of light reaches the skin surface, a small portion of it, about 5%, is reflected by the surface directly due to a change in the index of refraction, whereas the rest is refracted and transmitted into the skin.[12,13,59,60] The direct reflection of light by a

surface for which the angle of the reflected light is equal to the angle of the incident light, specular reflection, is related to the refractive-index change between the air and the reflecting medium.[61]

By its nature, the reflection of light from a turbid medium such as skin is diffuse rather than specular. The intensity and the angular distribution of diffusive reflection are determined by the transmission and the scattering properties of the skin tissue,[13,20,21] as well as by the polarization state of the incident light.[62] A portion of the light that is transmitted through the top layer of skin is scattered and absorbed by the underlying skin tissue. After multiple scattering events and reflections from the different layers of skin, some of the transmitted light reemerges through the air–stratum interface into the air as part of the total reflected light intensity. The polarization properties of the reflected or the transmitted light depend on the number of scattering events that take place for each photon of light.[3] The possible paths of a photon interacting within the soft tissue and skin layer structure with its dimension are illustrated in Figure 2.2 below.

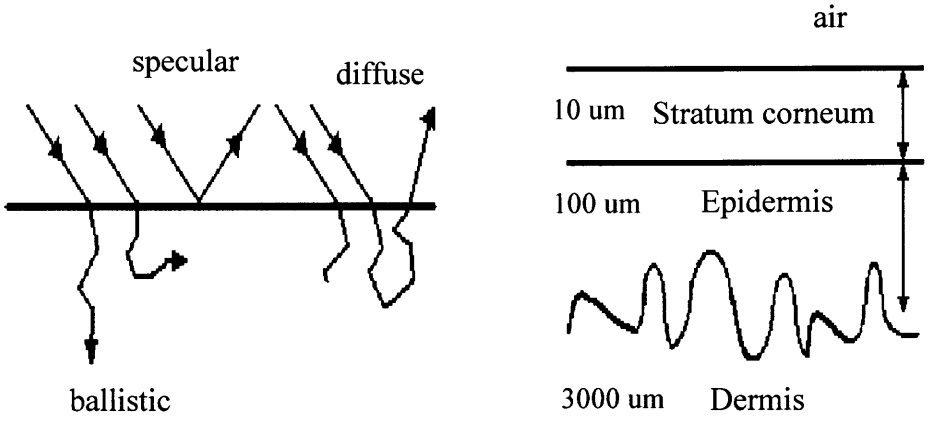


**Figure 2.2** Scatter beam path and Skin layer structure and dimension.

Photons that suffer virtually no scattering events preserve their polarization properties. These are termed ballistic photons. As photons suffer more and more scattering events, their final polarization state becomes more randomized. In the limit of many scattering events in a turbid tissue the outgoing photons, defined as diffusive photons, are unpolarized and have equal intensity components that are parallel and perpendicular to the polarization of the incident light.

In addition, the diffusive photons are not useful for tissue imaging because it is difficult to determine which areas of tissue were sampled by the diffusive photons. On the other hand, ballistic photons are partially reflected whenever there is a refractive index difference on passage from one tissue layer into another. Hence, the diffusive photons generally contribute to background noise that masks the tissue imaging information carried by the ballistic photons.

Once the light penetrates into the skin tissue, it can be absorbed or scatter into different directions. These processes are described by an absorption coefficient $\mu_a$ and a scattering coefficient $\mu_s$ where, the mean free path for an absorption or scattering event is given by $1/\mu_a$ and $1/\mu_s$ respectively. The total attenuation coefficient for the propagation of light is $\mu_t = \mu_a + \mu_s$.

Light propagation inside soft tissue is also characterized by radiative transport theory with 3 different optical properties; absorption coefficient $\mu_a$, scattering coefficient $\mu_s$, and phase function $ph(\hat{s},\hat{s}')$. The phase function is used to define and describe the fraction of light scattered from the incident direction $\hat{s}$ into the direction $\hat{s}'$.

$$\int_{4\pi} ph(\hat{s},\hat{s}')dw' = 1 \qquad (2.3.5)$$

The phase function is integrated and normalized so that the integrand over all the solid angle or directions is one. Where $dw'$ in the above equation is the differential solid angle in the $\hat{s}'$ direction. In general, the functional form of the described phase function is usually unknown. In these cases, the phase function is normally characterized by its average cosine form.

$$g = \int_{4\pi} ph(\hat{s}, \hat{s}') * (\hat{s} \bullet \hat{s}') dw' \tag{2.3.6}$$

These average cosines of the phase function g, is defined and known as the anisotrophy coefficient. The anisotrophy coefficient varies between isotropic scattering, with g = 0, and complete forward scattering, with g = 1 in this case.

It is worth mentioned that the integrals in the above equations (2.3.5) and (2.3.6) are independent of the direction of $\hat{s}$. This meant that the scattering profile is not a function of the incident angle or direction. It is not surprising that a single anisotrophy coefficient is inadequate to explicate tissues that have specialized directions along which light scatters better or worse. A good example is soft tissue, such as tendon that has a preferred scattering direction along its oriented collagen fibers.

A popular and standard phase function used is the Henyey-Greenstein phase function.

$$ph(\cos\theta) = \frac{1}{4\pi} \frac{1-g^2}{[1+g^2-2g\mu]^{3/2}} \tag{2.3.7}$$

Using these basic optical properties, several useful parameters to describe the scattering can be derived. The effective attenuation coefficient is given as

$$\mu_{eff} = \sqrt{3\mu_a[\mu_a + \mu_s(1-g)]} \tag{2.3.8}$$

Often when the anisotrophy coefficient is not known, the reduced scattering coefficient is useful. It is derived from the similarity relations that reduce the number of necessary parameters from three to two variables. Two possible choices for a similarity transformation are

$$\mu_s' = [1 - g^2]\mu_s$$

or

$$\mu_s' = [1 - g]\mu_s \tag{2.3.9}$$

The latter is the most commonly used, while the former comes from the delta-Eddington approximation to a Henyey-Greenstein phase function.

Consequently, when a collimated laser beam is incident normal to the soft tissue interface, a small portion of the light is reflected at the surface, according to the well-known Fresnel's relation for specular reflection $r(\phi_i)$, at normal incidence

$$r = \frac{(n_1 - n_2)^2}{(n_1 + n_2)^2}, \qquad \phi_i = 0 \tag{2.3.10}$$

and the remaining light is attenuated in the tissue by the absorption and scattering according to the Beer's law,

$$E(z) = E_0(1 - r_{sc})e^{-(\mu_a + \mu_s)z} \tag{2.3.11}$$

where E(z) is the fluence rate of the collimated light at position z in the tissue with dimension $W/m^2$; $E_0$ is the collimated irradiance; $r_{sc}$ is the Fresnel surface (specular) reflection of the collimated light striking the external surface, given in Eqs. (2.3.2) as above; $\mu_a$ is the absorption coefficient with dimension $m^{-1}$; $\mu_s$ is the scattering coefficient with dimension $m^{-1}$.

The penetration depth δ of the collimated beam is then defined as the mean free path for an absorption or scattering event, and it is the depth where;

$$E(\delta) = E_0(1 - r_{sc})e^{-1} \tag{2.3.12}$$

Which is also the depth where the percent of collimated light transmitted into the tissue is reduced to 37%. Thus, the collimated penetration depth is defined as the reciprocal of the attenuation coefficient;

$$\delta = \frac{1}{\mu_a + \mu_s} = \frac{1}{\mu_t} \tag{2.3.13}$$

The following Figure 2.3 shows an estimate of the penetration depth as a function of wavelength for soft tissue, for the soft tissue burnt depth experimentation.

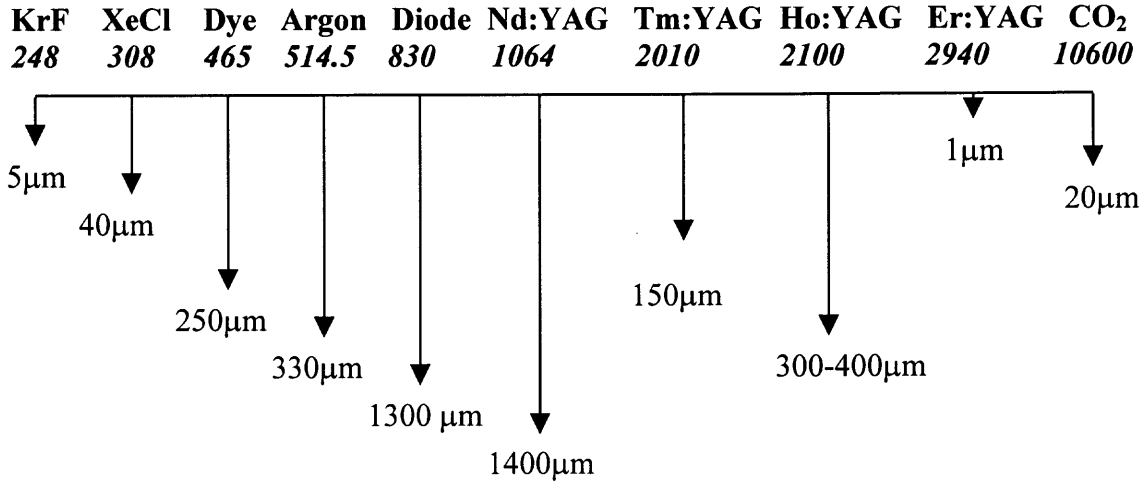


**Figure 2.3** Penetration depth of various lasers in non-colored soft tissue as a function of wavelength.

The scattering of light in the skin tissue is well explained by Mie scattering.[14]. In Mie scattering, the wavelength of light is comparable or smaller than the size of the scattering center. The probability for scattering is largest in the forward direction. In

contrast, Rayleigh scattering, which is responsible for the blue color of the sky, describe scattering by object, which are smaller than the wavelength of the light.

It is found that in expanding the reflection of polarized light from soft tissues reflectivity increases linearly with stretch is due to a changing surface roughness: As the rough surface or interfaces of the tissue smooth out with stretch, a smoother reflecting surface or interface is produced. For linearly polarized incident light the reflected light, which contains the imaging information, maintains the same linear polarization. However, there is also a component of the diffusely reflected light that has the same polarization. In the two-dimensional 2-D polarization-imaging technique subtracting the orthogonal component of the diffusely reflected light allows the background noise to be removed such that the skin tissue can be imaged. In this study, a new introduction, to our knowledge, technique based on a modification of the 2-D polarization-imaging method to measure skin stretch noninvasively by using the small changes that take place in the diffuse and the specular reflective properties of skin that are due to mechanical load.[63]

## 2.4 Theoretical Model

The relation between interface roughness and scattering can be explained if the incident light is regarded as being scattered from, the specular reflection or the transmission direction as it propagates through a rough surface. If the interface were rough, the local angle of incidence for an individual light ray would depend on the location at which that ray encountered the interface, as shown in Figure 2.4. Clearly, the presence of the rough interface would give rise to reflected laser power that would not be in the specular-reflection direction relative to the overall surface.

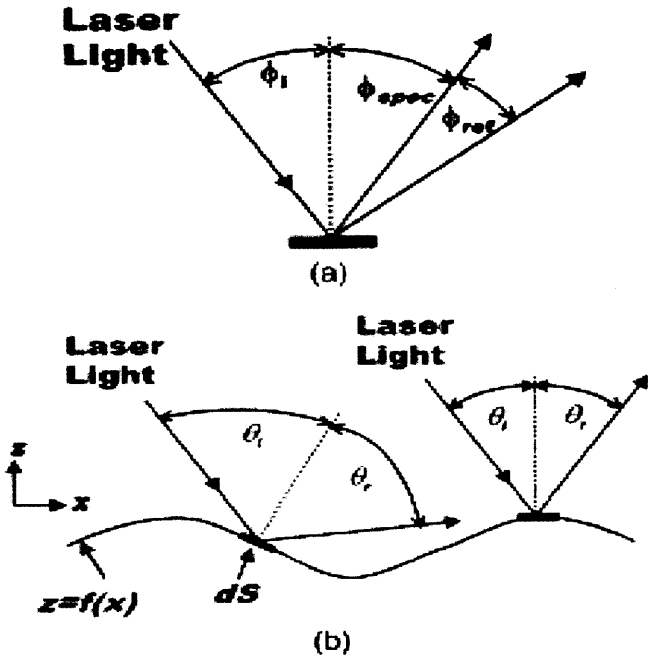


**Figure 2.4** a) Flat surface: macroscopic definitions of the angles of incidence, specular reflection, and ϕref relative to the macroscopic orientation. b) Rough surface: microscopic definitions of the angles of incidence and reflection for a rough interface.

When the wavelength is short compared with the height and the spatial extent of the roughness(Mie scattering), the angular and the intensity dependences of the reflectivity are derived from the geometry of the interface, assuming that light is specularly reflected from each tilted element of the interface. This limit is appropriate for examining the reflection from skin. Interface roughness affects the intensity of the reflected light through several mechanisms:

• the direction of the reflected light from an interface depends on the local slope of the surface.

• the intensity of the light reflected or transmitted from an interface depends on the local angle of incidence and the polarization, which in turn depend on the local slope.

• the diffusely scattered light that is transmitted back from the skin to the air (the right most ray in Figure 2.4) may pass through or be reflected from several rough interfaces. As with the transmission from air to skin, the intensity and the direction of the diffusely scattered light from skin to air depend on interface roughness.

In textbook treatments of tissue optics the reflectivity, contribution derived from surface roughness usually is neglected or incorporated into an overall attenuation coefficient for scattering.[61] Although neglecting the surface roughness is appropriate for the stratum corneum layer of skin Figure 2.4, underlying layers of skin such as the epidermis and the dermis are characterized by numerous rough interfaces such as the boundary between the epidermis and the dermis.

The papillary layer beneath this epidermis–dermis junction consists of numerous highly sensitive and vascular eminences, termed papillae, which project perpendicularly. This region is closely related to rich capillary beds in the dermis. This capillary structure supplies nutrients to the epidermis. The roughness of this junction allows the tight binding between the epidermis and the dermis and allows a large surface area for nutritional exchange.[64]

The experimental configuration is chosen to accentuate the contribution to the reflectivity from the outermost 100 mm of skin. It is well known that shorter wavelengths of light (blue) do not penetrate as far into the skin as do longer wavelengths (red). Thus shorter wavelengths of light (488 nm) should be more sensitive to interface-roughness changes than red light would be. For *in vivo* samples, the reflectivity of red light is also strongly influenced by the presence of blood in the underlying tissue.

To demonstrate the effect of large-scale roughness on the reflectivity from soft tissue, we start with a simple 1-D model for the roughness $z$ of an interface[65]:

$$z = A * \sin(g * x) \tag{2.4.1}$$

where $A$ is the height of the roughness with a periodicity of $2\pi/g$.

This periodic model was suggested originally for the surface roughness of skin and is used to explain how the surface patterns of the skin change as a result of tension loads.[65] Although the periodic-roughness assumption is not strictly true, the physiology of the various skin layers[64] and topological measurements of skin[66] show quasi-periodic interfaces between different layers of skin. Therefore, a periodic-roughness rather than a random-roughness model appears to be appropriate, with the spatial scale of the periodic roughness representing a characteristic roughness scale of the skin.

As a further simplification, interference among the various rays of light reflecting from the surface (laser speckle) can be ignored. This approximation is valid because of the long integration time for data acquisition by use of phase-sensitive detection (a 1-s time constant) and the fairly large solid angle of detection. The 1-s integration time is much longer than the correlation time of laser-induced speckles so that temporally the speckle effect is averaged out.[62] In addition, reflected light is collected over a fairly large solid angle. Because all the collected light is detected by a single-element photodiode, any spatial fluctuations in light intensity caused by laser speckle are averaged out.

Clearly, the assumptions made in this model and the subsequent derivations are an oversimplification of the problem. However, this simple model demonstrates that interface roughness, which decreases with increasing stretch, could explain three of our experimental results:

a) the observed decrease in the diffusely reflected light intensity,

b) the observed increase in the specularly reflected light intensity, and

c) the linear relation between tissue stretch and reflectivity.

For the theoretical analysis, reflected light from the skin is collected with a lens that is oriented at an angle $\phi_{ref}$ and that collects light within an angle of $\Delta\phi_{ref}$ as shown in Figure 2.4. The collected light is focused onto a single-element detector. An angle of $\phi_{ref}$ =0 corresponds to the specular-reflection direction. The incident light is assumed to be of uniform intensity $I_o$ and to illuminate an area of dimensions $L_x$ *x* $L_y$ of the surface. The total power detected is

$$P(\phi_i) = -\int_S \int_{angles} Io\,\hat{k} * dSr(\theta_i)\delta(\theta_i = \phi_i + \phi_{ref}/2)d\phi_{ref} \qquad (2.4.2)$$

The integration is over the entire solid angle of the reflected light that is captured by the focusing lens and over the surface *S* of the reflecting tissue. The δ function selects out surfaces that are in the range of correct tilts such that the reflected light is within the acceptance angle $\Delta\phi_{ref}$; $r(\theta_i)$ is the Fresnel reflection (power) coefficient, $\hat{k}$ is a unit vector pointing in the direction of the incident light ray, and d*S* is the element of surface area whose vector point is normal to the surface, as shown in Figure 2.4.

### 2.4.1 One Dimension Sinusoidal Surface Profile Variations

For a given surface profile of $z = A\sin(gx)$, the normal to the surface is given by

$$\hat{n} = \frac{\nabla[z - A*\sin(gx)]}{\left|\nabla[z - A*\sin(gx)]\right|} = \frac{[\hat{z} - \hat{x}A*g*\cos(gx)]}{\{1+[A*g*\cos(gx)]^2\}^{1/2}} \qquad (2.4.3)$$

For a surface element to reflect light into the detection angle $\phi_{ref}$ its normal vector must be

$$\hat{n} = \hat{z}\cos(\phi_{ref}/2) + \hat{x}\sin(\phi_{ref}/2) \qquad (2.4.4)$$

Equating Eqs. (2.4.3) and (2.4.4) shows that, when $x$ satisfies light rays will be reflected into the detector.

$$\tan(\phi_{ref}/2) = -A * g * \cos(gx) \tag{2.4.5}$$

The vector properties of the surface integral can be written as

$$\hat{k} \cdot d\vec{S} = \hat{k}.\hat{n}dS \tag{2.4.6}$$

where $d\vec{S}$ = dx dy[$\vec{\nabla}[z - A\sin(gx)]$] and the ranges of d$x$ and d$y$ are determined from solutions for $x$ of Eqs. (2.4.5), where $\phi_{ref}$ varies between $\phi_{ref} \pm \Delta\phi_{ref}$.

As a simple example, consider light detected in the specular direction ($\phi_{ref}$ = 0) within a collection angle of $\pm\Delta\phi_{ref}$. Using Eqs. (2.4.5) and (2.4.6) shows that the total power detected is

$$P(\phi_i) = -\iint dxdyI_o\hat{k} \cdot \nabla[z - A * \sin(gx)]r(\theta_i = \phi_i + \phi_{ref}/2) \tag{2.4.7}$$

where

$$\hat{k} = -\hat{z}\cos(\phi_i) + \hat{x}\sin(\phi_i) \tag{2.4.8}$$

and the range of $x$ is given by the solution of Eqs. (2.4.5) when $-\Delta\phi_{ref} < \phi_{ref} < \Delta\phi_{ref}$. Because the integral is independent of the variable $y$, the integral over $y$ yields just $L_y$, the length along the $y$ axis. For small stretching and a small collection angle, one can consider $r(\theta_i)$ to be approximately constant with the *ranges* of d$x$ and d$y$ that contribute to the integral's changing with stretch. Furthermore, the fact that the topology of the surface is periodic can be exploited. Each cycle of the fluctuation of the wavelength $2\pi/g$ produces two areas that will reflect into the detector. If the integration over d$x$ were restricted to one wavelength of roughness the integral should be multiplied by $2L_x g/2\pi \equiv$

$N$, which represents the number of reflecting areas. The total power detected is then approximately

$$P(\phi_i) = NI_o L_y r(\phi_i) \int dx[\cos(\phi_i) + A * g * \sin(\phi_i)\cos(gx)] \tag{2.4.9}$$

The limits of integration are determined by Eqs. (2.4.5). For low values of $\Delta\phi_{ref}$ the ranges of d$x$ that contribute to the integral are $\pi/(2g)\pm\Delta x$ and $3\pi/(2g)\pm\Delta x$. In the limit of a flat surface, $Ag$= 0, and the limits of integration are between 0 and $\pi/g$. In this flat surface limit the power detected is

$$P(\phi_i) = NI_o \frac{\pi}{g} L_y r(\phi_i)\cos(\phi_i) = P_o r(\phi_i) \tag{2.4.10}$$

which is the just the reflectivity of a flat surface. Two regimes of roughness can be considered: $Ag$ >>1 (very rough surfaces) and $Ag$ << 1 (slightly rough surfaces). In the, extremely rough surface limit ($Ag$ >> 1) only a small fraction of the interface surface contributes to the detected reflected light. In this limit the integral is approximately

$$P(\phi_i) = NI_o L_y r(\phi_i) 2\cos(\phi_i)\Delta x \tag{2.4.11}$$

where $\Delta x$ represents the linear extent of the surface that contributes to the reflectivity. Using $\Delta\phi_{ref}$ /2= $Ag^2\Delta x$ as an approximate form of Eqs. (2.4.5) for a small cone of detected angles allows the detected power to be written as

$$P(\phi_i) = P_0 r(\phi_i) \frac{\Delta\phi_{ref}}{\pi Ag} \tag{2.4.12}$$

For the experimental configuration $P_0$, $\phi_i$, and $\Delta\phi_{ref}$ are kept constant. As the soft tissue is stretched, both the amplitude $A$ and the wave number $g$ decrease, leading to an *increase* in the detected power. As the interface roughness *decreases*, the detected power

in the specular direction *increases*. This increase in detected power is observed with our soft tissue sensor.

Using a simplified model for the mechanical properties of the skin allows the change in reflectivity for small stretches to be determined. As an interface within the skin (e.g., the epidermis–dermis interface) and other biological elements in the skin are stretched, the surface, the interface, and the extra-cellular matrix flatten out subject to the constraint that the length of the surface remains constant. Using the profile of the surface of $z=A\sin(gx)$ leads to the length of the surface being calculated as

$$L = \int\{\left|\nabla[z - A*\sin(gx)]\right|\}^{1/2} = M\int_0^{2\pi/g}\{[1+A^2g^2\cos^2(gx)]\}^{1/2}dx \qquad (2.4.13)$$

where $M$ is the number of oscillations of the surface and the integral is over one oscillation of the surface. As the skin is stretched, the height of the interface roughness $A$ and the scale length $2\pi/g$ change in such a way that the length of the surface remains constant. For $Ag >> 1$ the integral becomes

$$L \cong M\int_0^{2\pi/g} Ag\left|\cos(gx)\right|dx = 4MA \qquad (2.4.14)$$

In this very rough limit, as the tissue is stretched, $A$ approximately remains constant. The change in surface roughness becomes predominately from changes in the periodicity of the topology. Substituting this result into the expression for reflected power Eqs.(2.4.12) yields

$$P(\phi_i) = I_o L_y r(\phi_i)\frac{\Delta\phi_{ref}}{\pi}\frac{s}{2\pi}\cos(\phi_i)\frac{4M}{L}, \qquad Ag >> 1 \qquad (2.4.15)$$

It is interesting to note that, in the limit of high roughness ($Ag>>1$), the theoretical result shows that the reflected power is linearly proportional to the stretch $s$, in agreement with

the experimental results. Typically, for skin, the roughness of the epidermis–dermis interface is greater than the skin air roughness,[64,65] and the roughness of the epidermis–dermis interface satisfies the $Ag >> 1$, high-roughness condition.[64] Obtained experimental and theoretical results suggest that the changing roughness of the epidermis–dermis interface might be primarily responsible for the observed changes in light reflection owing to skin stretch. A plot of observed normalized reflectivity versus stretch data of non biological sample (rubber glove) is shown in Figure 2.5 to illustrate that experimental data is linear. Since, the basis analysis uses a sine function as the surface profile, which is one of the Fourier sine series components. Therefore, the theorem works for all surface variations and roughness that could be modeled as a sum of the sine functions into a Fourier sine series.

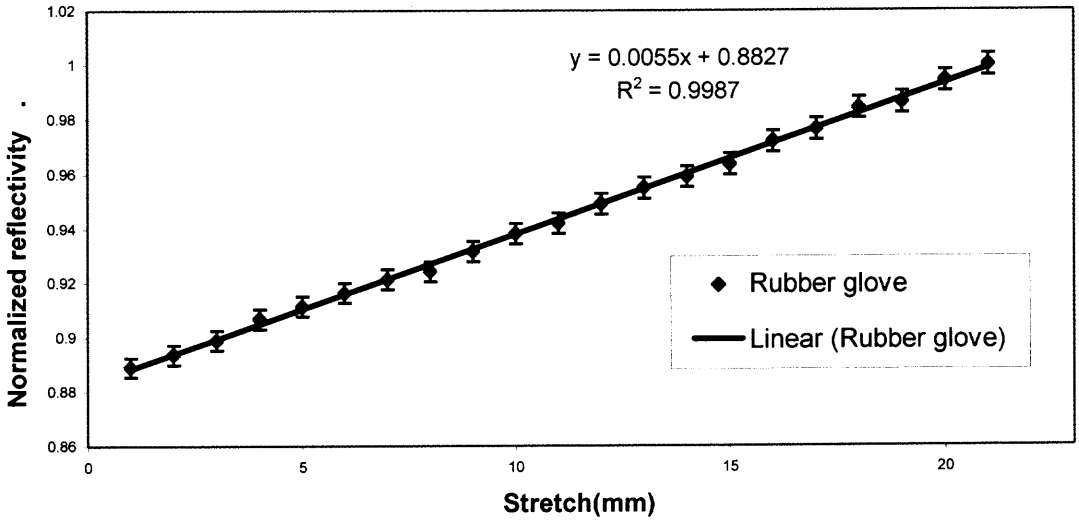


**Figure 2.5** Normalized reflectivity vs. stretch data of rubber glove.

### 2.4.2 Two Dimension Sinusoidal Surface Profile Variations

Similarly, the theoretical model described above, can be adapted to a two dimension sinusoidal variations. In investigation of the orientation of plane of incident relative to direction of stretch in the 2 dimensional case, the given 1 dimensional surface profile of $z = A \sin(gx)$, is modified to become

$$z = A * \sin(\vec{g} \bullet \vec{r}) \tag{2.4.16}$$

where $\vec{g} = \hat{x}g_x + \hat{y}g_y$ and $\vec{r} = \hat{x}x + \hat{y}y$

With the two-dimensional sinusoidal variation modification, the normal to the surface is given by

$$\hat{n} = \frac{\nabla[z - A * \sin(\vec{g} \bullet \vec{x})]}{|\nabla[z - A * \sin(\vec{g} \bullet \vec{x})]|}$$

$$= \frac{[\hat{z} - \hat{x}A * g_x * \cos(\vec{g} \bullet \vec{r}) - \hat{y}A * g_y \cos(\vec{g} \bullet \vec{r})]}{\{1 + [A * g_x * \cos(\vec{g} \bullet \vec{r})]^2 + [A * g_y * \cos(\vec{g} \bullet \vec{r})]^2\}^{1/2}} \tag{2.4.17}$$

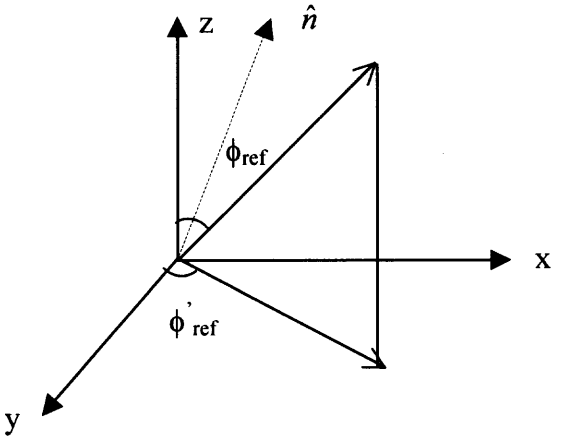


**Figure 2.6** Normal vector diagram.

While for the surface element to reflect light into the detection angle $\phi_{ref}$ its normal vectors must be

$$\hat{n} = \hat{z}\cos(\phi_{ref}/2) + \hat{x}\sin(\phi_{ref}/2)\cos(\phi'_{ref}) + \hat{y}\sin(\phi_{ref}/2)\sin(\phi'_{ref}) \tag{2.4.18}$$

to simplify Eqs. (2.4.18) the following variable substitution for the denominator is used

$$\alpha = \{1 + (A * g_x \cos(\vec{g} \bullet \vec{r}))^2 + (A * g_y \cos(\vec{g} \bullet \vec{r}))^2\}^{1/2} \tag{2.4.19}$$

hence, Eqs. (2.4.18) can be rewritten as

$$\hat{n} = \frac{1}{\alpha}\{\hat{z} - (A * g_x * \cos(\vec{g} \bullet \vec{r})) - (A * g_y * \cos(\vec{g} \bullet \vec{r}))\} \tag{2.4.20}$$

Next, by equating Eqs. (2.4.18) and (2.4.20), it shows that, when $\vec{r}$ satisfies Eqs. (2.4.21a-c), light rays will be reflected into the detector.

$$\hat{z}: \qquad \frac{1}{\alpha} = \cos(\frac{\phi_{ref}}{2}) \tag{2.4.21a}$$

$$\hat{x}: \qquad \frac{-Ag_x}{\alpha}\cos(\vec{g} \bullet \vec{r}) = \sin(\frac{\phi_{ref}}{2})\cos(\phi_{ref}^{'}) \tag{2.4.21b}$$

$$\hat{y}: \qquad \frac{-Ag_y}{\alpha}\cos(\vec{g} \bullet \vec{r}) = \sin(\frac{\phi_{ref}}{2})\sin(\phi_{ref}^{'}) \tag{2.4.21c}$$

By using the boundary condition of Eqs. (2.4.22c)/ Eqs. (2.4.22b)

$$\frac{g_y}{g_x} = \tan(\phi_{ref}^{'}) \tag{2.4.22}$$

for $g_y = 0$, the stretch is only directed in the $\hat{x}$ direction and this means only the tilt of the surface in the $\hat{x} - \hat{z}$ plane matters.

Next, by summing the squared Eqs. (2.4.21b) and Eqs. (2.3.21c), and for small angle of detections, $\phi_{ref} \approx 0$, the results is equal to

$$\frac{A^2 g_x^2}{\alpha^2}\cos^2(\vec{g} \bullet \vec{r}) + \frac{A^2 g_y^2}{\alpha^2}\cos^2(\vec{g} \bullet \vec{r}) = \sin^2(\frac{\phi_{ref}}{2})$$

$$\frac{A^2 g^2}{\alpha^2}\cos^2(\vec{g} \bullet \vec{r}) = \sin^2(\frac{\phi_{ref}}{2})$$

$$Ag\cos(\vec{g}\bullet\vec{r}) = \tan(\frac{\phi_{ref}}{2}) \tag{2.4.23}$$

hence Eqs. (2.4.23) with $\phi_{refx} \approx 0$ ($\Delta\phi_{ref} << 1$)

$$\frac{-Ag_x}{\alpha}\cos(\vec{g}\bullet\vec{r}) = 0 \tag{2.4.24}$$

where solving Eqs. (2.4.24) gets

$$\vec{g}\bullet\vec{r} = \frac{m\pi}{2} \qquad \text{m=1,3,5,7,.....} \tag{2.4.25}$$

The vector properties of the surface integral can be written as

$$\hat{k}\cdot dS = k\cdot\hat{n}dS \tag{2.4.26}$$

where dS= dx dy[$\nabla[z - A\sin(gx)]$]and the ranges of d$x$ and d$y$ are determined from solutions for $x$ of Eqs. (2.4.21), where $\phi_{ref}$ varies between $\phi_{ref} \pm \Delta\phi_{ref}$ and $\phi'_{ref} \pm \Delta\phi'_{ref}$.

$$\hat{k} = -\hat{z}\cos(\phi_i) + \frac{\hat{x}}{\sqrt{2}}\sin(\phi_i) + \frac{\hat{y}}{\sqrt{2}}\sin(\phi_i) \tag{2.4.27}$$

As a simple example, consider light detected in the specular direction ($\phi_{ref}$ = 0, $\Delta\phi'_{ref} = 0$) within a collection angle of $\pm\Delta\phi_{ref}$ and $\pm\Delta\phi'_{ref}$. For simplicity, one can assume that $\Delta\phi_{ref} = \Delta\phi'_{ref}$. Using Eqs. (2.4.21) and (2.4.26) shows that the total power detected is

$$P(\phi_i) = -\iint dxdyI_o\hat{k}\cdot\nabla[z - A*\sin(\vec{g}\bullet\vec{r})]r(\theta_i = \phi_i + (\phi_{ref}/2)\hat{\varphi} + (\phi'_{ref}/2)\hat{\theta}) \tag{2.4.28}$$

and the range of $x$ is given by the solution of Eqs. (2.4.21) when $-\Delta\phi'_{ref} < \phi'_{ref} < \Delta\phi'_{ref}$. For small stretching and a small collection angle, one can consider $r(\theta_i)$ to be approximately constant with the *ranges* of d$x$ and d$y$ that contribute to the integral's changing with stretch. The total power detected is then approximately

$$P(\phi_i) = -\int\int I_o.r.dxdy\{-\cos\phi_i - \frac{Ag_x}{\sqrt{2}}\sin(\phi_i)\cos(\vec{g}\bullet\vec{r}) - \frac{Ag_y}{\sqrt{2}}\sin(\phi_i)\cos(\vec{g}\bullet\vec{r})\} \quad (2.4.29)$$

By rotating the x-y coordinate system to a new x'-y' coordinates system so that $\vec{g} = g\hat{x}'$ only (or $\vec{g} = g\hat{y}'$ only), the integral does not depend on y coordinates (or x coordinates). The integration coordinates dxdy becomes dx'dy'. In the case of $\vec{g} = g\hat{x}'$ or $g = g_{x'}$, $\Delta y' \to \infty$ while $\Delta x' \to \frac{\Delta\phi_{rref}}{2g_x^2 A}$ and vice versa for $g = g_{y'}$ case with x' substituted with y'. The two dimensional model goes back to the one dimensional model described in Eqs. (2.4.15).

Therefore, in the limit of Ag >> 1, in the 2 dimension model, the theory again predicts that the reflected power is linearly proportional to the stretch applied. In essence, the polarization imaging method can determine the total stretch, but not the direction of the applied stretch. It is interesting to point out that the direction of the applied stretch can be determined by the use of the same model with the use of a cylindrical lens in place of the spherical lens. In this case, the limits of integration in Eqs. (2.4.28) and (2.4.29) are not equivalent since light is only collected and focused in one direction with a cylindrical lens.

# CHAPTER 3

# EXPERIMENTAL METHODOLOGY

## 3.1 Introduction

Experimental methodologies are discussed in the following sub-chapter with emphasis on the two types of detection techniques, namely point system and a CCD imaging system. Followed by, the algorithm used for the CCD digital image processing of the images captured with modified 2-D polarization elastometry experiments.

## 3.2 Measurement Systems

Various equipment and apparatus are need for the experimental work. Several light sources used includes a jumbo LED emitting incoherent red light at 633.0 nm, a Hitachi laser diode with wavelength of about 820 nm, with the corresponding Thorlabs laser diode power controller that regulate the power output was also used. In addition, a JDS Uniphase HeNe lasers with 500:1 ratio polarization distinction at wavelength of 632.8 nm (red), another similar HeNe laser, also with a 500:1 polarization distinction, operating at wavelength of 543.5 nm (green), and a Coherent argon gas laser capable of operating at about 430 nm to 514 nm wavelength, with variable output intensity were used.

For the specimen stretching apparatus, several mechanically actuated setups were built in the beginning to test out the hypothesis. The first, was the X-Y infinite screw stretcher mount of 1 mm step size. Followed by, the 1-D stage micrometer stretcher mount of 0.05 μm step size and a dial Vernier caliper forearm stretcher mount with variable step size, with the smallest stretching of 0.1 mm.

For more efficient functionality, the stretcher systems were then automated. They were as follows; a 1-D stepper motor controlled stretcher mount via National Instruments DAQ card with 0.5 mm step size, several 1-D Klinger translational stages stretcher mount controlled by its Klinger stepper motor controller via Labview with 1 μm step size, and recently 1-D stretcher using high speed Newport translational stages capable of a smallest step size of 0.01 μm, with its Newport controller. Cares were taken to pick all of the motorized stages with minimum mechanical hysterises to experimental repeatability.

Various detection systems were also employed for the data acquisition process. Multiple silicon photodetectors (PD) from Thorslabs are used in the point detection process. Whereas, in the case of, the 2-D experiment, Sony CCD cameras are used for the detection setup. Several Sony Mavica CCD cameras of different production periods are also employed in the setup. A pre-packaged system consists of a SBIG CCD camera; B/W and color monitors and Bandit video capturing board are additionally used. They are all calibrated to give only linear readings/responses before being utilized.

For the endoscopic experiment approaches, several types of polarization maintaining optical fiber, with core diameter ranging from 5.5 um to 250 um, are being tested and satisfy the requirement of the total diameter of the optical fiber must be smaller then the inherent standard utility port/instrument channel diameter of the endoscope, namely 2.8 mm.

Optical fiber bundle, made from PVC, plastics and glass were also being put to test. In this particular setup, besides the data acquisition described as above being used, the use of an optical spectrum analyzer also improves the finding.

## 3.3 2-D PIET Experimental Configuration

A schematic of the reflectivity experimental setup for measuring changes of reflected light intensity due to the applied stretch is shown below in Figure 3.1.

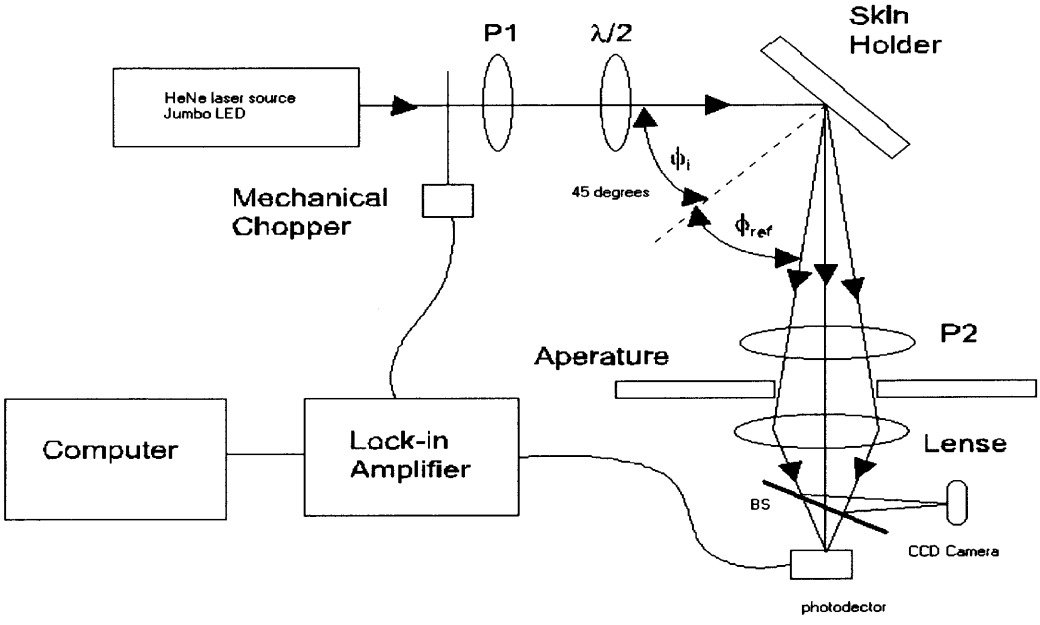


**Figure 3.1** Reflectivity experimental setup. Two detectors are used: a single element photodetector and a CCD camera.

The incident optical power level is typically ≤1mW. At this power level, the light intensity is kept low enough to ensure a linear detector response (voltage proportional to laser power) and to protect the soft tissue or skin from damage. Neutral density filters were used for above requirement, before the laser beam is passed thru the polarizer, P1. Linearly polarized light produced by the polarizer-orientated perpendicular to the tabletop is incident to the in-situ sample and is then reflected from the surface of the skin. The diameter of the incidence light was adjusted to two millimeters by means of an iris. The reflected light is collected onto the detection system using a lens (f=35mm) after it passes

through a second polarizer (analyzer). The polarization of the incident light and the analyzer can be set in one of two perpendicular orientations: either parallel or perpendicular to the plane of incidence. The incident polarization is adjusted using a rotating half-wave plate. This ensures equal intensities in either plane of polarization.

### 3.3.1 Point Detection with Silicon Photodetector

The soft tissue reflectivity is detected using the silicon photodetector by mechanically chopping the incident laser light and utilizing a lock-in amplifier and standard phase sensitive detection techniques. In this technique, the laser power on the skin is modulated at a fixed frequency by alternatively blocking and unblocking the laser beam with a rotating slotted disk. Consequently, the optical signal measured by the detector is modulated at this same frequency. The lock-in amplifier is designed to eliminate noise at all frequencies while locking on to and amplifying the signal frequency. This technique is particularly useful when measuring small signals in the presence of large background noise.

### 3.3.2 Image Detection with CCD System

From Figure 3.1 in the detection setup, the collected light (reflection) is split using a 50% pellicle beamsplitter and focused onto either a single element silicon photodetector of approximately $2mm^2$ active area or a CCD array digital camera. The angle of the collected reflected light and aperture size is adjusted to collect the light in the specularly reflected direction. The raw digital image acquisition system is consists of a SONY MAVICA™ CCD camera with a color CCD pixel array detector. The reflected power in

both the parallel and perpendicular polarization is measured as a function of the incident light polarization and skin stretch.

A typical example of the images captured before and after stretching by the CCD systems are as shown in the following Figure 3.2. The ratio of the unstretched and stretched images pixels were next computed and as shown in the Figure 3.3. The pixels ratio shows a symmetrical profile of the beam spot, with laser speckle scattered randomly across the gaussian profile. Next, is the cross sectional cut plot from the pixels ratio image shown in Figure 3.4. The results show that the reflectivity intensity is almost symmetric and consistent across the surface of the sample that is illuminated by the laser beam. This demonstrates that the reflectivity observed by the PIET with CCD detection system is applicable for the 2 dimensional cases.

**Figure 3.2** Images observed and recorded by the CCD detection system before stretching (left) and after 9% of stretching (right).

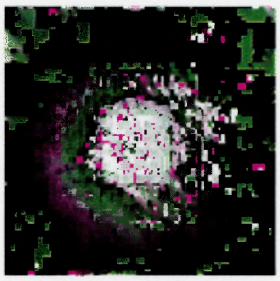

**Figure 3.3** Pixels ratio of the unstretch and stretched images given above.

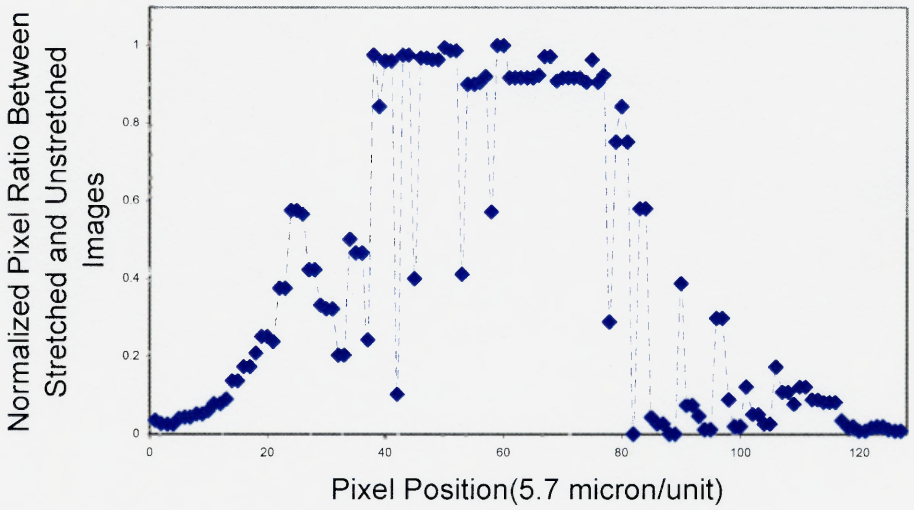


**Figure 3.4** A cross sectional cut plot of the pixel ratio of the Figure 3.3.

**3.3.2.1 Pixel Counting Algorithm.** Several different combinations of polarization angle of the skin reflection were observed and recorded as JPEG format for every skin stretches along the lines of tension of the skin (Langer line). The recorded image combinations were 0-0 degree polarization, 0-90 degree polarization, 90-90 degree polarization, and 90-0 degree polarization, with the first digit being the orientation of the polarizer P1 and the last digits representing the analyzer P2 orientation. The different polarization orientations were to reduce the unwanted diffused scattering from the skin at the particular polarization with the help of the specifically image analysis algorithm written for the 2-D polarization imaging technique.

Initially, all the pictures were converted to 16 bits and 24 bits GRAY scale format for analysis. However, its original content or color palette was converted accidentally/unintentionally by the commercially available software. Thus, inconsistency results, experimental system and camera linearity were questioned. The perplexity is

solved by breaking the images in question into the 3 main color component, namely the red, blue and green before being analyzed. Color images have an additional degree of freedom over grayscale a image, that is the mixture of the red, blue and green components in the image.

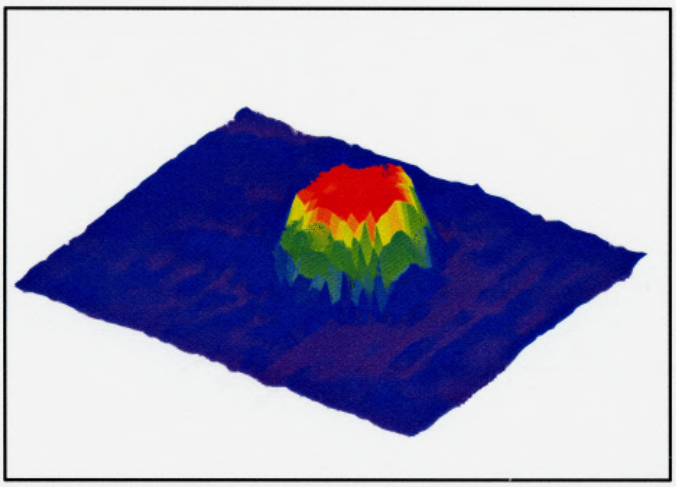


**Figure 3.5** Surface contour plot of an soft tissue image captured, in artificial color interpolation representation from the digitized matrices.

The images were then digitalized/converted into a matrices array by a mathematical software/algorithm. Arithmetic on a matrix provides for a wide variety of images processing techniques. In particular, the crossed pair of images, 0-0 and 0-90 or 90-0 and 90-90 pairs image pixel values were read into their numerical matrices respectively.

The unstretched skin reflection picture was used as the standard or norm to compare with the stretched pictures. The matrix then can be used to produce a surface

contour plot from a specified image, as shown in Figure 3.5 for artificial color contour and Figure 3.6 in wired mesh or select off a cross sectional profile across the images to be analyzed, as shown in Figure 3.7.

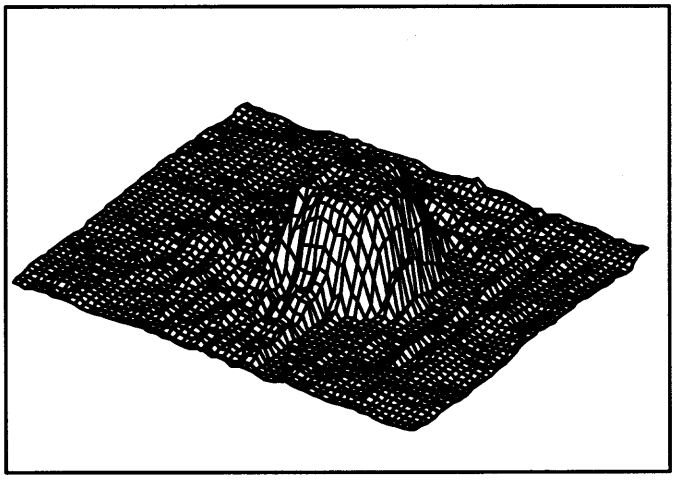


**Figure 3.6** Surface contour plot of the same captured soft tissue image, as in Figure 3.5, in wired mesh representation from the digitized matrices.

The unstretched soft tissue images, which acts as the calibration or reference image, is in turn superimposed on top of the respective stretched skin images of the same matrix array size and the net change of the total reflection of the skin is observed, analyze and compare with the standard point detection measurement.

Care was taken when the superposition overlapping is done with reference to the laser beam spot size and external markings in the apparatus that appears in pictures. In general, a net increment of the reflection intensity of the skin was observed. Analysis of the CCD images, agrees strongly with the point detection measurement technique results,

where an approximately 4.8% to 6% of reflectivity intensity increment is detected. The roughness or the surface's topologies of the skin can also being investigated, from the CCD images.

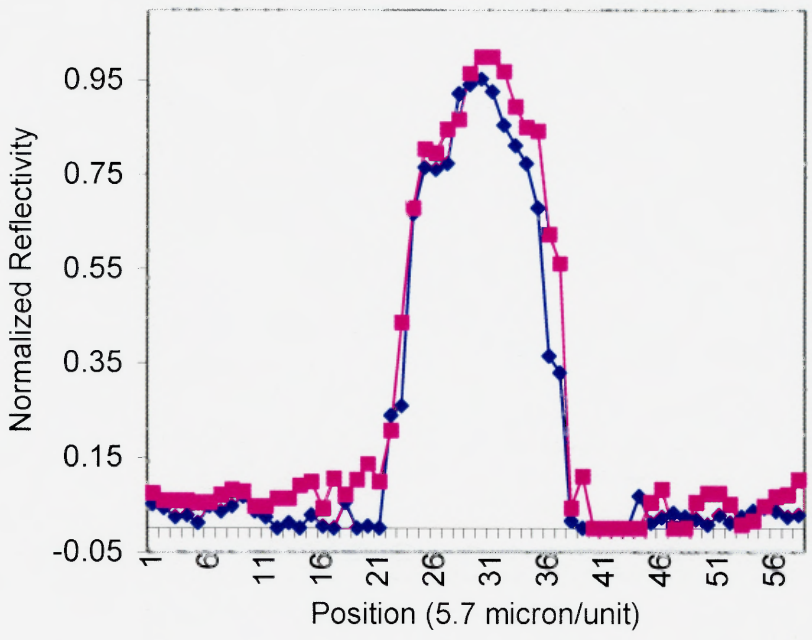


**Figure 3.7** A typical cross sectional plot of the un-stretched (pink squares) and 1 mm stretched (blue diamond) soft tissue, normalized reflectivity vs. position profile.

The algorithms designed and written specially for the image digitization task via Mathcad Professional 2000 version are as listed in Appendix A, for reference. Also, included are the codes for the different type of surface contour and the respective cross sectional comparative plots.

The crucial program logic for the CCD imaging analysis used is portrayed in the flowchart diagram drawn in Figure 3.8.

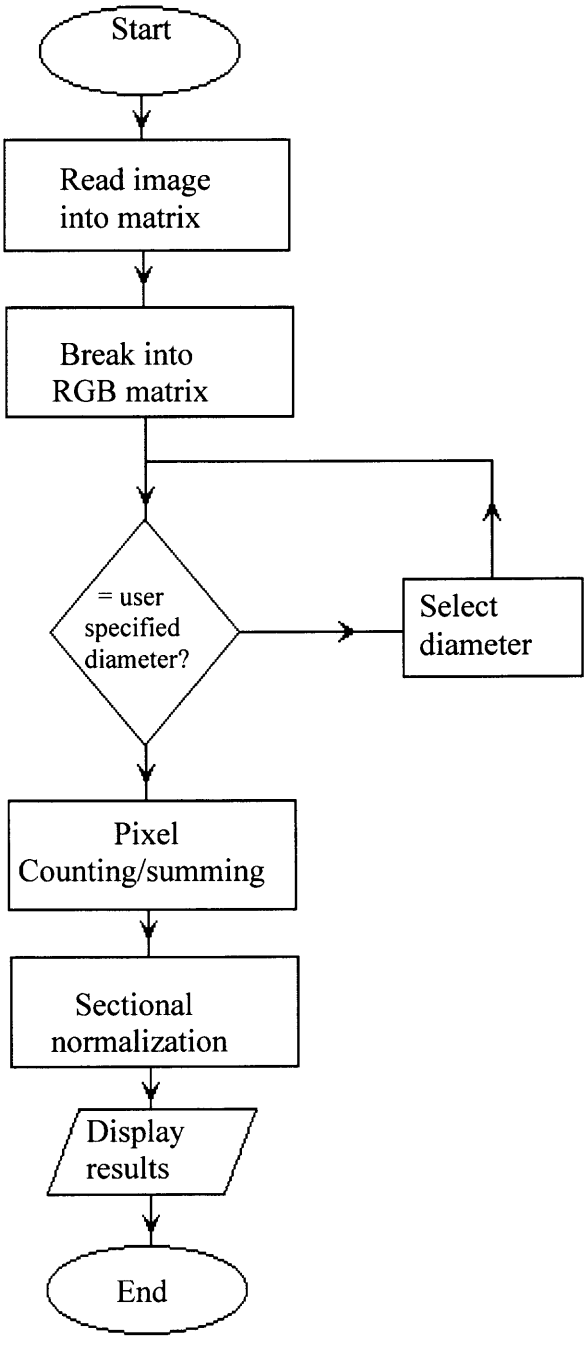


**Figure 3.8** Flowchart for CCD imaging analysis.

### 3.3.3 Endoscope 2-D PIET Experimental Setup

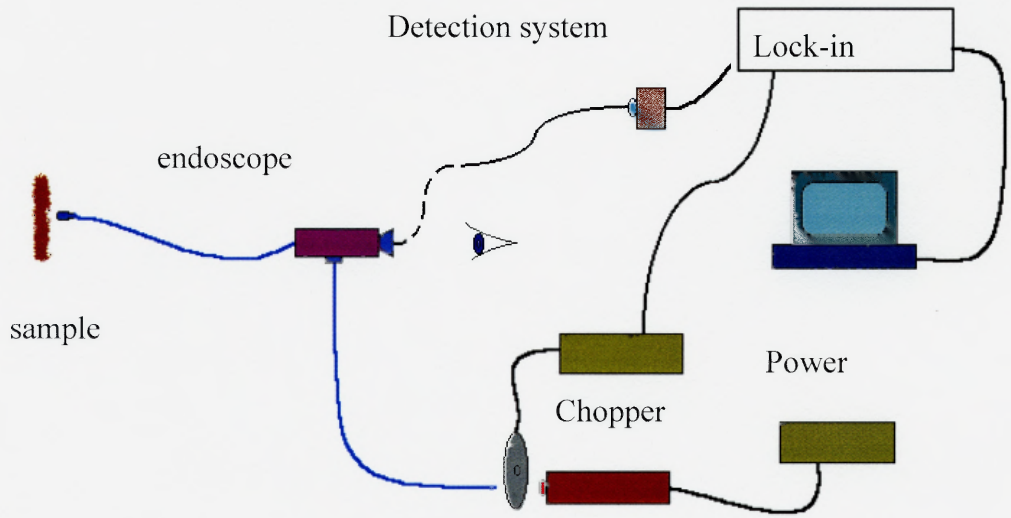


**Figure 3.9** Endoscopic experimental setup.

The schematic for the endoscope experiment is as illustrated in Figure 3.9 above. The basic design of the endoscope experiment is to couple the light through the endoscope's built-in optical fiber light inlet after passing thru a mechanical chopper, for phase lock detection method as described before. The light source beam needs to be collimated by an aspheric lens 1 and then focused to the fiber by lens 2, via a Newport prepackaged setup. The light is then transmitted and incident onto the closed soft tissue and its reflection is picked up by the proposed polarization maintaining optical fiber system. The output intensity is in turn captured and acquired by the means of the similar data acquisition system, both for point and CCD array, for further analysis. Using a lens and a Newport XYZ transitional stage optimizes the alignment between the fiber end and the detector. The light emerging from the optical fiber wireguide was imaged and captured by a CCD camera and processed on a computer, later.

### 3.3.4 In-Vitro and In-Vivo Materials Investigated

For measurement material, several kinds of materials were investigated based on the availability and meeting with the selection criterion that will be described below for different type of sample. They includes both non-biological and biological samples.

**3.3.4.1 Non-Biological Sample.** The selection of non-biological materials (including non-latex rubber PVC examination gloves, latex work gloves, Clean-room standard glove, 3M artificial skin graft, and various plastics bag) eliminates any complications due to the multilayer structure or viscoelastic[2] biological soft-tissues such as skin. The stretch on the material is applied only in one direction: parallel to the plane of incidence. Stretches were applied to both sides of the material at a time to keep the same location under illumination and to maintain a homogeneous stretch field.

**3.3.4.2 Biological Sample.** In-vitro experiments were performed on pigskin samples taken from the animals' sides. Three-way cross Yorkshire-Duroc-Hempshire (25 pound weight) pigskin samples were obtained from an outside source (Buckshire Corporation, Perkasie PA). Other, pigskin samples from the animal's shoulder part that was frozen and refrigerated after sacrificed were supplied from a local butcher shop were also investigated for reproducibility. The advantages of in-vitro specimens were; easy to obtain, prepare, and manipulate; moreover they are not subjected to respiration and positioning artifacts. Unfortunately, the in-vitro specimens do not reflect the perfusion and tissue conditions in-vivo. The effective attenuation obtained in-vitro at 630 nm, based on interstitial measurements, are generally larger than the in-vivo values. At 514 nm

where hemoglobin and possibly myoglobin absorption is high, the attenuation by perfused in-vivo rabbit muscle compared to in-vitro values was; 4.5-7.7 $cm^{-1}$ ratio to 2.0-10.0 $cm^{-1}$.[55] Human forearm, abdomen and back skin were chosen for the in-vivo testing specimens, since the stretcher, both manual and automated, can be adapted to these skin areas with ease.

### 3.3.5 In-Vitro Specimen Preparation

In-vitro samples were taken from a single Yorkshire-Duroc-Hempshire pigskin sample were shaved and delivered in saline solutions on the same day after the animal was sacrificed. In-vitro specimen that were refrigerated and/or frozen, were allowed to thaw at room temperature, before being prepared like the un-refrigerated sample. The caveat is that thawing reduces the tissue water content.

In order to obtain a repeatable data set, the pig spine orientation is used as an anatomical landmark. The fatty tissue is completely removed from the backside of the samples. Square samples are taken from the skin piece where one side of the rectangle is taken parallel to the spine. The size and the orientation of the samples are marked on the animals with soft plastic templates with waterproof markers before they are sacrificed. The samples are placed such that the side of the rectangle parallel to the spine is always parallel to the axis of the device where two micrometers are aligned. The detail description of the stretcher device and its diagram described here is found in the next chapter on manual implementation experiments. Initially the samples are attached to the device with the micrometer positions adjusted until the sample is set to its original length (in-vivo). The samples are stretched parallel to the spine orientation and then back to the original position. During the experiments, the backside of the skin (the side facing the

Plexiglas, plate of the stretching device, see Chapter 4 for more details) is kept wet with saline solution (pH 7.4) to minimize the friction between the two materials and eliminate the drying of the skin, hence constantly maintaining them moisturized.

Skin samples are stretched by equal displacement with the two micrometers. This allows the center of the sample to be stationary with respect to the stretch device. The support rods allow the skin to slide during the stretch and constrain the central portion of the skin to be subjected to a uniform deformation field parallel to the stretch. During the measurements, laser light is reflected from this central portion of the skin.

### 3.3.6 In-Vivo Specimen Preparation

Before each measurement, any hair, which might interfere with the measurements, was shaved with moisturizer and washed with distilled water before the experiment and each subject's skin was also wiped with alcohol. The subject performed the experiments at the approximate same time of the day under similar controlled environment (i.e. temperature) and skin moisture content. When successive or repeated measurements were taken, the skin was allowed to relax and return to the initial state. The subject was allowed to rest and relax the skin surface for a consistent amount of time while the subject skin was treated with alcohol wipes between each measurement. It was found that the longer time intervals given between the cycles would reduce the effect of viscoelastic deformations and thus reduces the experimental uncertainty and scatter in the data.

# Chapter 4

# IMPLEMENTATION

## 4.1 Introduction

The experiments implemented manually with in-vitro samples both non-biological and biological samples are first discussed. After that experimental results with coherent and in-coherent source are presented, which yields the lateral or spatial resolution of the 2-D polarization imaging elastometry technique. This is followed by, a brief description of the automation processes and in-vitro biological results. Results of human forearm specimens on the same day and different days trials are presented. Subsequently, experiments with different wavelength sources were also performed on biological samples. Experiments and procedure with different burnt duration on in-vitro biological specimen results are also presented.

## 4.2 Manual Implementation Experiments

A simple device was first built to apply stretch manually to skin pieces, as shown in Figure 4.1. The four sides of rectangular skin samples are clamped onto a Plexiglas stretching device. Two adjacent clamps can move with respect to the Plexiglas plate by use of infinite screws. The skin is held on the Plexiglas piece by two adjacent plastic pieces that are orthogonal to each other. The plastic pieces are attached to the Plexiglas piece by thumb screws. The skin is placed on an 8.9 cm x 8.9 cm area. The middle part of the Plexiglas plate is covered with a dull non-reflective, black, thin plastic piece. This plastic piece eliminates any reflection from the Plexiglas surface.

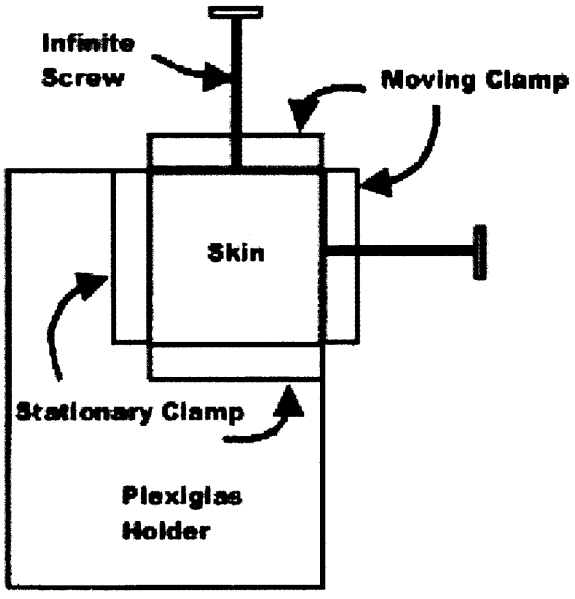


**Figure 4.1** Skin holder. Stretches were applied manually, thru the clamps by turning the infinite screws.

Another simple manual device was built to apply stretch to the sample piece as shown in Figure 4.2. Two opposite sides of the rectangular sample are attached to the micrometers using plastic clamps. One of the plastic clamps is attached to the micrometer and the skin is held between the two clamps by thumbscrews. The distance between the clamps is 77mm. The other sides of the sample are run through a metal cylindrical rod via 2mm diameter holes that are punched along the sides of the sample. When the sample is stretched an equal amount with the micrometers these rods prevent the center of the sample from contracting and moving toward the center of the device (lateral contraction). The distance between the supporting cylindrical rods is 90mm. The middle part of the Plexiglas plate is covered with a dull (non-shining) black thin plastic piece. This plastic piece eliminates any reflection from the Plexiglas surface. This device was also used for in-vitro pigskin experimentation, because of its uniformity stretch direction/application.

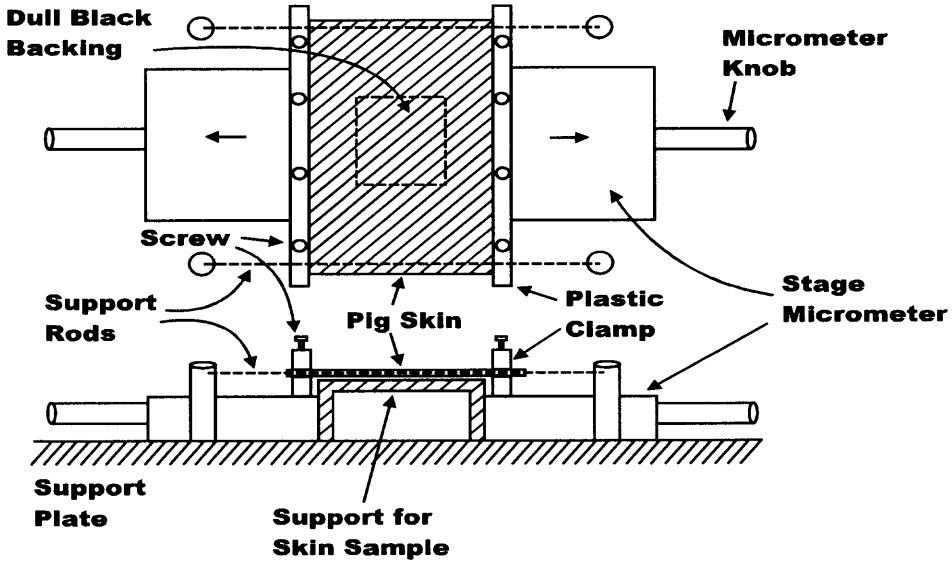


**Figure 4.2** 1-D micrometer stretchers mount.

### 4.2.1 Biological Experimental Results

Four guinea pig skin samples, Hartley Guinea pigs, 500 to 550 g were used in this experiment. The samples were prepared according to the description layout in the above subchapter 3.3.5. Owing to the preliminary nature of the simple skin-holder device, in Figure 4.1, the stretch in one direction did not create a completely uniform deformation because the other sides of the skin parallel to the stretching direction were also clamped and could not follow the deformation uniformly. However, the central portion of the skin is subjected to a uniform deformation field that is parallel to the stretching direction. During the measurements laser light with a spot size of approximately 2 mm is reflected from this central portion of the skin. Various amounts of stretch, to as much as 1.5 cm (17%), are applied to the 8.9 cm by 8.9 cm samples. The infinite screw is turned between measurements by hand. After the maximum stretch is reached, the skin sample is released to return to its original position with the same protocol.

Some viscoelastic deformation takes place during the experiments. Usually the skin samples did not recover their original positions because of the viscoelastic deformations and also, because of the friction between the Plexiglas surface and the skin, although this surface was kept wet with saline solution.

Experiments on four skin samples from four different animals with a laser wavelength of 488 nm show that, when stretch is applied to samples of guinea pig skin samples taken parallel to the spine, a nearly linear relation between the amount of stretch and the reflected light intensity is measured, as shown in Figure 4.3.

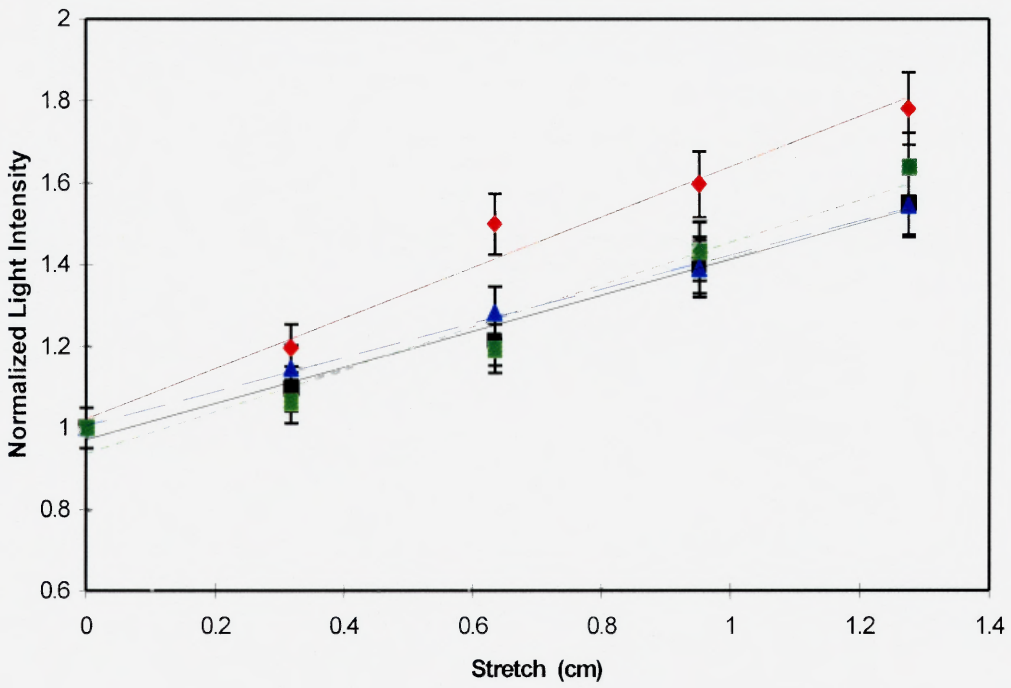


**Figure 4.3** Guinea pig skin results with X-Y stretcher.

In Figure 4.3, the incident light was polarized perpendicularly to the plane of incidence and the spine direction. As with the standard 2-D polarization technique, the net reflected light intensity is computed by taking the difference between the two

perpendicular components of the reflected light, i.e. the component parallel to the polarization of the incident light minus the perpendicular component. The intensities were then normalized with respect to the unstretched intensity. Similar results are obtained for incident light that is polarized parallel to the plane of incidence. The standard deviation method was used to estimate the error of all the experimental data measured. The error is represented by the vertical error bar in all of the subsequent experimental result graphs.

Because of viscoelastic deformations and residual friction between the skin and the Plexiglas, the skin samples did not recover their original reflectivity when returned to their original positions after stretching. Consequently, the absolute measured reflectivity for a particular stretch position would depend on prior stretching. However, the *slope* of the normalized reflectivity versus the stretch remained nearly the same for all four samples. Repeated measurements on the same sample yield roughly the same slope with a slightly decreasing value with repeated stretches. This effect is probably due to material fatigue.

**Table 4.1** Least Squares Fit method slopes of the guinea pig skin normalized reflectivity vs. stretch (cm) graph

| **Guinea pig skin** | **Gradients of normalized reflectivity vs. stretch ($cm^{-1}$)** |
|---|---|
| 1 | $0.616 \pm 0.055$ |
| 2 | $0.441 \pm 0.031$ |
| 3 | $0.417 \pm 0.012$ |
| 4 | $0.517 \pm 0.064$ |

The slopes of the normalized reflectivity, as determined by a least-squares fit, for the four samples shown in Figure 4.3 are as tabulated in Table 4.1. Clearly, the data are reproducible from sample to sample.

Similar samples were also stretched with the second device by hand, on the same experimental configuration. They all exhibit a linear relationship between the measured reflectivity and the amount of stretches applied. A typical result is as plotted in Figure 4.4. The slopes calculated with linear regression least squares method is 0.0404 $mm^{-1}$ with $R^2$=0.9908. An initial flat response region below stretches of 2 mm is due to slack in the sample. As the sample stretches, the slack disappears. The straight line is the best-fit linear regression line to the data points.

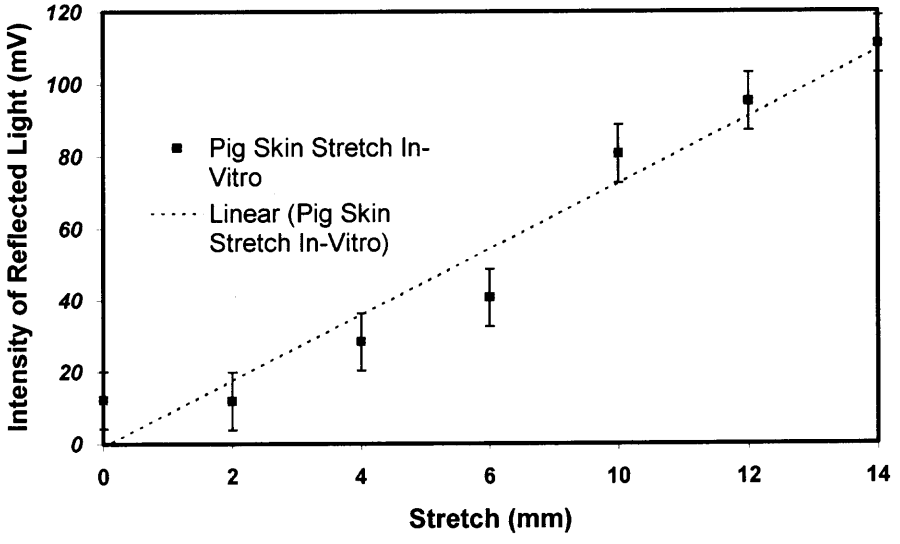


**Figure 4.4** Reflectivity results of pigskin stretched by the 1-D micrometer stretcher.

### 4.2.2 Non-Biological Experimental Results

It was proposed in the theoretical model of Chapter 2 that interface roughness is responsible for the change in reflectivity with stretching. If this is true, one would expect

that the increase in reflection with stretching to be a *general* property of soft, stretchable materials and not to be restricted to biological tissues such as skin. To test this hypothesis, measurement of the change in reflectivity of two different plastics as a result of stretching were made. The results observed and measured are as shown in Figure 4.5, Figure 4.6 and Figure 4.7. In the cases, that the error bar or the experimental error calculated with the standard deviation method is much smaller than the symbols used to represents the data point, the corresponding vertical error bar will not be noticeable.

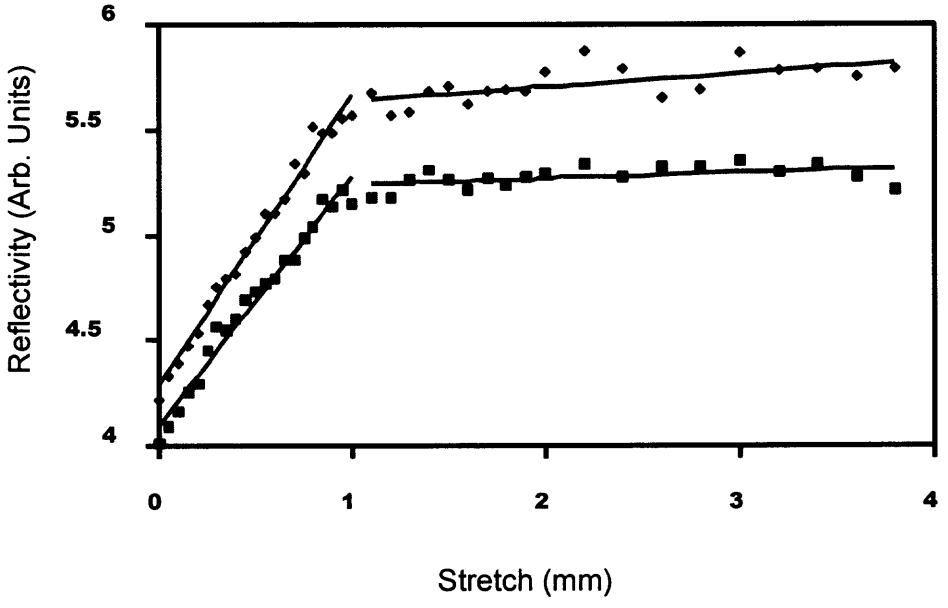


**Figure 4.5** Reflectivity vs. stretch plot of a piece of stretched latex examination glove.

The samples un-stretched length was 45 mm. The geometry of the stretch and the light polarization is the same as is shown for Figure 4.3. Shown is the reflected light that is polarized parallel, which is identified by diamonds pattern on the upper curve and perpendicular, with squares pattern on the lower curve to the polarization of the incident light. The maximum change in reflectivity caused by stretching is approximately 35%. The maximum stretch was approximately 8.4%. The solid curves represent least-squares

linear fits to the data for stretches of less than 1 mm, with the slopes of 1.37 ± 0.04 $mm^{-1}$ and 1.19 ± 0.04 $mm^{-1}$ for parallel and perpendicular polarization, respectively and for stretches of more than 1 mm, the slopes were 0.065 ± 0.018 $mm^{-1}$ and 0.028 ± 0.013 $mm^{-1}$, respectively.


**Figure 4.6** Normalized reflectivity vs. stretch obtained by use of the least-squares fit results.

In both cases, a linear change in reflectivity with stretching is observed. However, for stretches longer than approximately 1 mm, the slope of the reflectivity for the sample shown in Figure 4.5 becomes much flatter. The straight lines in Figure 4.5 are linear regression fits to the data for stretches of less than 1 mm and greater than 1 mm. Figure 4.6 shows the net reflected light intensity i.e., the difference between the two perpendicular components of the reflected light for the fitted regression lines. Figure 4.7 shows the result for a polyvinyl chloride glove. In this case, the sample un-stretched length was measured to be 45 mm. No saturation of the reflectivity was observed with

this sample due to the elasticity property of the material. The line was the fit to the data with a slope of $0.644 \pm 0.018$ mm$^{-1}$.

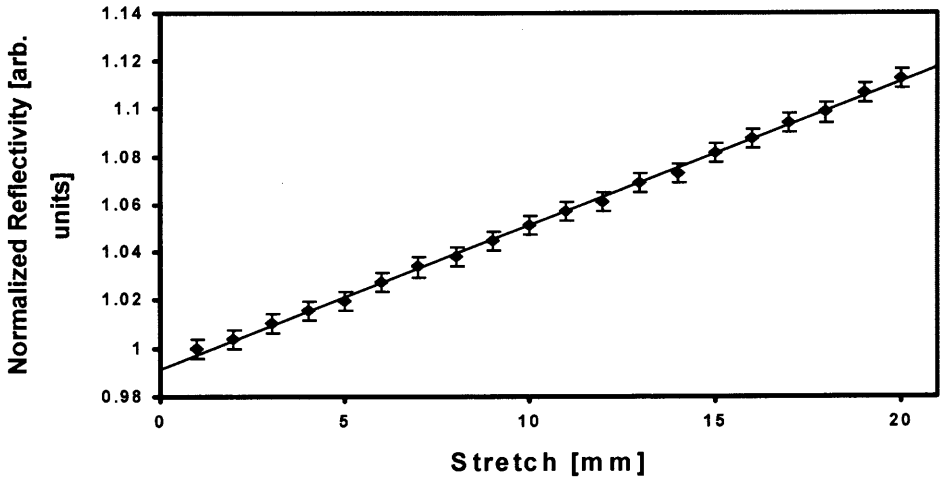


**Figure 4.7** Normalized reflectivity vs. stretch from a polyvinyl chloride examination glove.

Other non-biological materials investigated, also exhibits these linear relationship between the measured reflectivity with the stretch applied. They are as listed in the following Table 4.2 for comparison. The sample is excised and taken from the palm's section of the respective gloves for uniformity when mounting the sample.

**Table 4.2** Typical reflectivity slopes of various non-biological glove investigated

| Type of material | Normalized reflectivity vs. stretch slope (mm$^{-1}$) | Linear correlation coefficient ($R^2$) |
|---|---|---|
| Polyvinyl chloride glove | 0.644 | 0.9980 |
| Latex examination glove | 1.280 | 0.9840 |
| Rubber glove | 1.205 | 0.9962 |
| Latex rubber glove | 0.0089 | 0.9764 |
| Cleanroom glove | 1.1864 | 0.9500 |

### 4.2.3 Coherent and In-Coherent Source Experimental Results -Spatial Resolution

In this sub-chapter, the spatial resolution and stretch resolution of the modified 2-D polarization imaging technique was investigated and determined using stretchable Polyvinyl Chloride (PVC) rubber as the sample under test. The measured resolutions result is compared to state-of-the-art ultrasound and video imaging systems. As will be shown, the modified 2-D imaging technique has a spatial resolution of about 24μm and a stretch resolution of about 0.3%. This spatial resolution is slightly better than ultrasonic imaging and video dimension analyzer[67] and comparable to video motion analyzer imaging methods described here. The inferred strain resolution is comparable to that of the video imaging methods. Assuming that the cameras, which are used for the video techniques and the 2-D polarization imaging technique are equivalent, the spatial resolution of the 2-D imaging technique is determined by three effects;

(a) the area of tissue which is imaged onto one camera pixel,

(b) the characteristic spatial scale of the interface roughness in conjunction with the spatial scale over which Mie Scattering by the tissue is valid, and

(c) the coherence length of the light source (laser speckle).

Next, the detail measurements of the spatial resolution, the accuracy of the stretch measurement, and the influence of laser speckle as a competing optical effect are discussed.

The experimental setup used was, as shown in Figure 3.1, and is similar to that used in previous measurements.[2,63] However, a He-Ne laser operating at $\lambda = 632$nm, with P<5mW was the light source for this experiment. The only different was that the laser light passes through a neutral density filter, a polarizer and was then directed to the

sample surface through a focusing lens. The angle of incidence for the data presented was roughly 45°. Different focal length lenses are used to focus the incident light to 1/e spot sizes ranging from about 1mm, of unfocussed laser light to about 170μm. The lens is positioned such that the sample under test is at the focal point. The reflected light is collected using a lens (f=50mm) after it passes through a second polarizer (analyzer). The collected light is split using a 50% beam splitter and focused onto either a single element silicon photodetector ($2mm^2$ active area) or a CCD digital camera. The angle of the collected reflected light and aperture size is adjusted to collect the light in the specularly reflected direction. The polarization of the incident light and the analyzer can be set in one of two perpendicular orientations: either parallel or perpendicular to the plane of incidence. The reflected power in both the parallel and perpendicular polarization is measured as a function of the incident light polarization and skin stretch. For detection by the single element photodetector, the laser power is detected by mechanically chopping the incident laser light and utilizing a lock-in amplifier with phase sensitive detection. The raw digital image acquisition system consists of a SONY MAVICA™ F-51 CCD camera with a 640X480 pixel array detector.

All data presented here was taken from rectangular pieces of non-latex rubber PVC examination glove. By using the PVC rubber, any complications due to the multilayer structure of skin was avoided in the present experiment. Moreover, since skin exhibits viscoelastic behavior[2], the PVC sample was used to ensure repeatable stretches and reflectivity changes with a minimum of material fatigue. The reproducibility of the PVC samples is desirable for this study since the presence and reproducibility of the linear change in reflectivity with sample stretch is used as a criterion to determine the

stretch/ spatial resolution of the 2-D polarization imaging method. The stretch on the material is applied only in one direction: parallel to the plane of incidence. Stretches were applied to both sides of the material at a time to keep the same location under illumination and to maintain a homogeneous stretch field. A small tension was applied in the perpendicular direction to prevent the sample from wrinkling as it was stretched.

Two methods of light detection are used and compared. In the first technique, the reflectivity is monitored using the single element silicon photodetector in conjunction with the lock-in amplifier. The detected photodetector voltage, which is proportional to the reflected intensity is tabulated and plotted versus the sample stretch. Varying spot sizes of He-Ne laser light were used to illuminate a stretchable PVC rubber. The material was stretched manually at 1mm intervals until 2cm was reached. After each stretch, the voltage of the photodiode is measured using the lock-in amplifier. Trials are done quickly as possible (over a few minutes) to reduce reflectivity changes due to relaxation of the material and to reduce deformations caused by long term tension. Throughout all experiments, the incident light is polarized perpendicular to the plane of incidence. As is done with the 2-D Polarization Imaging Method,[3] the component of the reflected light which was polarized perpendicular to the direction of the incident light was subtracted from the magnitude of the detected reflected light polarized parallel to the incident light.

In the second technique, the reflected light is captured by the digital CCD camera. Two images per stretch position are acquired and stored on a floppy diskette. The image is then transferred to a Pentium II personal computer to be analyzed. The digital image processing algorithms are written using C/C++ and computed using MATHCAD pro 2000. By taking several frames of the same stretching condition, the images of several

frames could be averaged together as to minimize random noise fluctuations of the imaged laser power due to laser speckle. The captured image is then converted into matrices of RGB (Red, Green, Blue) components before being manipulated by the selected algorithm, which is listed in Appendix A. The linear regression correlation results from both the techniques are then compared. A standard brute force method of estimating the spatial resolution was also used.[68]

**4.2.3.1 Point Detection Data.** In order to ascertain the spatial resolution of the polarization reflectivity measurement, varying spot sizes of He-Ne laser light is used to illuminate a stretchable PVC rubber. The results are shown in Figure 4.8 and Table 4.3.

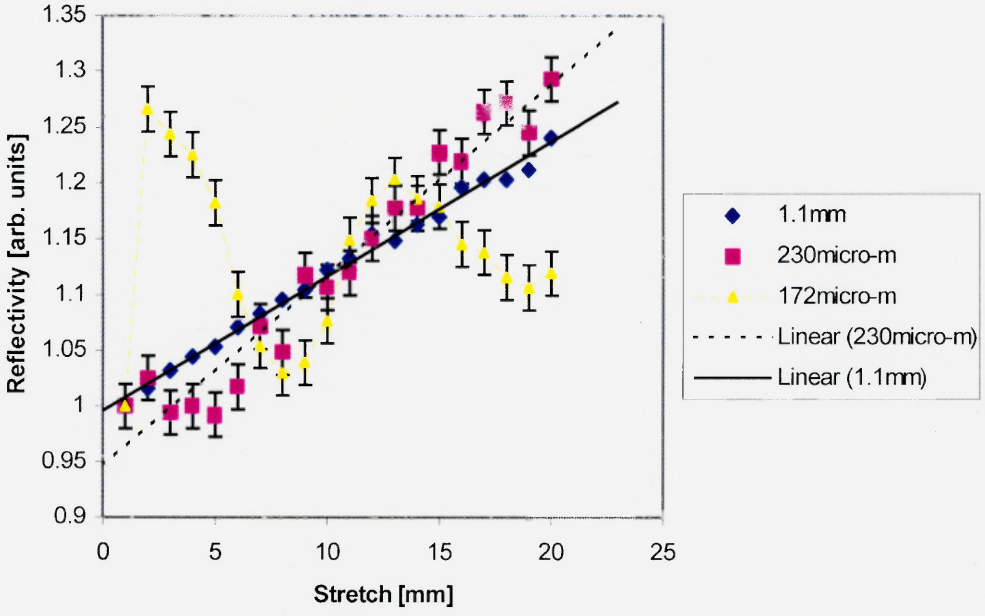


**Figure 4.8** Normalized Reflectivity vs. stretch using a He-Ne laser as the light source. The straight lines are linear fits to the data.

With stretch, the reflected light in the specular direction increased linearly. However, as the spot size of illumination decreases to about 170-200μm, the linear

dependence with stretch as measured by the linear correlation coefficient becomes less prevalent indicating a spatial resolution limit. The spot size is reduced either by a single lens or by a collimator consisting of two lenses. In the single lens configurations, the lens is placed a distance $f$ from the material, where $f$ is the focal length of the lens. The spot size at the focus is determined by standard Gaussian beam propagation equations.

The initial size of the beam before focusing is measured to be $D_o$ = 1.1mm (1/e spot size). To estimate the laser spot size D on the sample, the following equation is used

$$D = (2\lambda f)/D_o \tag{4.2.1}$$

where $\lambda$ is the wavelength of the light and $D_o$ is the width of the incident beam upon the lens.

**Table 4.3** He-Ne laser spot size and corresponding slope as determined by linear regression of the data. The nonlinear behavior, as shown in Figure 4.8, indicates that the spatial resolution is between 172-230μm for coherent source

| Spot Size | Slope ($mm^{-1}$) $\times 10^{-2}$ | Linear Correlation Coefficient |
|---|---|---|
| 1.1mm | 1.201±0.025 | 0.99620 |
| 396μm | 1.846±0.077 | 0.98482 |
| 310μm | 1.725±0.116 | 0.96156 |
| 264μm | 1.429±0.197 | 0.86339 |
| 230μm | 1.712±0.094 | 0.97409 |
| 172μm | Not linear | |

Trials with varying spot sizes are shown in Figure 4.8. The data is normalized such that the first data points for all curves have a reflectivity value of 1 in arbitrary units. Note the increased deviation from linear behavior as the laser spot size is decreased. Until

the spatial resolution is surpassed, all trials give slopes close in magnitude as shown in Table 4.3. Included in the figure are three trials: unfocused light, immediately before the resolution limit, and immediately after the limit. The slopes of the reflectivity versus stretch curves are determined by a linear fit to the data. The data for the smallest spot size of about 172μm shows no linearity.

One possible limitation to the spatial resolution is laser speckle due to the long coherence length of the laser. In order to test the effect of laser speckle, the He-Ne laser source is replaced with a red light emitting diode (LED, λ=635nm). The reflectivity versus stretch data is shown in Figure 4.9.

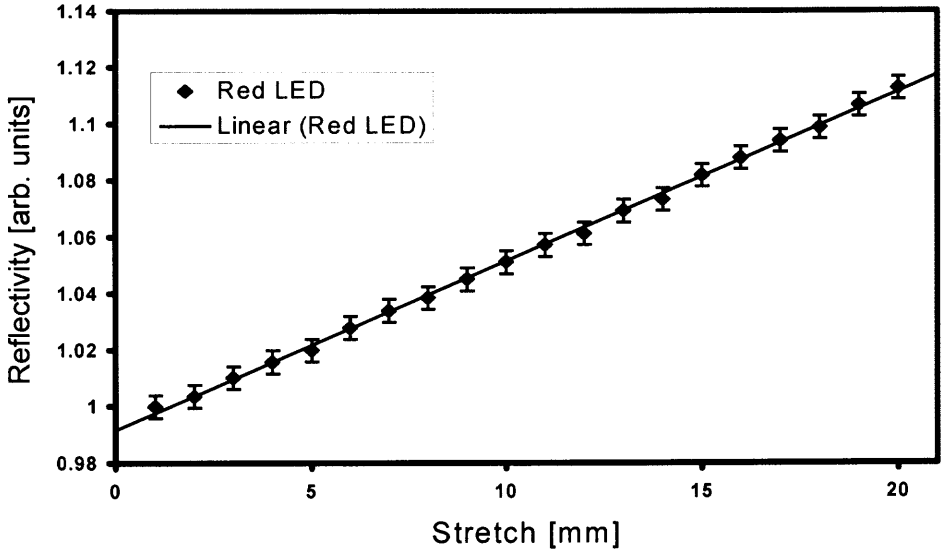


**Figure 4.9** Measured reflectivity vs. stretch using a red LED as the light source.

The LED light is focused down to a spot size of 3mm on the sample (99% power) and mechanically chopped and detected using a lock in amplifier and phase sensitive detection. A particularly noticeable difference between the trials in Figure 4.8 and Figure 4.9 is that the LED gives much better linearity. The slope of LED data is

$(5.994\pm0.047)\times10^{-3}$ $mm^{-1}$. The spot size is roughly 3mm (99% power). The slope as determined by linear regression has an uncertainty, which is an order of magnitude less than that obtained with a He-Ne laser. It is suspected that the lower noise is due to the incoherent nature of the LED source compared to the laser.

As will be discussed below, due to the different optical components, which are used to focus the LED and He-Ne light onto the sample, one cannot directly compare the absolute slope values. However, the uncertainty in the slope, about 1%, is about an order of magnitude smaller than the trials with the laser.

The stretch resolution can be estimated using the 1.1mm spatial resolution data for the He-Ne laser. For a fixed stretch position, the detected light has a measured power fluctuation of about 0.39%. For a slope of $1.201mm^{-1}$, this corresponds to an uncertainty in stretch of about $\Delta x/x = 0.32\%$. For an unstretched material length of 78mm, this uncertainty corresponds to an uncertainty of about 0.25mm.

**4.2.3.2 CCD Imaging measurements.** For the CCD imaging measurements, the sample is illuminated with an unfocussed laser beam. The angle of incidence and incident polarization are the same as is used for the single element detector measurements. To ensure a linear detector response, the automatic shuttering feature of the camera is disabled so that the shutter speed is fixed. In addition, the power to the camera is not left on in between data acquisitions in order to minimize the shot noise and dark current in the camera. The linearity of the CCD camera is confirmed prior to and during measurements.

As with the standard 2-D polarization imaging technique and the Si photodetector measurements discussed above, the detected light polarized perpendicular to the polarization of the incident light was also subtracted from the intensity of the detected light polarized parallel to the incident light. As was observed for single element detection measurements, the perpendicular component of the detected light does not change with stretch.

The digital images were analyzed by thresholding the illuminated areas via pixel counting across the specimen.[3] For image analysis, several algorithms were tested.[68] For the data presented here, the algorithm employed is commonly utilized to analyze images with laser speckle. In this method, the total detected laser power within a specified area is calculated by summing the pixel count for all pixels within the specified area and dividing by the total number of summed pixels. In applying this technique to measured data in order to estimate the spatial resolution of the 2-D polarization imaging technique, the detected power as a function of stretch is calculated from the CCD images by averaging the pixel counts within a certain radius of the center of the beam profile.

Various diameters are used corresponding from 3 pixels across to 350 pixels across an equivalent spot size. The corresponding spatial resolution is calibrated by measuring the width in pixels of the illuminated spot size on the sample (2mm diameter for 99% power). The 2mm illuminated spot has width of 350 pixels, which computes a 5.7 μm/pixel resolution. As an example, the 4.8% diameter corresponds to an image 17 pixels in diameter or a spatial resolution on the sample of roughly 97μm.

The slope of the summed reflected power versus stretch curve is determined by linear regression. Typical results are as tabulated in Table 4.4 for the He-Ne laser source.

**Table 4.4** He-Ne source. Spatial resolution, slope, and linear correlation coefficient for the CCD reflectivity data shown in Figure 4.10, Figure 4.11, and Figure 4.12

| **Diameter of area for Average Power** | **Spatial Resolution (μm)** | **Slope($mm^{-1}$)** | **Linear correlation R** |
|---|---|---|---|
| Data from point detector | 2000 | 0.346 | 0.998 |
| 0.857% 3 across | 17 | 0.360 | 0.147 |
| 1.428% 5 across | 28 | 0.415 | 0.232 |
| 3.714% 13 across | 74 | 0.373 | 0.538 |
| 4.857% 17 across | 97 | 0.408 | 0.650 |
| 6% 21 across | 120 | 0.345 | 0.671 |
| 11.714% 41 across | 234 | 0.335 | 0.856 |
| 14.571% 51 across | 291 | 0.291 | 0.861 |
| 18% 63 across | 360 | 0.385 | 0.960 |
| 20.286% 71 across | 406 | 0.267 | 0.842 |
| 30% 105 across | 600 | 0.335 | 0.950 |
| 40.286% 141 across | 806 | 0.406 | 0.972 |
| 50% 175 across | 1000 | 0.409 | 0.982 |
| 70% 245 across | 1400 | 0.376 | 0.983 |
| 80.286% 281 across | 1600 | 0.332 | 0.970 |
| 90% 315 across | 1800 | 0.272 | 0.943 |
| Whole picture with background | 2000 | 0.209 | 0.886 |

The imaging data in Figure 4.10, Figure 4.11, and Figure 4.12 show that as the radius of pixel summing is increased, the average summed power decreases. This is to be expected since as the diameter of the summed area increases, the contributed power per

pixel decreases due to the roughly Gaussian beam profile, which illuminates the surface. Additionally, as the radius of the summed area increases, the quality of the linear fit improves.

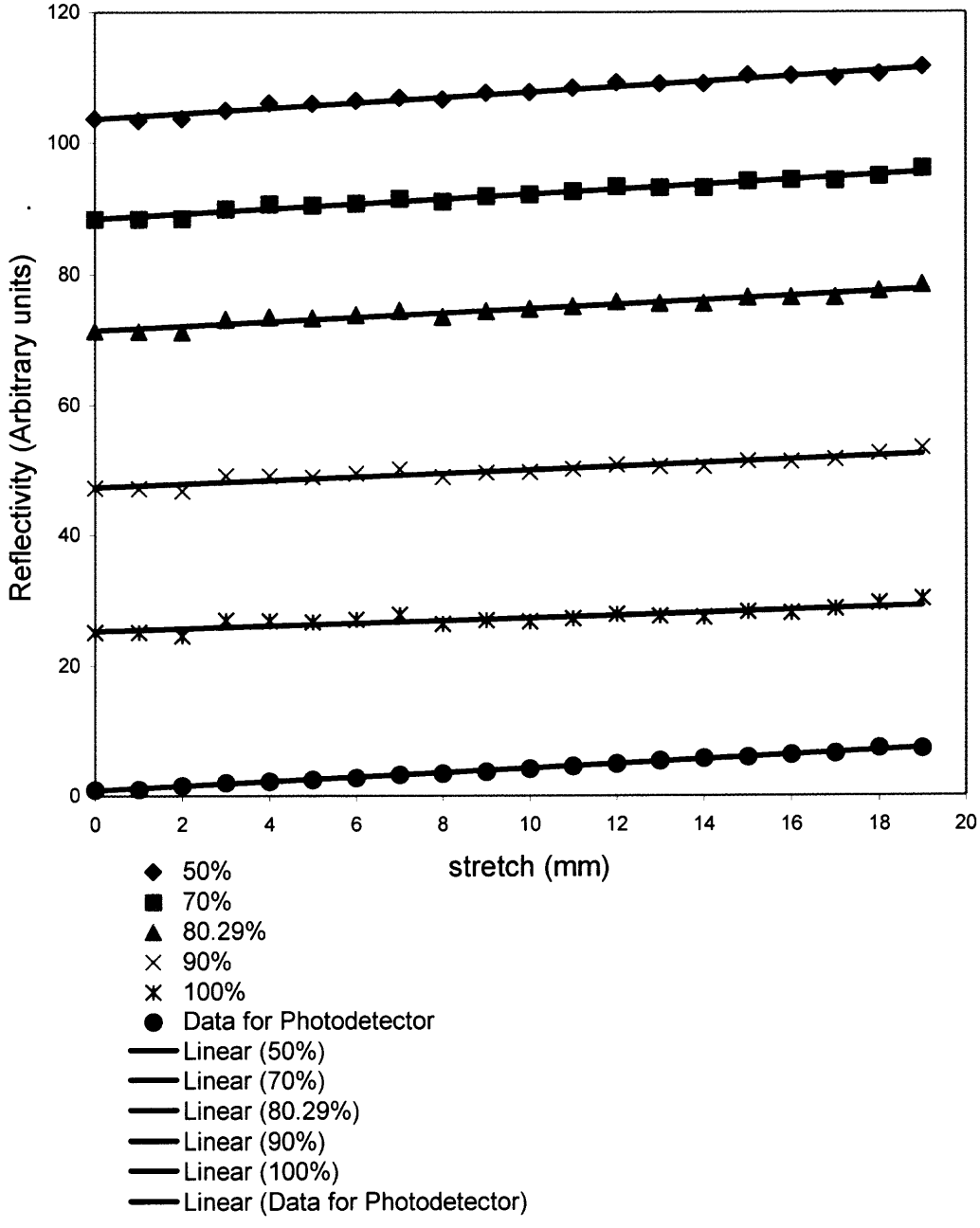


**Figure 4.10** CCD imaging data averaged over a percentage (100%-50%) of the imaged illumination spot on the sample.

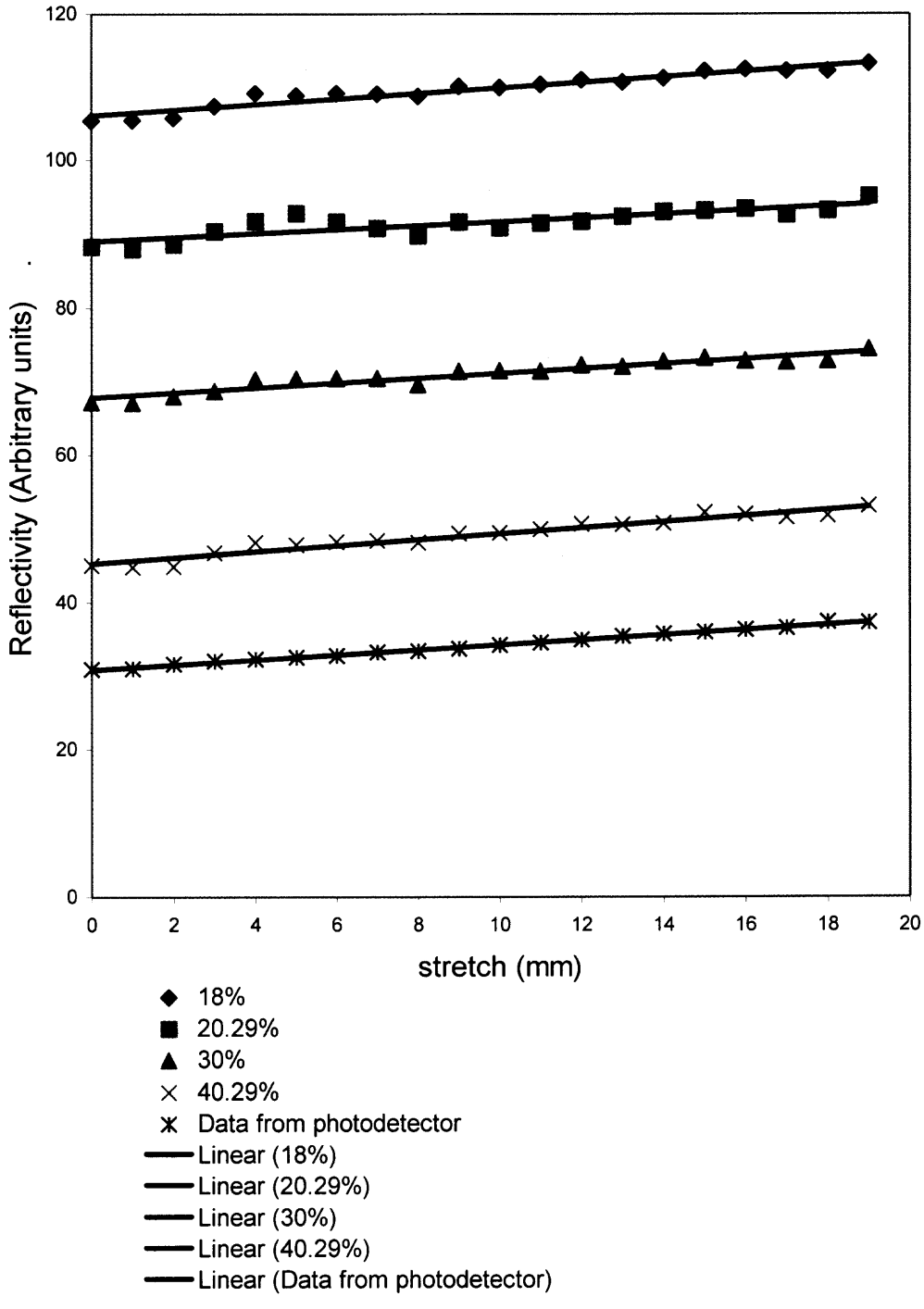


**Figure 4.11** CCD imaging data averaged over a percentage (40%-18%) of the imaged illumination spot on the sample.

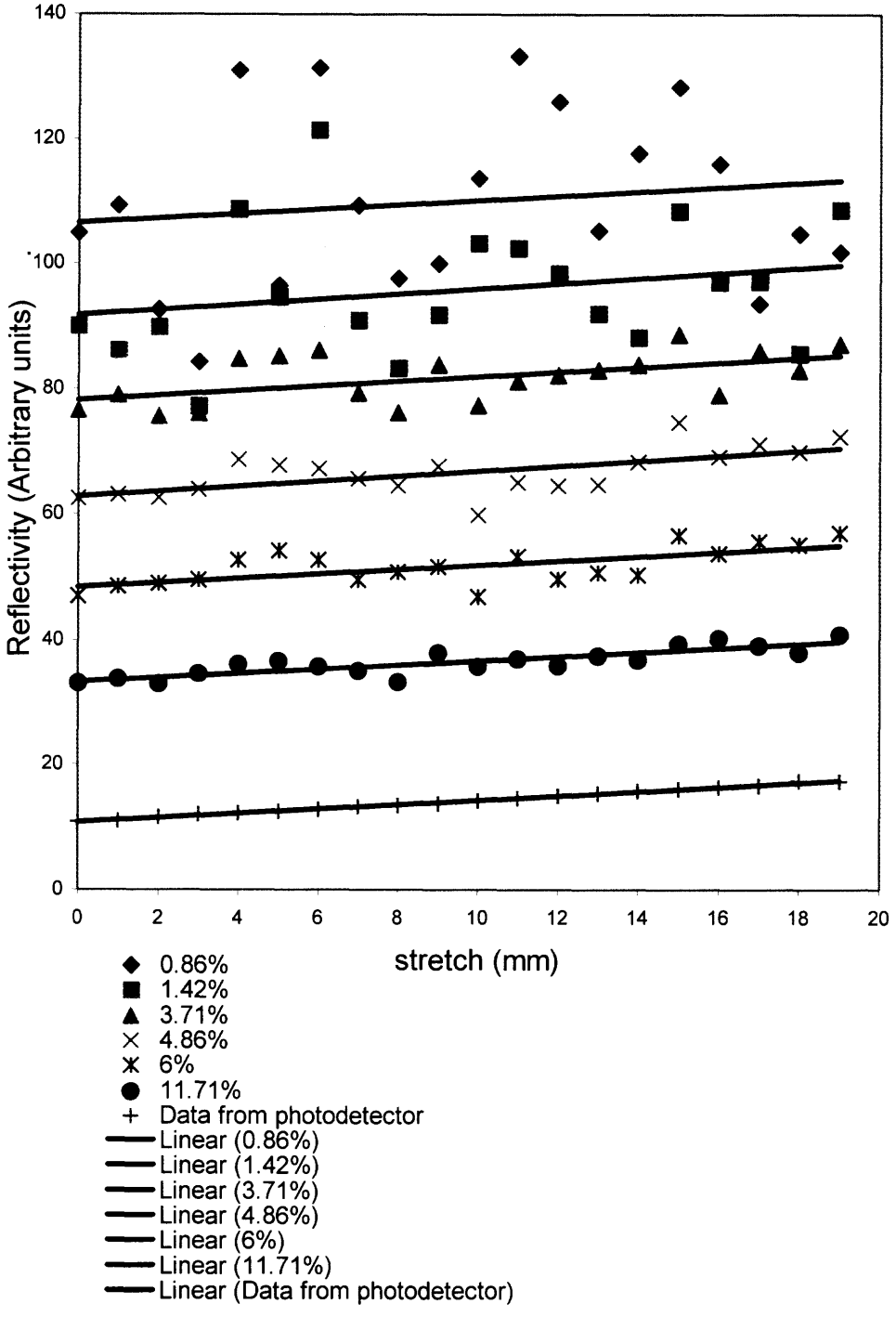


**Figure 4.12** CCD imaging data averaged over a percentage (12%-0.8%) of the imaged illumination spot on the sample.

As will be discussed below, the improvement in the linear fit may be due to the averaging out of laser speckle. As the pixel averaging area decreases, Table 4.4 and in Figure 4.13, the linear correlation coefficient gradually decreases and then sharply drops for a spatial resolution of 120μm. The rapid reduction of the linear correlation coefficient for spatial resolutions in the range of 120-234μm suggests that the spatial resolution of the 2-D polarization imaging is in this range as well. This range of 120-234μm is consistent with the 200μm resolution as estimated using the single element detector for coherent source.

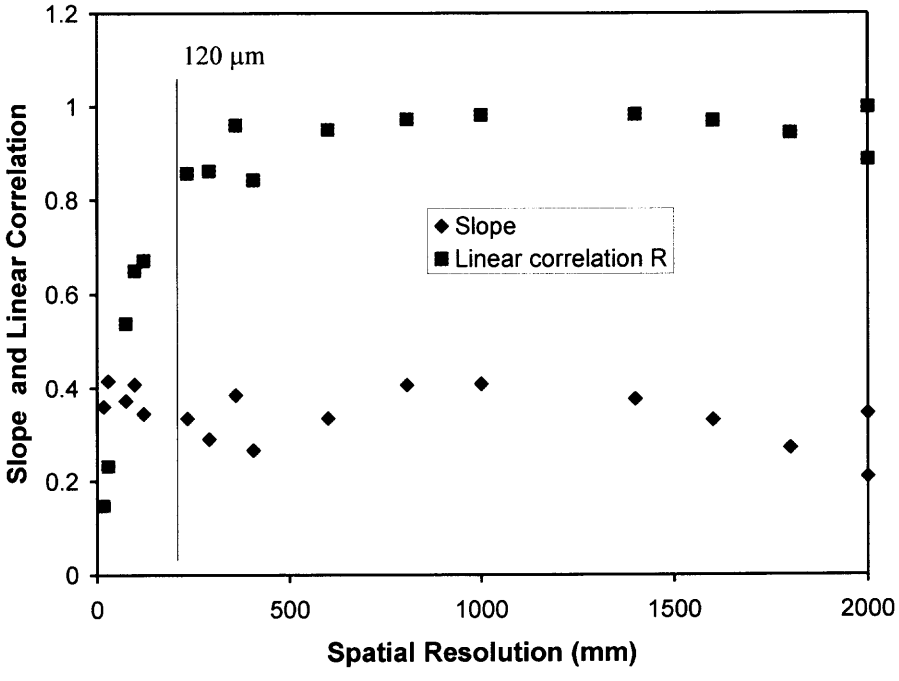


**Figure 4.13** Plot of data shown in Table 4.4.

In order to determine the effect of laser speckle on the CCD detection system, spatial resolution, the He-Ne laser was again replaced with an incoherent red light emitting diode (LED, λ=635nm). The data for the LED light source is presented in Figure

4.14 and Figure 4.15. The drop in the linear correlation coefficient near a spatial resolution of 24μm suggests that the spatial resolution of 2-D polarization imaging with the LED source is comparable to this value.

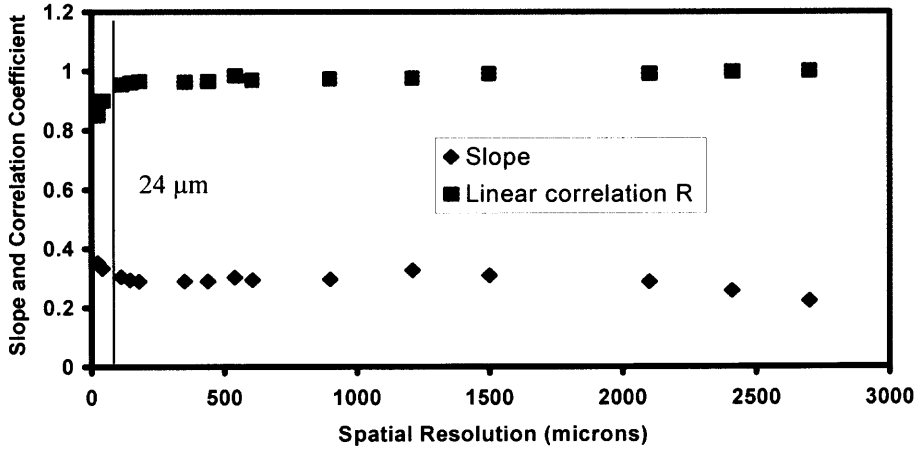


**Figure 4.14** CCD data with Red LED Source: Results of spatial Resolution versus slope and linear correlation coefficient.

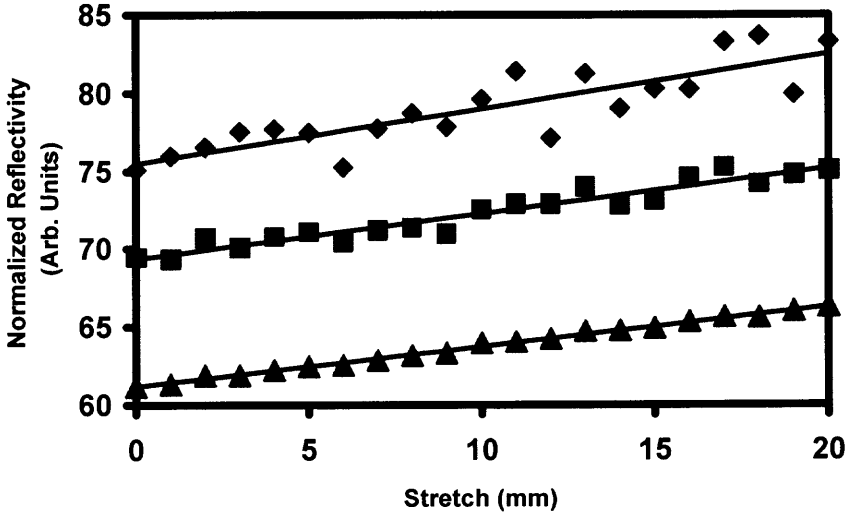


**Figure 4.15** Reflectivity data for red LED source for 3 different spatial resolutions 24μm, 145μm, & 2400μm from top to bottom. Straight lines are linear regression fits to the data.

## 4.3 Automated Implementation Experiments

The manual actuation of the stretcher is a time consuming and tedious tasks. From the experimental data measured manually as described and shown in chapter 4.2, the number of data point collected is not sufficient to provide accurate representation or show enough evidence of the linear trend that exists between the reflectivity and stretch introduced. This prompted for the need to increase the number of data point measured for each trials, and hence the need to computerize and automate the data acquisition process.

### 4.3.1 Hardware Implementation

With that in mind, the stretcher were redesigned and refitted with accurate motion controlled stepper motors. They were then interfaced and controlled by a personal computer equipped with either the GPIB or DAQ interface card. New stepper motor controlled translational stages were also used for more finite step size and longer travel displacement.

### 4.3.2 Software Implementation – Labview

The stretcher motion were furthermore controlled with the corresponding Labview program written with reference to the help of timing diagram, so that there is no timing issue and data buffer aliasing. The corresponding working Labview programs are listed in Appendix B, for reference. They include the program that control the Stanford Research SR510 analog lock-in amplifier, EG&G 7260 DSP lock-in amplifier, Klinger CC 1.1 stepper motor controller, Newport ESP300 stepper motor controller and National instrument DAQ or GPIB card. The program for all the lock-ins included the autophase

and autosensitivity algorithm for optimum and ease of use during experimentation. The corresponding program logic for the Labview automation is as shown in Figure 4.16.

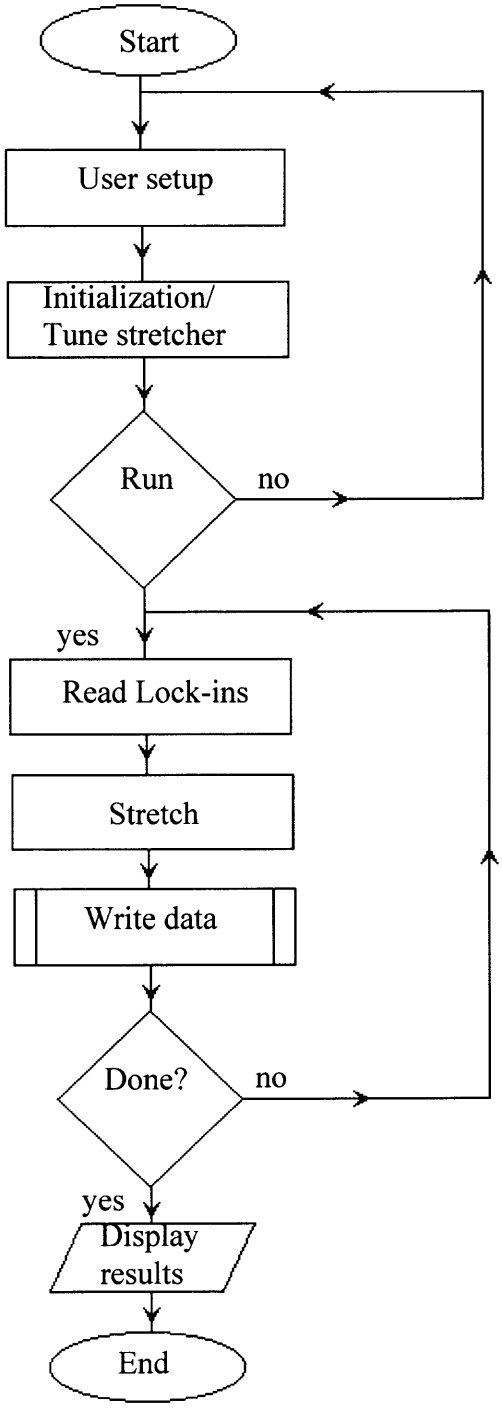


**Figure 4.16** Flowchart for Labview automated implementation.

### 4.3.3 Biological Experimental Results

**4.3.3.1 In-Vitro Pigskin.** The computer-controlled stretcher has a spatial resolution of ± 1μm, with accurate motion precision. Using a typical step size of 100 μm, additional in-vitro experiments are performed on pigskin samples that were taken from the animals' shoulder section. The device built to apply stretch to the skin piece was similar to the stretcher shown in Figure 4.2. Two opposite sides of the square (70mm x 70mm) skin sample are attached to the computer controlled translation stages using plastic clamps. The distance between the clamps is 57mm. The other sides of the sample are run through a metal cylindrical rod via 2mm diameter holes that are punched along the sides of the sample. When the skin is stretched an equal amount with the translation stages these rods prevent the center of the skin from contracting and moving toward the center of the device (lateral contraction). The distance between the supporting cylindrical rods is 90mm. The middle part of the Plexiglas plate is covered with a dull (non-shining) black thin plastic piece. This plastic piece eliminates any reflection from the Plexiglas surface.

Numerous experiments were performed on the animal's shoulder skin section. Attention was paid when selecting and mounting the samples to conform with the medical criterion, in particular, mounting the skin so that the stretch direction would be parallel to the animal's spine orientation. It is interesting to point out that the observed reflectivity results measured by the PIET are quite reproducible day from day regardless of animals. It is also reported that the initial stretching, typical value below of about 1mm, was to removes any sagging in the sample. This is be due to the skin mounting and clamping procedure on the stretcher. The linear reflectivity versus stretch is observed for

intermediate values of stretch. For large values of stretch, the reflectivity saturates as the skin roughness has been flatten and reduced to a uniform flat interface. A good representation of the described phenomena of two different animals is as shown in the Figure 4.17 results below.

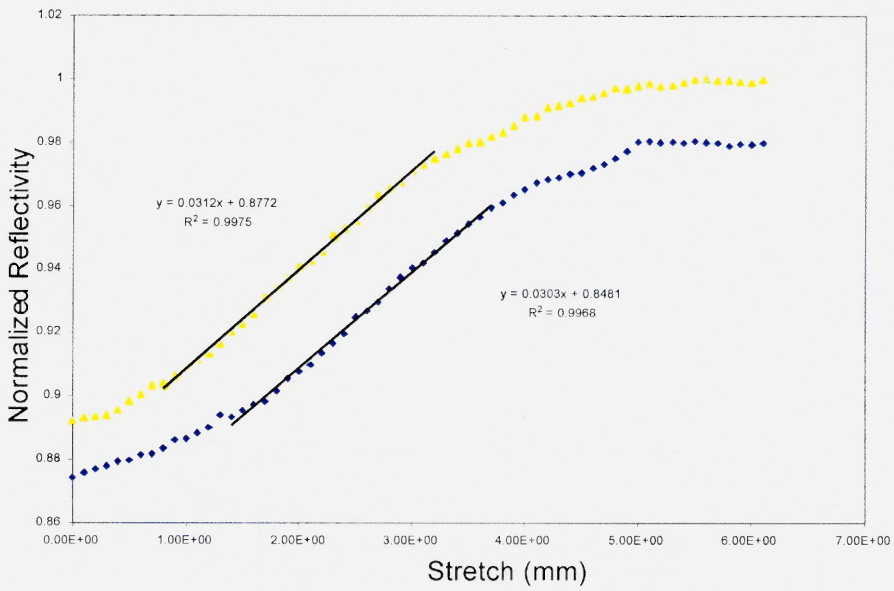


**Figure 4.17** Normalized reflectivity vs. stretch for pigskin (shoulder) from two different animals. The bottom curve is offset for by 0.02 for clarity.

The observed linear regression slopes of all the animals' are sampled to within the experimental uncertainty and will not be tabulated. The two slopes computed from the above Figure 4.17 are 0.0312 $mm^{-1}$ with linear correlation $R^2$ of 0.9975, and 0.0308 $mm^{-1}$ with linear correlation $R^2$ of 0.9968.

**4.3.3.1 In-Vivo Human Forearm.** The polarization imaging measurement technique has been tested on human skin in-vivo. In this measurement, a special support for the right forearm is utilized. The experimental set up for holding the forearm is shown in Figure 4.18.

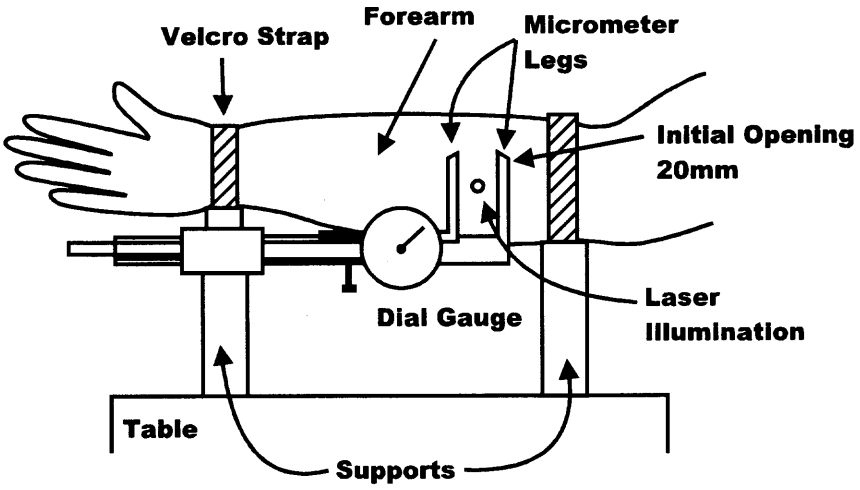


**Figure 4.18** 1-D forearm vernier caliper stretcher mounts.

The forearm is supported with two plastic supports. One is located under the wrist and the other one is under the elbow. The arm is secured on these supports with Velcro straps. A micrometer is secured on one of the supports. The two legs of the micrometer are placed against the skin at the anterior side of the forearm. Two legs of the micrometer are attached to the skin of the forearm with a double-sided scotch tape with an initial 20mm opening. Intensities of parallel and perpendicular polarized light of the analyzer were measured. The differences of the reflected light intensities were plotted against the stretch relative to the initial length of 20 mm. Skin was stretched with the micrometer by moving one leg relative to the other. The initial measurement, the forearm skin is stretched manually. After each additional stretch, the moving leg was locked with its own setscrew before the optical measurement. Data is recorded for stretch along and perpendicular to the long axis of the forearm. The stretch of forearm skin experiment is repeated with HeNe laser. Nine different subjects participated. Some of the measurements were taken on different days while some measurements are on the same

day. A total of six measurements are taken by Argon-Ion laser and four measurements are taken by Helium-Neon laser. All measurements were taken under the same in-door environmental conditions with about the same humidity and time of the day where measurements were taken for different days for consistency. The subject's forearm was all prepared according to the discussion in chapter 3.3.6. Results obtained for in-vivo human skin (two adult males) for the anterior side of right forearm by using an Argon-Ion laser are as shown in Figure 4.19.

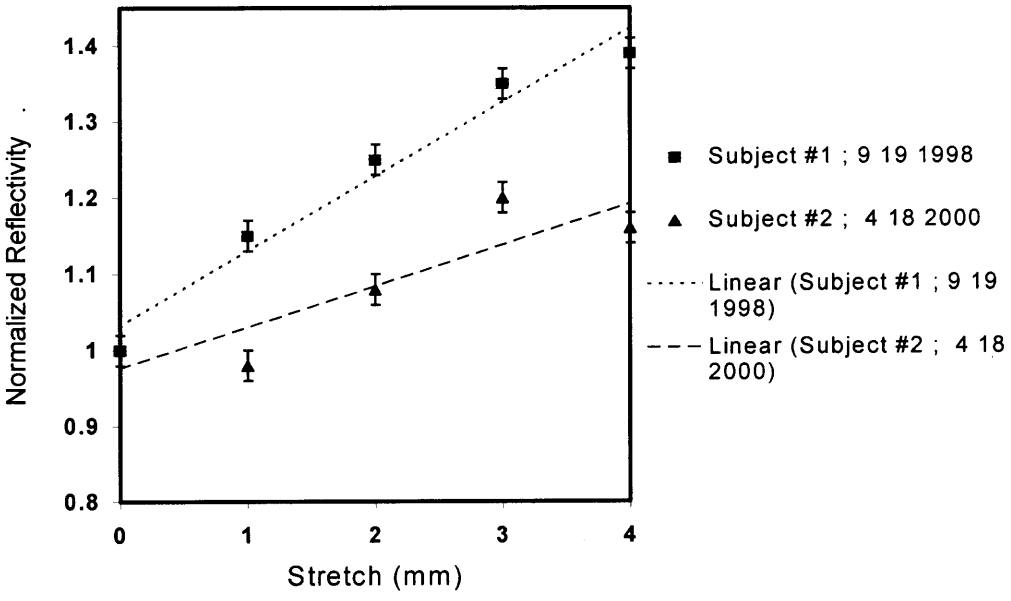


**Figure 4.19** Stretch versus reflected light intensity for in-vivo human skin (Subject 1 & 2, adult male ) for the anterior side of right forearm.
(Blue light $\lambda = 488$ nm)

The net reflected intensity is plotted against the additional stretch relative to the initial un-stretched tissue (20mm), which is the elongation of the distance from the original 20mm opening. The Figure 4.19 shows a good correlation between the stretch and reflectivity for subject 1 and 2 for stretch along the long axis of the forearm.

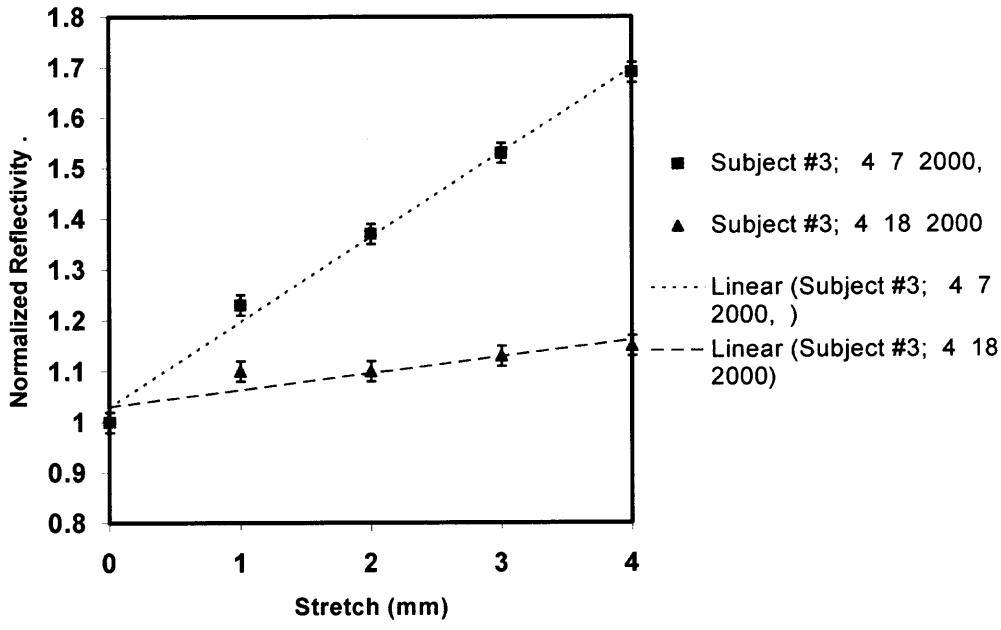


**Figure 4.20** Human forearm measurement for subject 3 (Adult male). Measurements were taken in two different days.

(Blue light $\lambda = 488$ nm)

Next, Figure 4.20 shows right forearm measurement for the subject 3 for two different days. Figure 4.21 shows the results of subject 4's for same day, with two measurements with an Argon-Ion laser. Similar experiments were ran by substituting with a Helium-Neon laser results are summarized in Figure 4.22 and Figure 4.23.

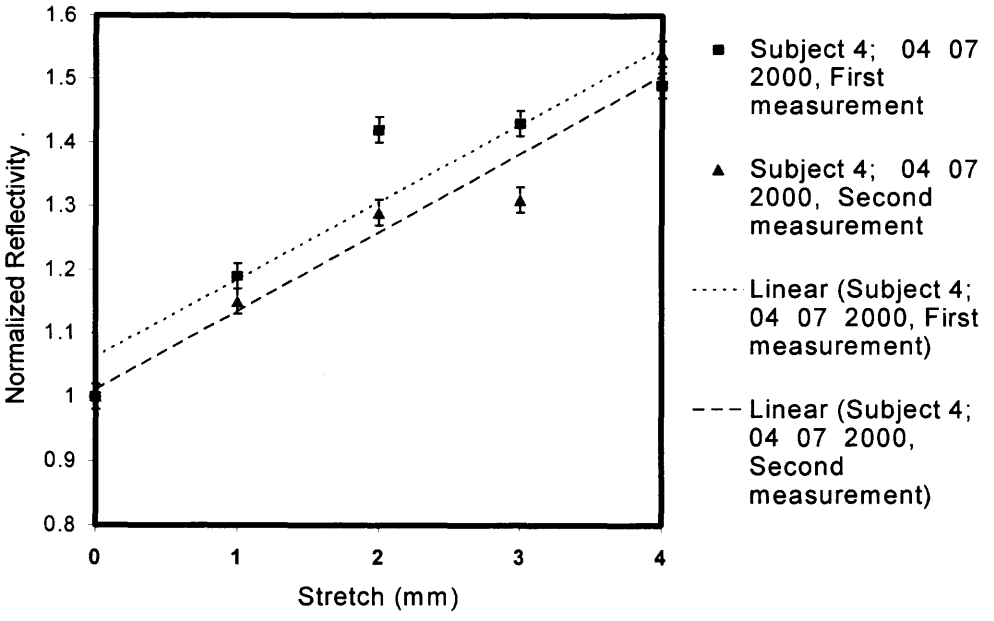


**Figure 4.21** Human forearm measurements for subject 4 (Adult male). Both measurements are taken in the same day with two hours apart.

(Blue light $\lambda = 488$ nm)

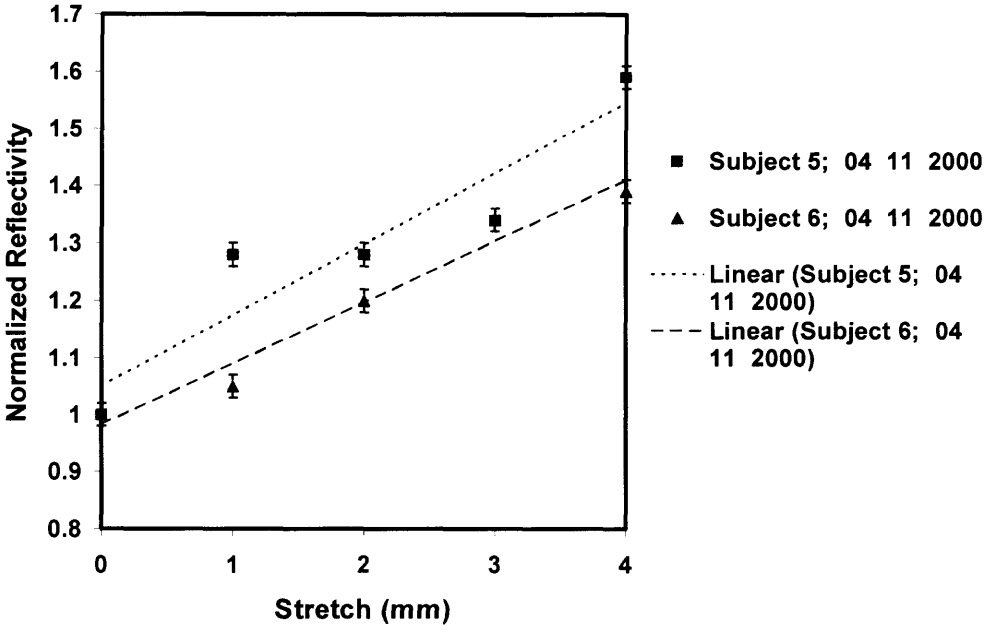


**Figure 4.22** Human forearm measurements for subjects 5 and 6 (male adults)with Helium-Neon laser.

(Red light $\lambda = 632.8$ nm)

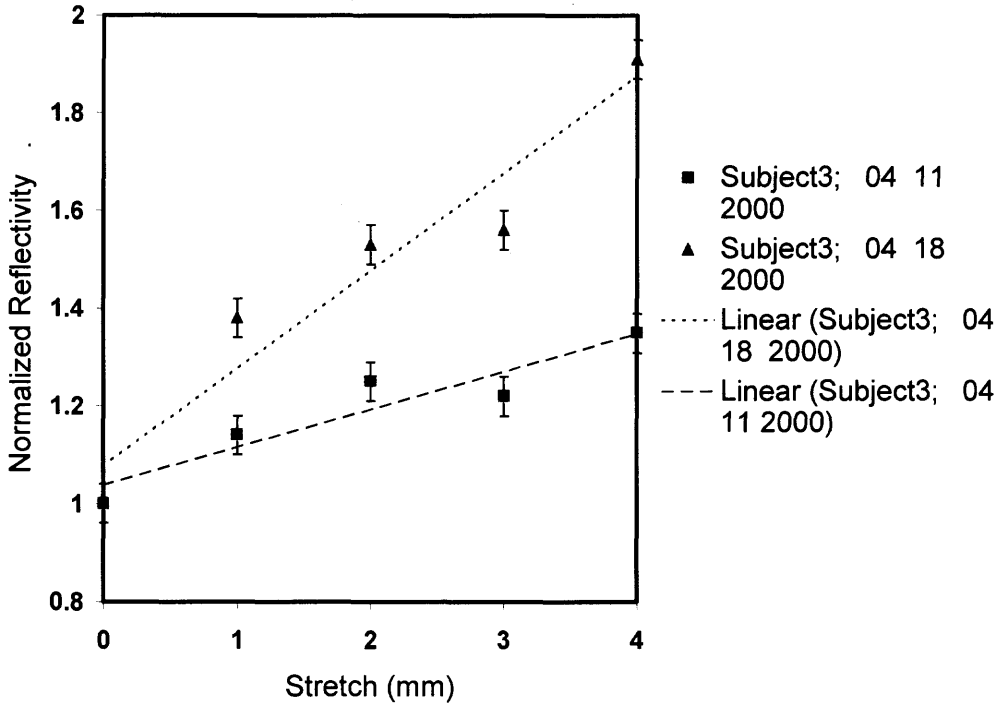


**Figure 4.23** Human forearm measurement for subject 3 with Helium-Neon laser in two different days.

(Red light $\lambda = 632.8$ nm)

Figure 4.22 shows the forearm measurement of subject 5 and 6. Human forearm measurements of subject 3 in two different days with Helium-Neon laser are summarized in Figure 4.23. The reproducibility of the results was investigated and will be shown later in the automated in-vivo testing section. Figure 4.24 shows the results for applied stretch and compression for (shortening of the distance from the original 20mm opening) subject 1 by using an Argon-Ion laser. Stretch and shortening are along the long axis of the forearm. The jump in the reflected light intensity at the initial length (20mm opening) is due to viscoelastic deformation sets in, at the initial stretch measurement. Reflectivity measurements with skin stretch perpendicular to the long axis of the arm were performed

with the Argon-Ion Laser set up. Figure 4.25 shows the resulting reflectivity for skin stretch parallel and perpendicular to long axis of fore arm for subject number 3.

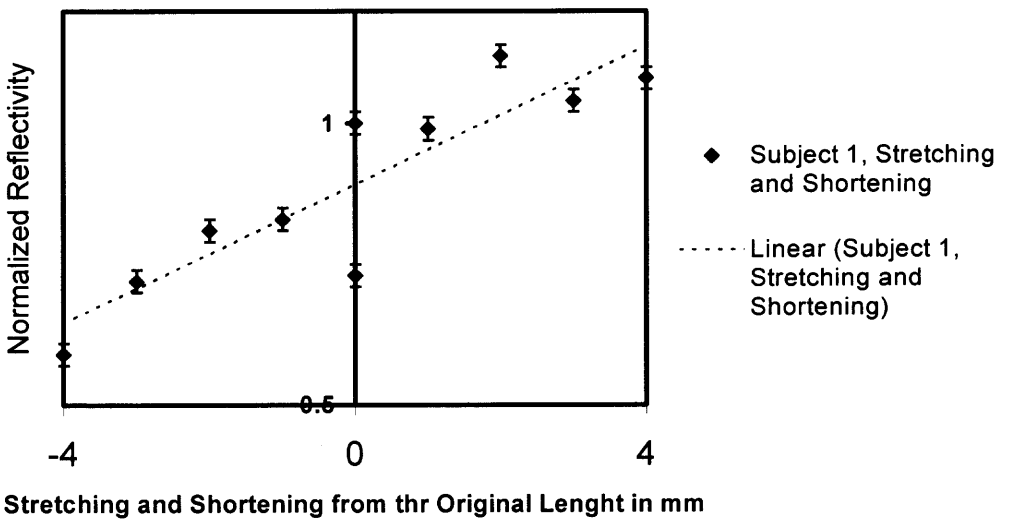


**Figure 4.24** Stretch from the initial opening of 20mm and then shortening from the initial opening for human skin (Subject 1) in-vivo.

(Blue light $\lambda = 488$ nm)

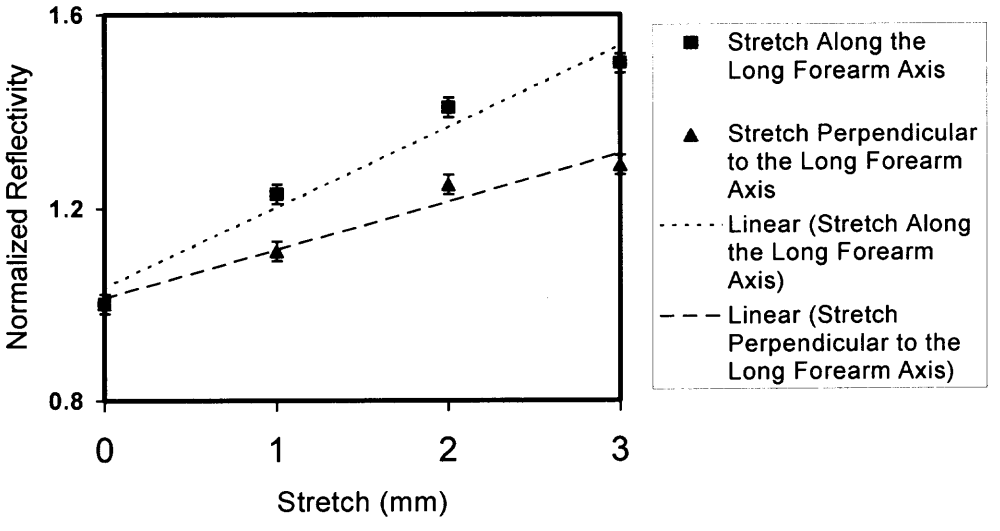


**Figure 4.25** Reflected light intensity vs. stretch for in-vivo human skin (Subject 2, adult male) for the anterior side of the right arm. Stretches are parallel and perpendicular to the long axis of the forearm.

(Blue light $\lambda = 488$ nm)

Due to the limited number of data points acquired by manually stretching human skin, as with the in-vitro measurements, the experiment was automated. Similar results are obtained for in-vivo human skin, utilizing the automated stretcher is as shown in Figure 4.26. With the improved effectiveness of the newly automated stretcher, the reproducibility of the measurement were demonstrated, on the reflectivity versus stretch data recorded on a Human subject on the same bodily location for ten different days. On each day, ten trials were conducted with a consistent interval between successive measurements.

**Table 4.5** Measured slope ($\times 10^{-2}$ $mm^{-1}$) of reflectivity vs. stretch data for a Human Subject on ten different days

| Day/Slope($mm^{-1}$) | Day 1 | Day 2 | Day 3 | Day 4 | Day 5 | Day 6 | Day 7 | Day 8 | Day 9 | Day 10 |
|---|---|---|---|---|---|---|---|---|---|---|
| | 0.018 | 0.02 | 0.012 | 0.02 | 0.018 | 0.013 | 0.017 | 0.02 | 0.015 | 0.017 |
| | 0.017 | 0.016 | 0.017 | 0.021 | 0.015 | 0.017 | 0.023 | 0.019 | 0.017 | 0.018 |
| | 0.019 | 0.016 | 0.016 | 0.017 | 0.015 | 0.017 | 0.021 | 0.018 | 0.02 | 0.017 |
| | 0.017 | 0.02 | 0.019 | 0.022 | 0.013 | 0.019 | 0.016 | 0.018 | 0.013 | 0.019 |
| | 0.02 | 0.016 | 0.015 | 0.02 | 0.015 | 0.019 | 0.023 | 0.02 | 0.019 | 0.017 |
| | 0.019 | 0.016 | 0.02 | 0.013 | 0.015 | 0.016 | 0.018 | 0.018 | 0.019 | 0.02 |
| | 0.02 | 0.019 | 0.017 | 0.022 | 0.018 | 0.017 | 0.019 | 0.013 | 0.02 | 0.018 |
| | 0.02 | 0.017 | 0.02 | 0.022 | 0.019 | 0.02 | 0.017 | 0.017 | 0.017 | 0.02 |
| | 0.016 | 0.019 | 0.023 | 0.017 | 0.022 | 0.019 | 0.017 | 0.02 | 0.019 | 0.017 |
| | 0.016 | 0.02 | 0.019 | 0.015 | 0.02 | 0.019 | 0.016 | 0.019 | 0.02 | 0.016 |
| **Average** | 0.0182 | 0.0179 | 0.0178 | 0.0189 | 0.017 | 0.0176 | 0.0187 | 0.0182 | 0.0179 | 0.0179 |
| | 1.82±.0.16 | 1.79±0.18 | 1.78±0.31 | 1.89±0.32 | 1.70±0.28 | 1.76±0.21 | 1.87±0.27 | 1.82±0.21 | 1.79±0.24 | 1.79±0.14 |

The data observed is tabulated in Table 4.5. On a day-to-day basis, the data is reproducible to roughly 13%. The error is determined by the standard deviation of the ten measurements.

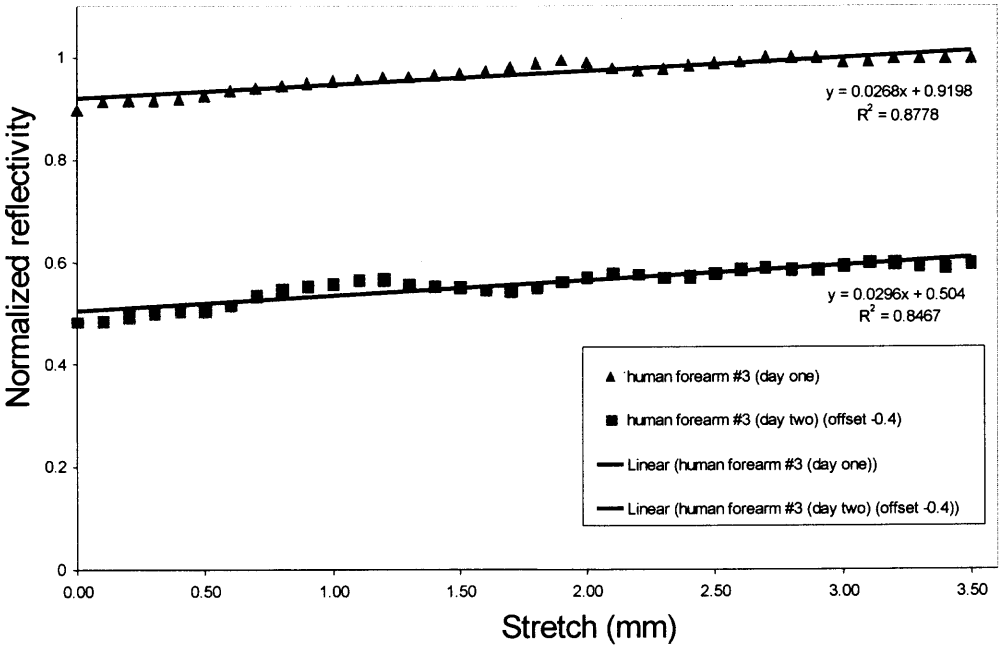


**Figure 4.26** Normalized reflectivity vs. stretch for in-vivo human skin.

With the establishment of a consistency in the measurement of the reflectivity versus stretch to within 13%, different parts of the body where tested to see if known difference in the mechanical properties of skin could be measured. For instance, automated measurements of reflectivity on in-vivo human forearm with stretch applied parallel and perpendicular, to the forearm long axis, once again shows consistent results and are tabulated in Table 4.6 below for assessment. Physiologically the skin is easier to be stretched parallel to the long axis of the forearm compared to the perpendicular direction of the axis.

**Table 4.6** Measured slope of reflectivity versus stretch data for stretch applied parallel to long axis of the arm compared to stretch applied perpendicular to the long axis of the arm

| Direction of Stretch | Slope ($mm^{-1}$) |
|---|---|
| Parallel to Long Axis of Arm | 0.0164 |
| Perpendicular to Long Axis | 0.0114 |

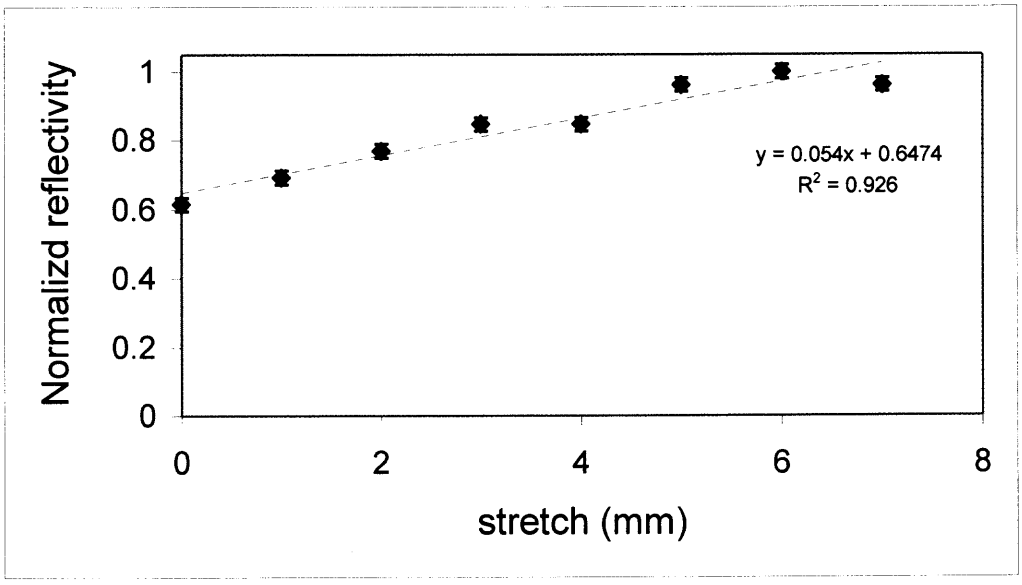


**Figure 4.27** Human abdomen parallel to the Langer lines reflectivity data.
(red light $\lambda$=632.8 nm)

The PIET and the data analysis are also employed to investigate the reflectivity of other in-vivo human sample/location. They included the human abdomen; back skins that are aligned parallel to the human spine, with both parallel and perpendicular stretching direction. Typical results obtained for the abdomen skin is as shown in Figure 4.27 above. In all cases, the total reflected light intensity was found to be directly proportional to the amount of stretch applied, and can be inferred to the surface roughness changes. However, as seen in the parallel and perpendicular directional applied stretch on the

forearm experimentation described before, the slope of the reflectivity is slightly higher for more easier stretched skin (mechanical properties). In the case of abdominal reflectivity slopes of typically $0.054 \pm 0.005$ $mm^{-1}$ from Figure 4.27, it was found that it was at least half the slope for the reflectivity slope, $0.168 \pm 0.015$ $mm^{-1}$ of human forearm parallel stretching along the long axis of the arm.

Typical data for various human skin type and skin location of the normalized reflectivity versus stretch performed are as tabulated in Table 4.7.

**Table 4.7** Normalized reflectivity vs. stretch slopes for different type of skin location

| Skin Type | Normalized reflectivity vs. stretch slope ($mm^{-1}$) | Linear correlation coefficient ($R^2$) |
|---|---|---|
| Artificial skin | 0.0404 | 0.9908 |
| Human Forearm (parallel) | 0.0164 | 0.9877 |
| Human Forearm (perpendicular) | 0.0114 | 0.8426 |
| Human Abdomen (parallel) | 0.0540 | 0.9260 |
| Human Abdomen (perpend.) | 0.0334 | 0.7869 |
| Human Back (parallel) | 0.0115 | 0.8908 |
| Human Back (perpend.) | 0.0077 | 0.7869 |
| Pigskin Shoulder (parallel) | 0.0303 | 0.9968 |
| Pigskin Shoulder (perpend.) | 0.0001 | 0.9821 |

It can be inferred that when the applied stretch is along the Langer lines, the reflectivity slopes is higher compare to the perpendicular direction. Langer lines are defined as the lines of tension of the skin. The general course of the connective tissue bundles of the corium determines the direction of these linear clefts, or Langer lines. It is found that whenever possible, incisions should be made along or follow these lines, since

there will then be little gaping of the wound and a subsequent finer scar. The typical human Langer lines profile is as illustrated in Figure 4.28. The measurement on the human abdominal and back skin are performed exactly 3.5" horizontally away from the human spinal bone (symmetrical axis) for the anterior and navel for the posterior side. By this configuration, the experimental sample would have the Langer lines alignment and/or distribution approximately the same as on the human forearm experiment as shown in Figure 4.28.

In order to prove the PIET method works over all the possible human natural skin pigmentation or genetic ethnicities, a small study group of human volunteers was established. The group assembled consisted of almost all possible skin complexions in the middle age group, i.e. 29 – 40 years old. As a controlled study, all the participants were asked to have the dietary and skin management/treatment throughout the experimentation period, which was for three days in a row, with several test runs each day as before. Furthermore, the experiments were conducted at the approximately same time of the day with the similar procedure applied as described in the subchapter of in-vivo specimen preparation.

All the participants' reflectivity intensities were linear and proportional to applied stretch as shown in all the previous plot of results and will not be plotted here for space conservation. The results observed and measured are encouraging and help in establishing the PIET method to a broader audience. The results of the group study are as tabulated in the following Table 4.8. The standard deviation of the data and its corresponding linear correlation coefficients were also calculated and shown in the same table.

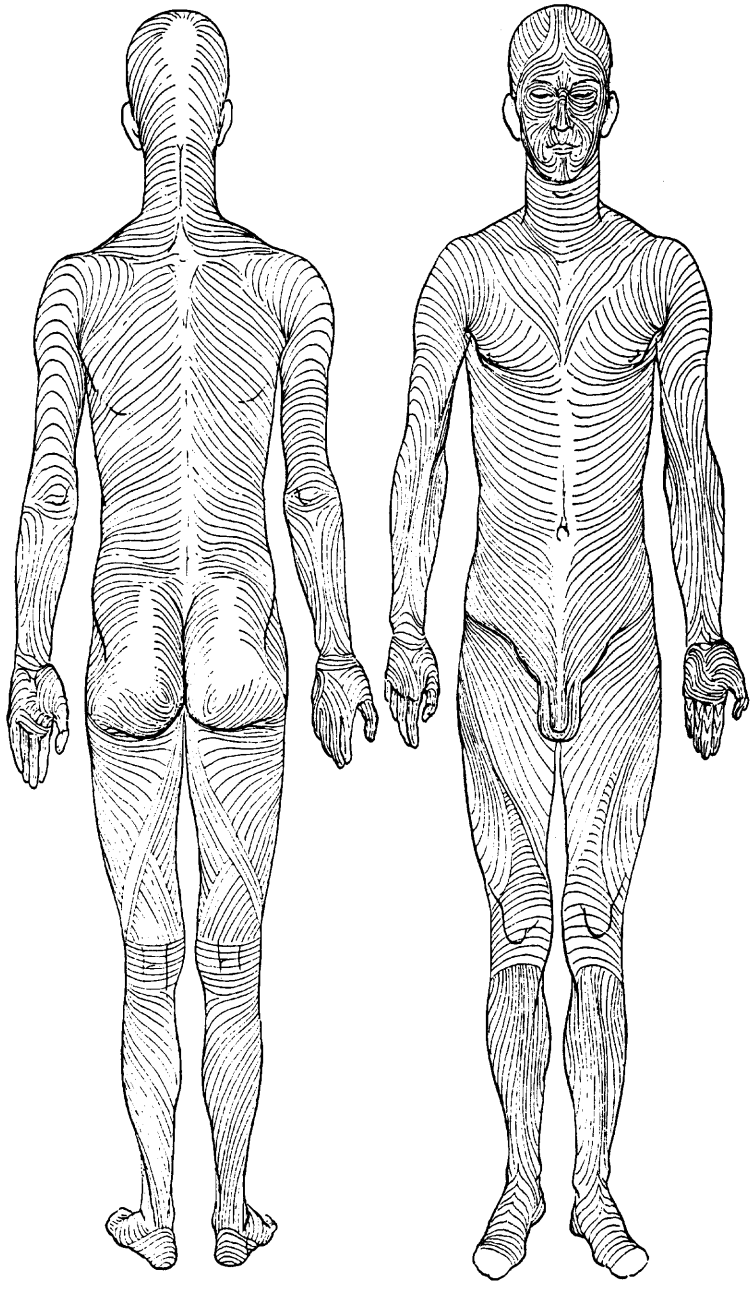

**Figure 4.28** Human Langer lines distribution (adapted from Surgical Anatomy)[69].

**Table 4.8** Measured slope of reflectivity versus stretch, with its corresponding $R^2$ and $\sigma$ data for nine different skin complexions forearm stretch applied parallel to the long axis of the arm

| Subject # | Skin Complexion | Average Normalized Reflectivity vs. stretch gradient(mm^-1) | Linear Correlation Coefficient | Average Standard Deviation (±) |
|---|---|---|---|---|
| 1 | Fair-white | 0.06100 | 0.98700 | 0.001542323 |
| 2 | Yellow | 0.02660 | 0.99460 | 0.000375982 |
| 3 | Yellow | 0.02680 | 0.87780 | 0.002038673 |
| 4 | Extreme white | 0.01301 | 0.92368 | 2.56865E-13 |
| 5 | Fair | 0.03380 | 0.93604 | 0.001468991 |
| 6 | Medium brown | 0.01540 | 0.93970 | 7.31774E-06 |
| 7 | Black | 0.05620 | 0.95887 | 0.001222333 |
| 8 | Light brown | 0.04800 | 0.94131 | 0.002434763 |
| 9 | Dark brown | 0.06840 | 0.92500 | 0.002275607 |

**4.3.3.3 In-Vitro Pigskin Burnt Data.** The in-vitro pigskin samples were subjected to thermal burns, following the standard skin burn procedure practiced in burn studies, which uses a block of brass measured 4" by 4" by 2" heated in 100 degrees Celsius boiling water.[70] Thus, the block will have the same amount of heat applied in a specified amount of burn time, as they have the same specific heat capacities. Since intact skin will not deform as much as the skin samples excised from the animal's body, the skin size was identified and marked on the animal with a template before they are excised so that in the experimental apparatus they can be stretched to original size before new tension is applied. The duration of the thermal exposure of the heated brass block

correlates well with the histologic evaluations, which confirm the depth of the created injury. Exposures of 0.0, 10.0, and 20.0 seconds create necrosis to depths of 0.0, 1.1 and 1.6 mm, respectively.[71] Two different wavelengths of HeNe laser source were used in these PIET experiments; they are namely, 632.8 nm and 547 nm. They both show similar reflectivity results for the same type of specimen used.

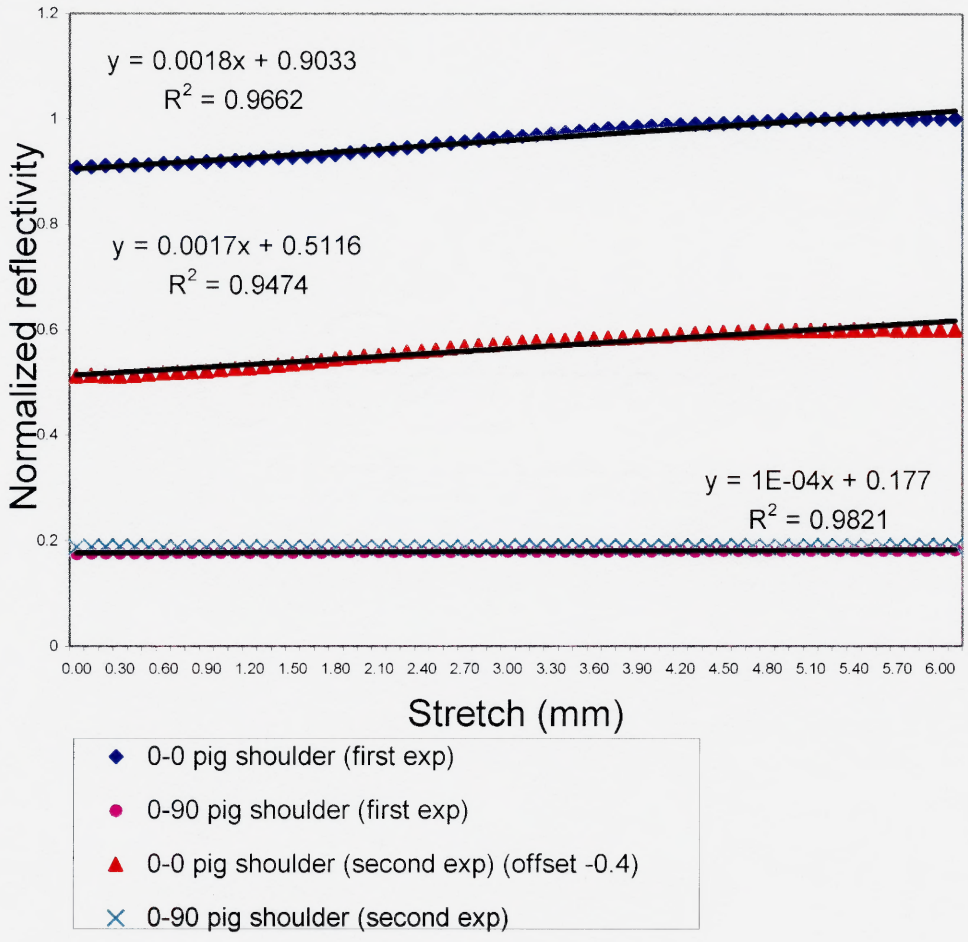


**Figure 4.29** Measured reflectivity vs. stretch data of in-vitro pigskin from animals' shoulder portion for 0.0 sec burn duration. Both the 0-0 and 0-90 degrees polarization is shown for the 2 different trials.

It is worthwhile to notice the linear trend between the reflectivity intensities plotted against the applied stretch in Figure 4.29 were as observed by the PIET in the

previous biological specimen experiments subchapter. Also worth allusions are the invariant (flat d.c offset) 0-90 degree polarization reflectivity results of the pigskin. Hence, the experimental results or slopes of the reflectivity versus stretch measurements is the same as the 0-0 degree polarization slope, because the cross polarizers data subtraction procedure would only reduces/change the y-axis intercept values, which is a constant, and not the trends of the reflectivity increment due to stretches. Since it is impossible to perform the burn experiment on in-vivo human skin, pigskin is chosen because of its similarity in biomechanical and physiological properties to human skin.

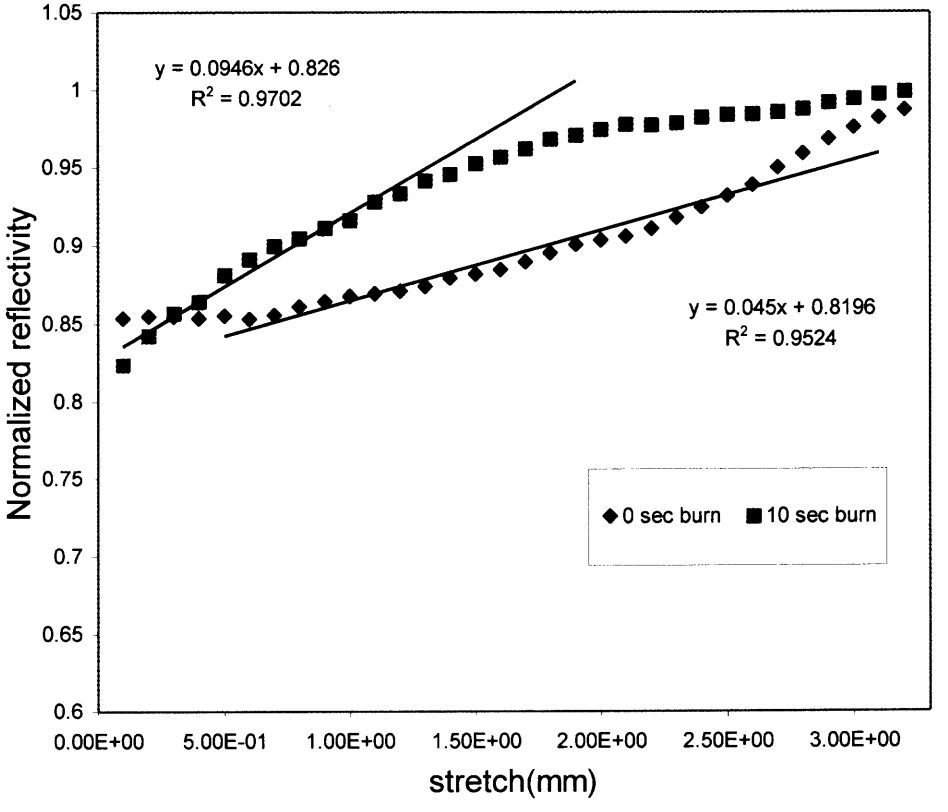


**Figure 4.30** Reflectivity results of unburnt and burnt in-vitro pig's shoulder skin.

A typical noticeable reflectivity increment in results between the unburnt; 0.0 second and burnt; 10.0 second of the in-vitro experiment is shown in Figure 4.30. These reflectivity incremental trends continued until a certain limit, where additional burnt duration yields negative or close to zeroes slopes. PIET experimental result of different burnt duration of pigskin taken from the same parts of the animal sides that is parallel to spine is as shown in Figure 4.31 and Figure 4.32 below.

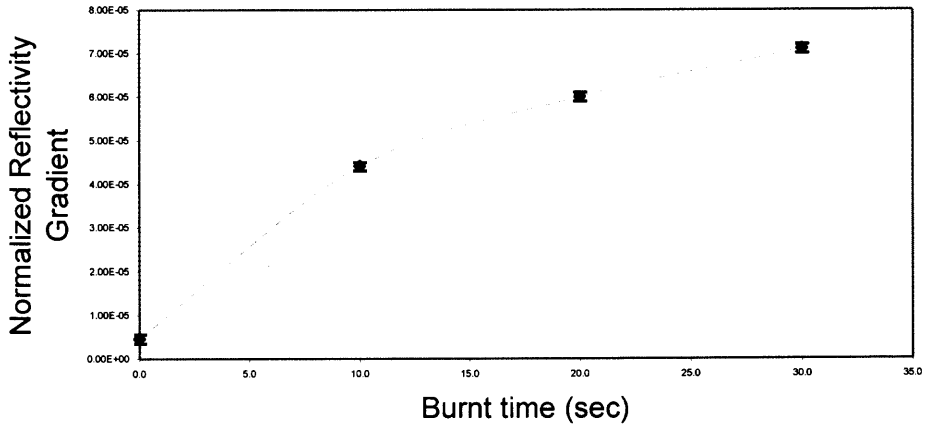


**Figure 4.31** In-vitro pigskin burnt data reflectivity slope($mm^{-1}$) as a function of scorch time.

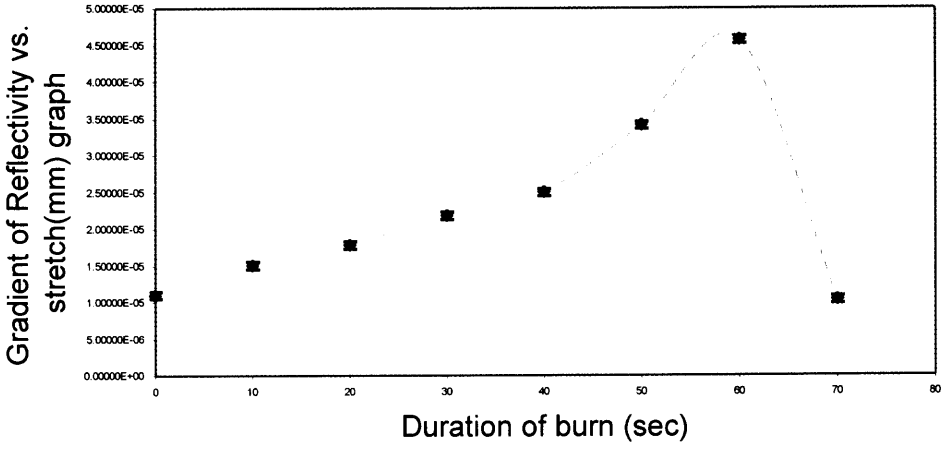


**Figure 4.32** In-vitro pigskin burnt data of normalized reflectivity vs. stretch(mm) gradient ($mm^{-1}$) vs. burnt time.

# Chapter 5

# DISCUSSION

## 5.1 Implementation

The 2-D Polarization Imaging Elastometry Technique uses changes in the diffuse-reflectance properties of skin that are due to mechanical deformation to determine soft-tissue deformations noninvasively. A small spot size, or gauge length, with a miniaturized detector and a fiber-optic delivery– detection system would allow surgeons to determine the stretch of soft tissues in real time. One could improve the utility of the technique by imaging stretch patterns from a large area of tissue. The technique can easily be extended to an imaging technology by the replacement of the single-element photodetector with a CCD camera. The geometry of the imaging optics is similar to the 2-D polarization imaging technique.[3] Experiments that image a nonuniform stretch pattern by use of our technique are underway and will be reported elsewhere. Measuring the tension in wound closures,[72] skin flaps,[73] and tissue expanders[74] will help surgeons to treat wound closure and healing in patients more successfully by minimization of scar tissue and maximization of the speed of treatment, especially after accidents and burns, from knowledge of how much the skin can be stretched at each treatment step.

The information will be very useful, in particular, in plastic surgery because the effects of tension forces on the successful outcome of surgery are crucial. The measurement technique can be used to determine the excess mechanical deformations of internal vessel walls or internal organs around a surgical site. This information could be useful in avoiding injury to the surrounding tissue, as the optimum amount of force could

be applied during suturing. By use of a CCD imaging technique, the stretch sensor could give instant information on the stress concentration of tissues that is due to different surgical procedures. Further applications could be found in mechanical experiments to determine the deformation of the diffuse-reflectance materials as a non-contact extensometer. With a very small spot size, (gauge length) the technique could be superior to the existing technology of video extensometers. Determining the mechanical properties of soft tissues and also obtaining the mechanical properties of soft artificial biomaterials will advance the fields of biomechanics and biomaterials in which real-time, *in-situ* imaging measurements of such properties are critical.

It was observed that the difference in light intensity between the two perpendicular polarization measurements of the analyzer is related to the amount of stretch in the skin. This result suggests that changes in skin stretch properties in an area of interest can be monitored and estimated non-invasively by comparing the reflectivity changes that take place in symmetrical anatomical locations by applying controlled deformations and monitoring the resulting changes that take place in the light reflection properties of the skin. In addition, during the applied deformations due to medical interventions, one can follow continuously the changes that take place in the light reflection properties of the area under investigation.

The measurement techniques, which provide information to the surgeons about the excess mechanical deformations of soft tissue around the surgical site during the surgery, would avoid injury to the surrounding tissue since the optimum amount of force could be applied during suturing.

## 5.2 Soft Tissue Reflectivity - Spatial Resolution

### 5.2.1 Comparison of PD, CCD Detection and Source Measurements

In comparing reflectivity results using the same source, detector and optical configuration, the measured reflectivity as a function of stretch is reproducible from run to run and from sample to sample. Typically, the slopes of the measured reflected light intensity versus stretch curves are the same to within less than 1% for the single element detector measurements. In order to quantitatively compare (e.g. absolute reflectivity, slope) the reflectivity versus stretch results of the single element photodetector and CCD camera, an absolute calibration is required for the reflectivity. Even if the same light source is used, differences in the efficiency of collected light (e.g. field of view, variations in optical losses of optical components, etc.) lead to slight variations in the detected power. Consequently, the slope of the detected power versus stretch curves is different depending on the choice of detector and optical arrangement. If the results from different sources are compared [e.g. He-Ne and LED] with the same detector, the slopes of the detected power versus stretch will not be the same due to the different spatial distribution of optical power of the sources. In conclusion, although absolute reflectivity and slope results for a particular detector/source are reproducible, differences in the efficiency of light detection for difference detectors leads to a different slope depending on detector and source combination. In analyzing the data, rather than attempting to account for variations in the field of view, optical components, detector efficiency, etc. to directly calibrate the absolute reflectivity, emphasis is on the existence of linear behavior, spatial resolution, and stretch resolution.

### 5.2.2 Spatial Resolution

The spatial resolution of the 2-D imaging technique is determined by three effects: (a) the spatial scale over which Mie Scattering by the tissue is valid (b) the area of tissue which is imaged onto one camera pixel or the single element photodetector, and (c) the coherence length of the light source (laser speckle). When the wavelength of light is shorter than or comparable to the spatial extent of a scattering center, the propagation of light in the tissue is well described by (Mie Scattering).[55,75] As described in earlier work,[2] as long as the height and spatial extent of interface roughness is larger than the wavelength of light, the scattering of light from a rough interface (which plays the role of scattering centers) is in the Mie scattering limit. In this limit the angular and intensity dependence of the reflectivity is derived from the geometry of the interface assuming that light is specularly reflected from each tilted element of the interface.

Using the hypothesis that the changes in reflectivity during stretch are due to the smoothing of the rough interfaces, one limit to the spatial resolution is the spatial scale over which the interface roughness is measured. For a single element photodetector measurement, the spot size of the laser beam defines the area over which the surface reflectivity is averaged. This corresponds to the gauge length of the VDA/VMA measurement systems or equivalently the spatial resolution of the measured tissue stretch. In this situation, one is measuring the average reflectivity of the illuminated tissue area corresponding to an average tissue interface roughness. For the CCD imaging measurement, the corresponding parameter is the area of skin that is included in the summing process. By decreasing the spot size of the laser, equivalently, one is sampling a smaller area of tissue. In the limit that the spot size of the laser is on the same order or

smaller than the scale length of the surface roughness, the simple relationship - based on Mie scattering - that the change is reflectivity is linear with the stretch may no longer be true. This may limit the spatial resolution of the 2-D polarization imaging technique.

Based on the point measurements of Figure 4.8, the spatial resolution for measuring the stretch of the PVC rubber is roughly 200μm. For spot sizes below this value, the reflectivity data is poorly fit by a straight line. The corresponding spatial resolution as determined by imaging is 120-234μm. While the spatial resolution results of the single element detector and CCD camera are consistent, the CCD images, as shown by comparing the ranges of slopes from Table 4.3 and Table 4.4, show a larger variation than for the single element detector. This may be due to differences in the way the data is averaged for the two techniques: The single element detector data is acquired using phase sensitive detection techniques with a chopping frequency of about 1kHz and an integration time of 1sec (1Hz). The 1KHz/1Hz bandwidth ratio corresponds is equivalent to more data averaging than the CCD data since the raw CCD image data is the sum of only two images. The superior data averaging capabilities of phase sensitive detection leads to smaller fluctuations in the detected reflectivity signal with stretch. Other potential sources of error include fluctuations in the laser power, effects of a non-symmetrical gaussian profile of the HeNe laser beam, speckle due to surface roughness and dark background pixel contributions when averaging[57,76,77] The total error of the 3-D imaging techniques depends on the imaging and optical system properties and mathematical roundup errors in matrices computation.[78]

### 5.2.3 Stretch Resolution

For a spot size of about 1.1mm, as discussed above, the stretch resolution is roughly 0.32%. This value cannot be directly compared with the 0.13% strain resolution (0.8mm gauge length) recorded for video techniques[10] since stretch and strain are not equivalent parameters. (One would need to know the stretch corresponding to a known applied force in order to deduce the correct relation.) However, in the simple limit of an elastic material such that the stretch is proportional to the strain, the stretch and strain resolution should be comparable. For this approximation, the stretch resolution of the 2-D polarization imaging technique is about a factor of two larger than video techniques for comparable spatial resolution. The stretch resolution using CCD imaging is worse than the single element detector method due to limited averaging (2 pictures) of the CCD imaging data compared to phase sensitive detector. To check this, numerous images at the same stretching condition were acquired. When more and more of these images are averaged together to generate a single image for the stretch position, the scatter in the data points around the linear regression line becomes smaller. Therefore, in order to achieve smaller errors in the reflectivity data extracted from CCD image, a larger number of images should be averaged. As will be discussed below, the averaging of the several images reduces the impact of laser speckle to some extent. With improved averaging and the removal of laser speckle via an incoherent light source, we suspect that the stretch resolution of the 2-D polarization imaging technique can be reduced well below the limit set by video techniques (0.14%).

### 5.2.4 The Influence of Laser Speckle

Within the proposed model of interface roughness[2], the scattering of light from the surface roughness can be treated as Mie scattering where light is reflected from each tilted element of an interface. In calculating the reflectivity, it is assumed that the light rays, which reflect from the different tilted elements of the interface, do not interfere with each other. This is strictly true if the illuminating light source is incoherent. For a coherent light source (e.g. a laser), it is possible to observe interference between the various light rays scattering from the different surface bumps. This leads to the well-known speckle effect.[76] For large (~1mm) laser spot sizes, interference among the various rays of light reflecting from the surface (laser speckle) can be ignored. This approximation is valid due to the long integration time for data acquisition using phase-sensitive detection (1 sec time constant) and the large area of illuminated tissue. The one second integration time is much longer that the correlation time of laser induced speckles so that temporally, the speckle effect is averaged out.[62] In addition, for large spot sizes, the detected light contains many uncorrelated speckles arising from different locations on the sample surface. When all of the collected light is detected by a single element photodiode, any spatial fluctuations in light intensity due to laser speckle are averaged out.

As the spot size of the laser is decreased, or equivalently, if the area of pixels averaged is decreased, the detected light intensity may be modulated by the speckle effect. If a CCD camera is used for light detection, and if the size of imaged area is small enough, laser speckle may effect the measured intensity of the pixels. In other words, the intensity fluctuations due to individual speckles would be resolvable with the camera. By

summing an area of pixels, as is done to generate the data of Figure 4.10-10 and Figure 4.15, the effect of speckle, to some extent, can be averaged out. However, as the spatial resolution is further reduced, the effect of laser speckle cannot be spatially averaged out. Moreover, since the fixed shutter speed of the camera is comparable to the correlation time of speckle, averaging only two images does not effectively average out the temporal intensity variations due to speckle. If the effects of laser speckle become too large, then the simple linear relationship between stretch and reflectivity is no longer correct. As shown in both the photodetector and CCD data, laser speckle is the cause of the nonlinear behavior with stretch that limits the spatial and stretch resolution of the technique to about 200μm with a coherent source.

With an incoherent LED source, laser speckle is eliminated resulting in an improved spatial resolution limit of about 24μm. This resolution limit represents about an order of magnitude improvement in spatial resolution compared to 2-D polarization imaging using coherent laser sources and almost two orders of magnitude improvement in spatial resolution over state-of-the-art video imaging techniques. The improvement in spatial resolution over existing state-of-the-art techniques may permit in-situ, non-invasive biomechanical measurements on various biological and artificial soft-tissues with unparalleled resolution.

## 5.3 In-Vivo Human Forearm

If one were to measure the absolute reflectivity of skin, the absolute reflectivity would depend on many factors such as age, water content, pigmentation, etc. However, in the experiments, the main concern is the slope of the reflectivity measurements curves (e.g.

the relative *change* in reflectivity vs. *change* in stretch). For such a measurement, the *absolute* reflectivity does not matter - only relative changes in slope matter.

In-vivo human experiments on skin show that the reflection properties of skin change with stretch for both wavelengths ($\lambda$= 488nm and $\lambda$=632.8nm). Added linear regression lines show that the intensity of the reflected specular light after subtracting the noise increases with applied stretch as in Figure 4.19 to Figure 4.23. The slopes of the regression lines are different for different subjects; it is also varies for the same subject for different days with manual experimentation. Such differences are to be expected since the mechanical properties of tissue will vary with age, moisture content, and error in taking the data manually. Figure 4.21 indicates that the variation in slopes for the same subject in the same day could be rather small if one leaves enough time between the measurements for skin to recover its viscoelastic deformations. With the automated stretcher, the observed results, as in Table 4.5 for the same subject on different days were very reproducible, with about 13% of standard deviations.

The Figure 4.24 shows that even a full cycle after two tries (Zero -stretch-zero and shortening) of the skin yields correlation between the changes in distance versus reflected light intensity. The jump at the origin is due to viscoelastic deformation of the skin during the stretch cycle[79]. The scattering in the data obtained in Figure 4.24 as compare to Figure 4.19 for subject #1 was due to short time resting period between the measurements of the initial cycles. The longer time intervals given between the cycles reduce the effect of viscoelastic deformations and smoothes out the data, as shown in Figure 4.21.

The stretches in two perpendicular directions yield good correlation between stretch and reflected light intensity and also it shows that skin has anisotropic properties, in Figure 4.25 which can be detected by light reflection. Similar stretch experiments on the volar surface of the forearm by other researchers showed that the mechanical properties of the forearm skin are anisotropic.[65,80] Also, in that study it was shown that skin impressions that are taken by silicone rubber[81] changed with applied stretch. If the skin surface is approximated by a sinusoidal curve in the resting stage, stretching reduces its amplitude and increases its spatial scale thereby making it smoother and flatter resulting in a commensurate change in reflective characteristics of the skin.[2,65] As the skin is stretched towards its maximum limit, one would expect the reflectivity to saturate with increasing stretch since its surface becomes mirror-like. Continued stretching will no longer increase the reflectivity at an appreciable level as compared to lower stress levels, since the surface is already as smooth as possible. This saturation is observed in latex membrane measurements.[2] The change in reflected light intensity is decreasing for larger stretches as evidenced by the reduction in the slope of the curve towards the maximum stretch of 3mm stretch (15%) for subject number 3 in Figure 4.25 perpendicular to long arm axis as compare to parallel to the long arm axis. Similarly, this saturation behavior is observed by Ferguson and Barbenel[65] in their skin tension experiment in which skin behaved rather mechanically stiff in the direction perpendicular to the long axis of fore arm as compare to parallel to long axis of fore arm.

Both wavelengths used in this study gave similar results indicating that the applied stretch changes the reflective properties through out the optical penetration depths of the two wavelengths. It is well known that different wavelengths of light

penetrate different depths into skin tissue. Previous results with wavelength dependent polarization imaging show that features below the surface of the skin can be imaged.[3] For a single wavelength, polarization imaging averages over the penetration depth of the light. The imaging of structures at different depths can be achieved by subtracting the normalized polarized reflectivity images acquired with two different wavelengths (i.e. two different penetration depths). The subtraction will cancel out the image arising from the outer part of the tissue (shorter wavelength image) because the number of photons contributing to this part of the reflectivity is approximately the same for both wavelength images. Therefore, subtracting the two images for different wavelengths produces an image that only contains information from a location in the tissue given by the difference of the penetration depths. This suggests that by using different wavelength light sources PIET can map the stretch field of the skin as a function of depth under applied stretch/force.

In-vivo mechanical measurements of the skin yield comparatively important information to the physicians. Due to certain sicknesses the mechanical properties of the skin change, and certain devices that are available today in the market can determine these properties.[82,83] The suction base devices ( Cutometer SEM 474; SEM 575 and Dermaflex A)[83,84] have become an important tool for determining the mechanical properties of skin in-vivo.[85,86] These devices use a cylindrical orifice to apply a small amount of suction to the skin surface. The small amount of vacuum generated in the cylinder raises the skin inside the cylindrical tube and the displacement of the spherical skin dome under suction can be recorded in time. Using this device, a simple mechanical model is developed to obtain stress-strain curves for skin tissue.[84] This type of

information on the pathological skin can be examined and compared to the information obtained by similar anatomical healthy skin parts (symmetric) of the body. The comparison yields information to the physician concerning the degree to which mechanical changes have taken place in the skin due to pathological changes. In this type of measurement, the anisotropic structure of the skin is averaged out in the cylindrical region under investigation. In addition, the effect of hypodermis on the mechanical properties of the skin cannot be isolated from the results. This type of measurement yields some information about the tension characteristics of the skin. Torsinal devices also can be used to determine the mechanical properties of the skin. They require large measurement sites and must transfer torque to the skin by contact. This type of a device provides information about the torsional properties of the skin and can be utilized similarly to suction tension devices.[82,83] In both cases, the devices must touch the surface of the skin to evaluate the relative mechanical properties as compare to the similar healthy anatomical sites.

The light reflection technique that is introduced in this study potentially allows physicians to apply mechanical deformations/forces outside of the region under investigation. A micrometer or any other type of a device (measuring applied load instead of deformations) can attach the surface of the skin with a double-sided tape. The changes that take place in the reflection of the skin under mechanical deformations/forces can be observed. Comparing the similar anatomical side (symmetric part of the body) one can infer about the physical changes take place in the region due to pathological conditions. As compared to the methods mentioned above, the non-invasive light reflection method, which can take measurements easily under applied mechanical deformations/forces in

two perpendicular directions, provides more information about the mechanical properties of the region under investigation through its sensitivity to the anisotropic properties of the skin.

In this study, attempts have not been made to determine the stress-strain curve of a skin in-vitro but rather point out the potential of the polarized light reflection method. This method can be used alone in-vivo to provide relative information on the changes of the mechanical properties of skin as compare to similar anatomical parts by taking into account the anisotropic structure of the skin non-invasively with high resolution. Moreover, for in-vitro measurements, deformation fields of complicated geometric regions under investigation could be mapped with high resolution under applied mechanical deformations/forces.

## 5.4 In-Vitro Thermally Damaged Pigskin

Most living cells and tissues can tolerate and survive modest temperature or thermal excitation for limited periods of time depending on the species and the metabolic status of the specimen. Recovery after heating is marked by restoration of the normal functions. Most non-lethal thermal injuries of individual cells are secondary either to heat induced acceleration of metabolism or to thermal inactivation of particular enzymes and rupture of the cellular membranes.[55] The best indicators of reversible, non-lethal injury in the living cell or tissues are physiological test that monitor heat sensitive biochemical and metabolic changes rather than morphological alterations. However, certain histopathologic techniques and PIET can be useful to detect mild thermal damage in cells

and tissues, especially those delayed morphologic alterations resulting from disruption of normal functions.

It is found that after several minutes to hours of heating, intracellular and tissue edema and hyperemia occurs. These are easily identified delayed organismal responses to non-lethal thermal damage in both single cell and living tissue. Intracellular edema is due to abnormal accumulation of fluids secondary to thermally induced metabolic dysfunction and resolution of the edema upon repair is the marker of heating. Heat induced tissue edema and transient hyperemia, the increase of blood flow and blood vessel dilatation, is mediated by release of vasoactive polypeptides from local inflammatory cells within several seconds of injury. The actions of the polypeptides causes blood fluids to escape through gaps between the endothelial cells lining the vessel. Alternatively, prolong hyperemia, such as that associated with sunburn, is a delayed response associated with direct endothelial damage. In this case, the histologic indicators of the more severe vascular damage are dilated blood vessels stuffed with red blood cells and, not infrequency, microscopic leakage of the red blood cells through the damaged vessel wall into the adjacent tissue space. Recovery, which is secondary to endothelial regeneration and repair, is seen in a few days.[87]

Cell death and subsequent necrosis result when the damage is so severe that the usual repair mechanisms cannot cope and the mediators of the repair mechanism, such as DNA and RNA transcription enzyme, themselves are thermally destroyed. Again, routine microscopic techniques cannot be used to identify dead cells immediately after heating except in the case of severe damage. However, within minutes of lethal thermal damage, transmission electron microscopy (TEM) reveals accumulation of chromatin, DNA

containing chromosomes, at the margins of the nuclei, which is a recognized TEM marker of cell death, plus more extensive disruption of cellular organelles and limiting cell membranes that are incompatible with survival.[88] After death, cells and tissues undergo nercosis, which is a natural process of disintegration that follows a predictable course over time.

As temperature and heating times are prolonged, cellular and tissues structural proteins, which are more thermally stable than the vital, energy producing enzymes, go through denaturization and conformational changes, a process called thermal coagulation. Coagulations is immediately noticeable and always indicate lethal thermal effect. For most tissue, coagulation can be seen with the naked eye as whitening of the tissue associate with the increased stiffness and opacity. The change of the egg white while being fried is an obvious example of thermal coagulation. On the other hand, coagulation of collagen rich tissues, such as tendon and skin, can be signaled by increasing transparency due apparently to decreased scattering by denatured collagen fibrils.

Microscopically, thermal coagulation of cellular and extracellular structural proteins includes an array of morphological alterations that mark a large range of temperatures and exposure times, as in Table 5.1.

**Table 5.1** Pathologic thermal effect and correlated temperature ranges

| **Thermal damage mechanism** | **Temperature of Onset: Ranges** | **Heating duration** | **Histopathologic effect** |
|---|---|---|---|
| Water dominated processes | 100± | Seconds | Extracellular vacuole formation. Rupture of vacuole, popcorn effect |
| | 100-200 | Seconds to millisecond | Tissue ablation by explosive fragmentation |

In the low temperature ranges, histologic markers of coagulation are more easily detected with TEM but certain subtle alterations in routine prepared, hematoxylin and eosin stained light microscopic sections can suggest thermal structural alteration to the experienced observer. As tissue temperatures and exposure times increase, the coagulation changes become more obvious and PIET analysis could becomes the investigative tools of choice. The most useful histologic markers of coagulation thermal damage in tissues are structural alterations of cell and collagens. Thermally coagulated cells and intracellular organelles shrink and undergo characteristic conformational changes. Collagen area widely dispersed biochemical class of extracellular fibrous proteins that form the supporting scaffolding of nearly all soft tissues. These fibrillar proteins cell and form amorphous masses as a unique response to heat.

The PIET found that there is a difference between unburnt and burnt in tissue measured reflectivity slope with applied stretch. Typically, at least an order of magnitude jump or increments were recorded with the pigskin sample, and as shown in Figure 4.31. Also established was the reproducibility of the results of the experiment, as samples from the identical part of the animals' yields similar reflectivity data with respect to burnt duration, i.e. shoulder and posterior skin. Observed in-vitro shoulder pigskin experimental results showed that as the thermal excitation duration increases, the reflectivity intensities versus applied stretch increases linearly up to a certain duration limit. Where after the thermal threshold, the reflectivity versus stretch slopes changes to a negative values or close to zeroes as shown in Figure 4.32. This is probably due to the breakdown progress of the collagen fibril (as drawn in Figure 2.2) hence the roughness, which is dependent on the collagen found throughout the epidermis and dermis layer. In

future work, the plans are to collaborate this hypothesis with histological studies of the burns.

With this information at hand, the PIET can be used to determine and distinguish type 2A and 2B burns, by the abrupt change of the reflectivity slope. Since, the different between type 2A and 2B burns is where most of the regenerative tissue sub-layer, collagens, and blood vessels found between the dermis and epidermis are completely destroyed or damaged in the latter case and not in the former. From the experiments, typical duration of the thermal excitation ranges for type 2B burns on in-vitro sample as described in sub-chapter 4.3.3.3, is in the range of 70 second, while type 2A burns still exhibits the linear relationship between specular reflected light with stretch. This behavior or trend can still be observed since, the regenerative sub-layer and collagen have not been substantially damaged. Tissue depth damage can also be determined with the use of different wavelength, since it would penetrate different probe depth.

## 5.5 Summary

In comparing the spatial and stretch resolution of ultrasonic imaging, video imaging, and 2-D polarization imaging, it is clear from the present study that 2-D polarization imaging has comparable spatial resolution compared to video motion analysis imaging method and to ultrasonic imaging and video dimension analyzer. The stretch resolution is comparable to that obtained by alternative techniques. The results presented suggest that laser speckle limits the spatial resolution of the technique to about 200μm and the stretch resolution to about 0.3%. By replacing the coherent He-Ne laser source with an incoherent LED, any effects due to speckles are eliminated. The LED data exhibits

smaller reflectivity fluctuations and better spatial (~24μm) and stretch resolution compared to that obtained using the He-Ne laser source. With improved signal averaging and the elimination of detected light fluctuations due to laser speckle, we suspect that the stretch resolution can be improved from what is presented in this dissertation.

The non-biological results observed shows that the reflectivity intensity indeed increases with the amount of stretches applied uniformly across the sample. This helped in establishing the electromagnetics theoretical model of the surface roughness effects and explain the experimental observation.

From the biological experimentation, it was found that the reflectivity measurement of in-vitro pigskin sample also increases with stretch, as with the non-biological sample. However, due to the nature of the in-vitro sample, the reflectivity is invariant of the incident laser wavelength. This is because when the in-vitro samples is removed from the animals, it lacks of the regeneration, blood circulation and metabolism.

In the in-vivo human skin measurement, it was found that the reflectivity slope is dependent on the direction of the stretch being applied. It can be summarized here, that the more flexible the biomechanical properties of the sample or skin is, the larger the reflectivity slope would be measured. It can be exploited or used to distinguish good, or healing tissue from damaged tissue (collagen found in the sub-layer) of the same part of the body, without the use of invasive methods.

For in-vitro burn experiments, the different laser wavelength reflectivity results measured or observe depends on the depth of the thermal damage introduced to the pigskin. Also as the thermal damage to the in-vitro pigskin sample increases, the reflectivity slope measurement increases up to a limit, where any additional thermal

damages to the sample will not increase its reflectivity reading with the applied stretch. In these limit, the biomechanical properties of the in-vitro pigskin sample is completely altered and becomes optically transparent to the incident light as described before. This reflectivity changes observation can be exploited to help and determine the burn wound treatment.

In developing the 2-D polarization imaging as a new technique for imaging soft tissue stretch, it seems that a spatial resolution of about 10-12 microns (factor of 2 better than presented here) and a stretch resolution of about 0.01% (factor of 30 better than presented here) should be possible through the elimination of laser speckle and improved signal averaging. Clearly, if these resolutions are achievable, in-situ/ non-invasive soft-tissue stretch measurements using 2-D polarization imaging could become the state-of-the-art measurement technique compared to existing technology. With these parameters, stretch images of skin could be easily obtained and applied to wound closure/ treatment applications. Moreover, with a spatial resolution of 10-20 microns, the technique opens the possibility of measuring the in-situ biomechanical properties of a variety of materials including tendons, collagen, artificial biomaterials, and other connective tissues with a much finer spatial scale and accuracy then is currently possible.

## 5.6 Anticipated Prospect/Vision

The 2-D PIET and endoscope PIET approaches are a promising new class of diagnostic medical imaging technology that utilizes advanced photonics and fiber optics to obtain images and tissue characterization. When fully exploited, the technology has the potential to dramatically change the way physicians, researchers and scientists see and understand the human body in order to better diagnose and treat disease.

Simply put, PIETs combines the principles of non invasive diagnostics with the imaging performance of a microscope and in a standard instrumentation form that is familiar to clinicians. Whereas ultrasound produces images from backscattered sound "echoes," PIET uses visible light waves that reflect off the internal microstructure within the biological tissues and soft tissue surfaces. The frequencies and bandwidths of visible light are orders of magnitude higher than medical ultrasound signals - resulting in greatly increased image resolution - 8-25 times greater than any existing modality.

Light can be delivered to the imaging site through a single optical fiber only .006" diameter (about the size of the period in this sentence). The imaging guidewire that will contains a complete lens and polarizers assembly will be able to perform a variety of imaging functions. The guidewire can be deployed independently or integrated into existing therapeutic or imaging catheters.

PIET imaging can be performed over approximately the same distance of a biopsy at high resolution and in real time making it an attractive application, where conventional biopsies cannot be performed or are ineffective.

In addition to providing high-level resolutions for the evaluation of microanatomic structures PIET is inherently able to provide information regarding tissue composition/roughness. Using spectroscopy (i.e. via Optical Spectrum Analyzer), users can evaluate the spectral absorption characteristics of tissue while simultaneously determining the orderliness of the tissue through the use of polarization imaging.

Advantages of PIETs system;

- High resolution: Current prototype systems have resolutions at 20-24 um compared to 110 um for high frequency ultrasound.

- Small size: The fiber-based design allows easy integration with small catheter/endoscopes.
- Real time imaging: Imaging is at or near real time. PC Based, Digital system architecture (via Labview) enables a compact, portable easily upgraded system.

The endoscopic embodiment of PIET, as described before would greatly heighten and promote its use as a non-invasive diagnostics in the medical fields. Enclosed tissues such as throat, lungs and colon can now be probed without invasive surgery. Furthermore, in vocal cord treatment, where it is impossible to attach any stretching device to the vocal cord in the enclosed place, the tension and stress of the vocal cord during vocalization is best investigated with the PIET endoscopy. Preliminary data from the endoscopy experiment shows that the reflectivity changes due to the change in the tension experienced and hence its surface roughness follows the linear relationship as in the bulk optics system approaches.

For the endoscopic approach several type of polarization maintaining optical fiber, core diameter ranging from 5.5 um to 250 um, are being tested. It was found that the requirement of the total diameter of the optical fiber must be smaller then the inherent standard utility port/instrument channel diameter of the endoscope, namely 2.8 mm. Optical fiber bundle, made form PVC, plastics, and glass are also being put to test. The total reflected intensity measured was found to increases with stretch, but the polarization information were not preserved after propagating thru the fiber bundle. In this particular setup, besides the automation data acquisition described as above being used, the use of an optical spectrum analyzer, along with a broadband source would improve the measurement. In order to validate this approach, the initial background work or tests,

were made on a used commercial endoscope. The schematic for the endoscope experiment is as illustrated in the Figure 3.9 above. Polarization tests on the Pentax endoscope optical fiber system showed the original endoscope fiber does not maintain the polarization of the coherent incidence light. This problem can be circumvented to some extent by placing a polarizing filter between the sample and endoscopic fiber. In this configuration, a linear reflectivity versus stretch curve for plastic samples was measured. However, the results are only reproducible and stable if there is no movement of the endoscope i.e. flexing, twisting, bending of the tube. This is easily understood since motion of the fiber results in varying birefringence in the fiber due to stresses. Hence, in order to develop an endoscope system that might work in a clinical setting as the future work, the endoscope system need to be modified with the use of a polarization maintaining fibers and additional polarizers in order to use the PIET method.

Future approaches includes the proposal to obtain and test the endoscope with a polarization maintaining optical fiber inserted in the working chamber (auxiliary tube). Also, several designs of the endoscope head were envisioned, but the most feasible ones are as depicted below;

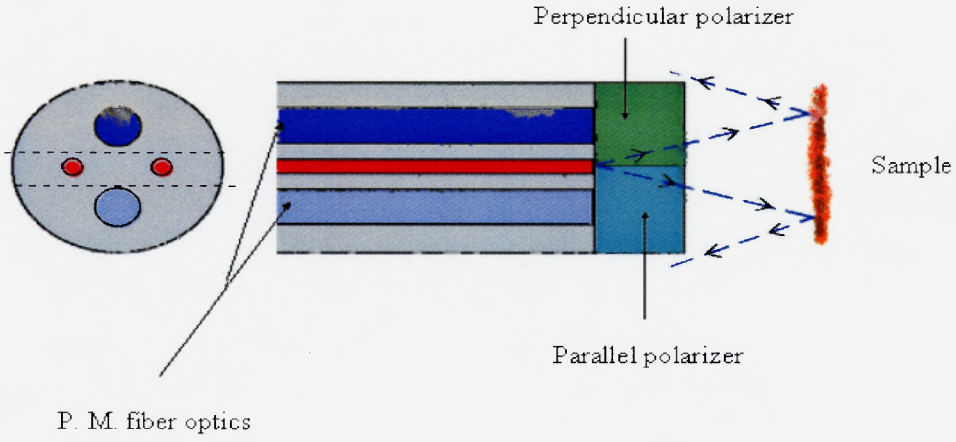


**Figure 5.1** First recommended modification of endoscope sensing probe.

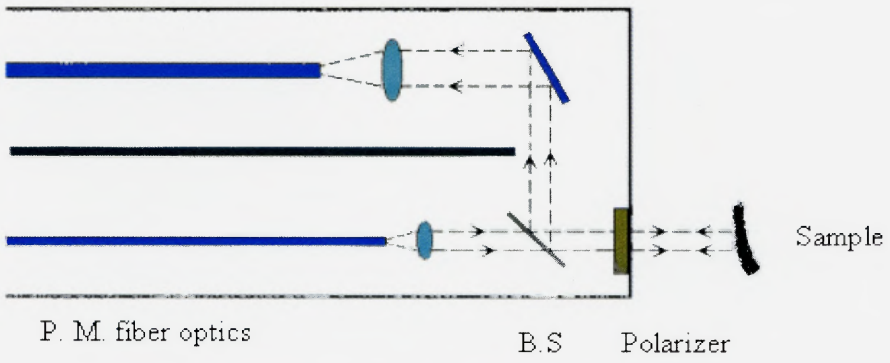


**Figure 5.2** Second recommended modification of the endoscope sensing head.

For the ultimate application in vocal cord diagnostics, the endoscopy system could be tested on the vibrating latex sample with known frequencies of vibration that mimic the physical property of the vocal cords. The anticipated results from the vibrating vocal cord that gives rise to the measured waveform is as shown in Figure 5.3. Important information about the vocal cord can be inferred from the observed waveform. The waveform can be analyzed since it will contain the tension or stress information in the waveform frequency properties and the waveform offset will have the stretch information embedded in it.

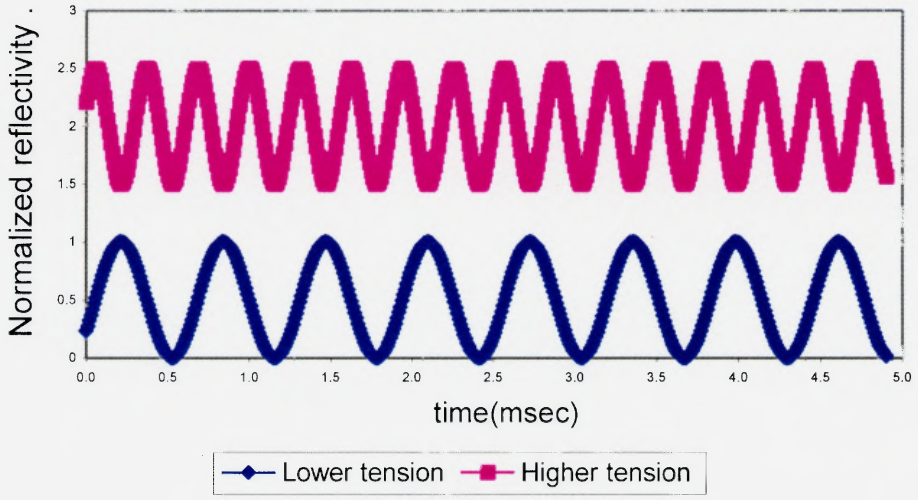


**Figure 5.3** Vocal cord anticipated reflectivity results

In additions, possible solutions or approaches to compensate the movement of the endoscope's tube via software are also in design and further experimental work to re-confirm that the endoscope works under various different or same conditions and sample is also planned.

The next move to make the PIET more applicable in burn diagnostics is to investigate and extract the depth of burnt or tissues damages in-vivo specimen experiment. As portrayed in Figure 2.3, multi wavelength from a broad band white light source, could be used as the source of the polarized light. With the help of an optical spectrum analyzer, healthy and death cell information from different tissues depth can be examine non invasively and obtained in close to real time data acquisition. The information would provide insight and burnt treatment decision, i.e. to graft the wound or not.

A further enhancement of the development of the techniques is to measure that reflectance of the soft tissues as a function of the tension or force of the applied stretch. The anticipated observation is that the reflectivity intensity is linearly proportional to the force of the stretch, while its slope would provide in depth details of the biomechanical properties of the specimen, i.e. spring constant, Young modulus. The force or tension experienced by the sample with respect to the stretch applied plot slope will provide the information about the elasticity of the sample or spring constant. While the reflectivity versus stretch slope would yields, the biomechanical properties of different sample spring constant. Their corresponding anticipated graphs are as shown in Figure 5.4 and Figure 5.5. Next, by plotting the respective reflectivity graph slope versus the force graph slope, the mechanical properties of the sample could be related to its surface roughness or

topology. With this information at hand, a miniature device that relates the reflectivity to the tension due to stretch or pull can be build to help a surgeon to perfect and optimize the art of suturing.

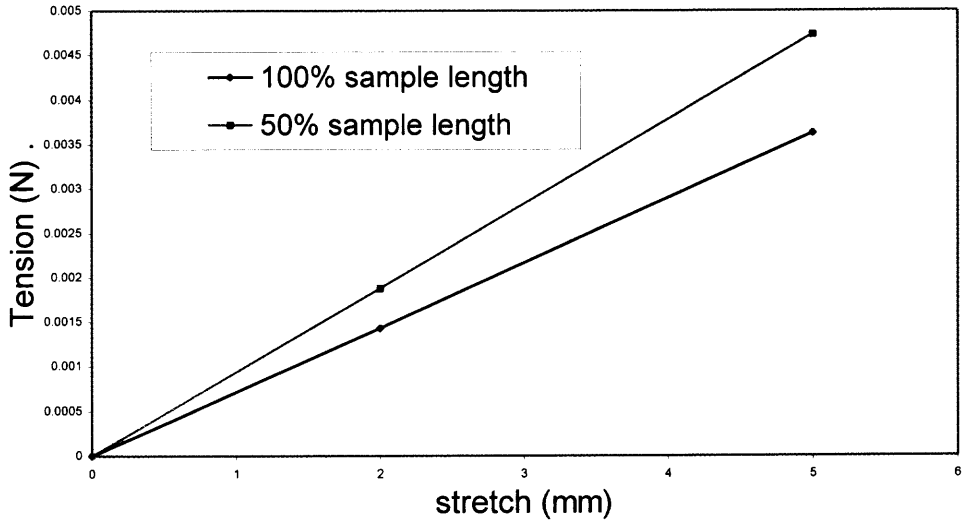


**Figure 5.4** Anticipated force vs. stretch results for different sample length.

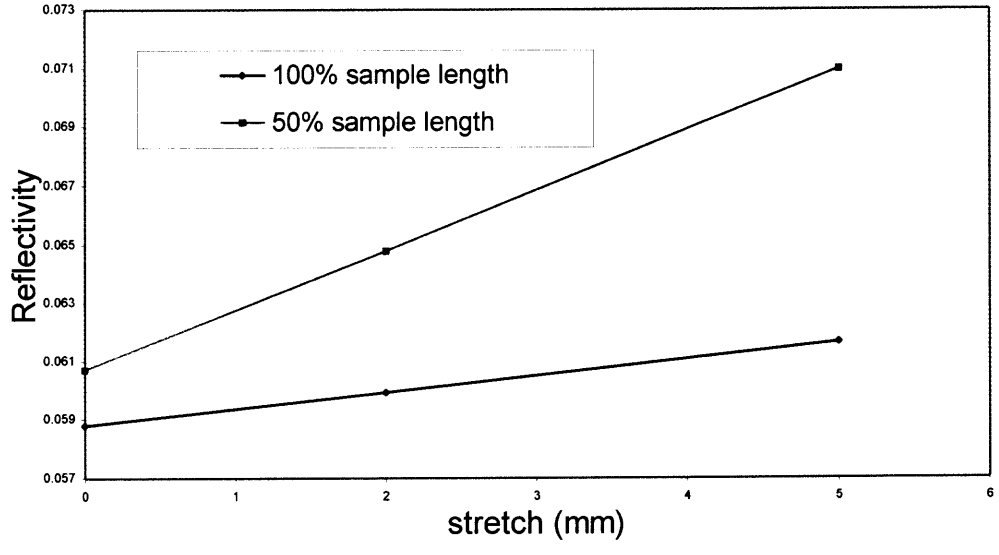


**Figure 5.5** Anticipated reflectivity vs. stretch results for different sample length.

# APPENDIX A

## ALGORITHM FOR IMAGES PROCESSING

The algorithms designed and written specially for the image digitization task using Mathcad Professional 2000 version are as listed. Also, included are the codes for the different type of surface contour and the respective cross sectional comparative plots.

Read images into RGB matrices

A := READRGB("C:\WINDOWS\My computer\biomedical\forearm data 2-26-99\0-0.bmp" )

B := READRGB("C:\WINDOWS\My computer\biomedical\forearm data 2-26-99\0-90.bmp" )

C := READRGB("C:\WINDOWS\My computer\biomedical\forearm data 2-26-99\1mm-0-0.bmp" )

D := READRGB("C:\WINDOWS\My computer\biomedical\forearm data 2-26-99\0-90.bmp" )

Separate the the read images into Red, Green and Blue portion for data analysis

$a := \max(A)$

$a = 255$

$w := \frac{\text{cols}(A)}{3}$

$w = 40$

$c := \max(C)$

$c = 255$

$v := \frac{\text{cols}(C)}{3}$

$v = 40$

$b := \max(B)$

$b = 255$

$x := \frac{\text{cols}(B)}{3}$

$x = 40$

$d := \max(D)$

$d = 255$

$z := \frac{\text{cols}(D)}{3}$

$z = 40$

Red, Blue and Green images and their respectives sub-matrices


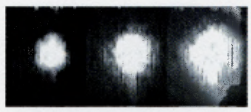
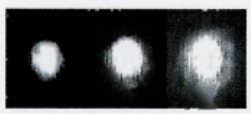
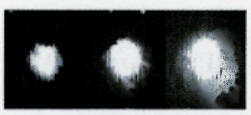

$$w := \frac{cols(A)}{3}$$

| | | |
|---|---|---|
| $rdog := submatrix(A, 0, rows(A) - 1, 0, w - 1)$ | $r := max(rdog)$ | $r = 255$ |
| $gdog := submatrix(A, 0, rows(A) - 1, w, 2 \cdot w - 1)$ | $g := max(gdog)$ | $g = 255$ |
| $bdog := submatrix(A, 0, rows(A) - 1, 2 \cdot w, 3 \cdot w - 1)$ | $b := max(bdog)$ | $b = 255$ |
| $rdg := submatrix(B, 0, rows(B) - 1, 0, w - 1)$ | $r1 := max(rdg)$ | $r1 = 255$ |
| $gdg := submatrix(B, 0, rows(B) - 1, w, 2 \cdot w - 1)$ | $g1 := max(gdg)$ | $g1 = 255$ |
| $bdg := submatrix(B, 0, rows(B) - 1, 2 \cdot w, 3 \cdot w - 1)$ | $b1 := max(bdg)$ | $b1 = 255$ |
| $rdg1 := submatrix(C, 0, rows(C) - 1, 0, w - 1)$ | $r2 := max(rdg1)$ | $r2 = 255$ |
| $gdg1 := submatrix(C, 0, rows(C) - 1, w, 2 \cdot w - 1)$ | $g2 := max(gdg1)$ | $g2 = 255$ |
| $bdg1 := submatrix(C, 0, rows(C) - 1, 2 \cdot w, 3 \cdot w - 1)$ | $b2 := max(bdg1)$ | $b2 = 255$ |
| $rdg2 := submatrix(D, 0, rows(B) - 1, 0, w - 1)$ | $r3 := max(rdg2)$ | $r3 = 255$ |
| $gdg2 := submatrix(D, 0, rows(B) - 1, w, 2 \cdot w - 1)$ | $g3 := max(gdg2)$ | $g3 = 255$ |
| $bdg2 := submatrix(D, 0, rows(B) - 1, 2 \cdot w, 3 \cdot w - 1)$ | $b3 := max(bdg2)$ | $b3 = 255$ |

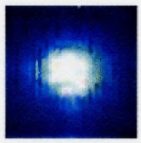

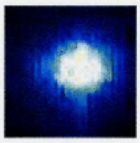


Top 2 images are the unstretched soft tissue, of 0-0 and followed by 0-90 degrees measurements
Bottom 2 images are the stretched soft tissue, of 0-0 and followed by 0-90 degrees measurements

Surface contour plots of the unstretched and stretched images, 0-0 (left) and 0-90 (right) degrees measurements

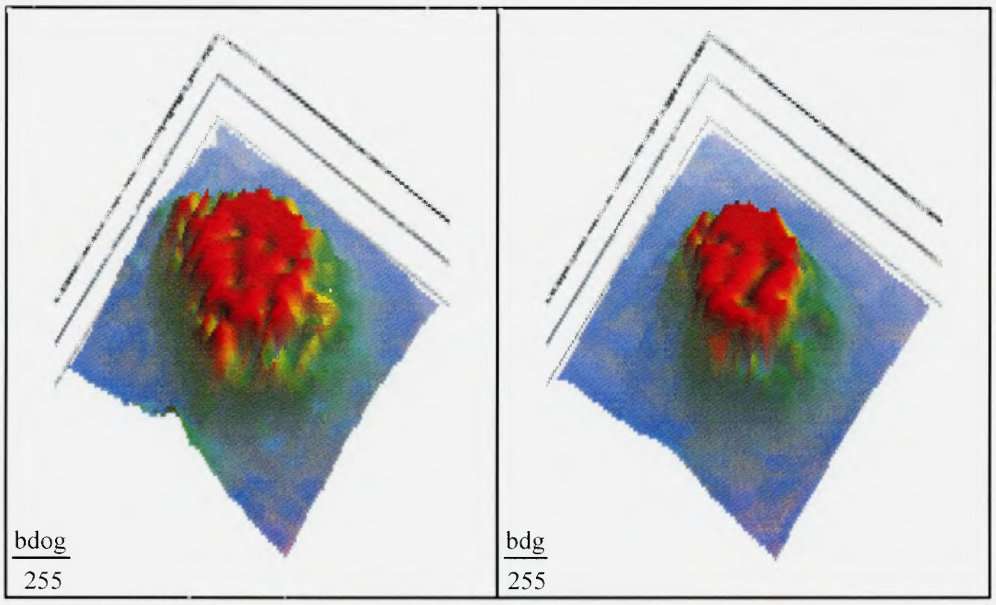


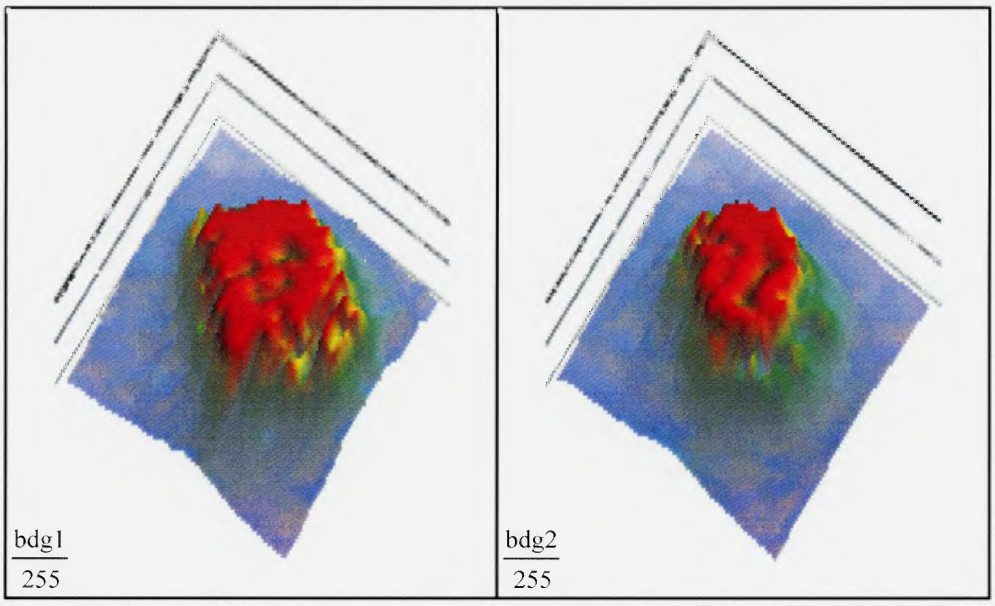

Algorithm for cross sectional plotting

$$\text{cond}(x) := x \geq 1.0$$

$$\text{Locate}(A, \text{cond}) := \left| \begin{array}{l} i \leftarrow 0 \\ L \leftarrow 0 \\ \text{for } m \in 0..\text{rows}(A) - 1 \\ \quad \text{for } n \in 0..\text{cols}(A) - 1 \\ \quad\quad \text{if } \text{cond}\left(A_{m,n}\right) = 1 \\ \quad\quad\quad \left| \begin{array}{l} L^{\langle i \rangle} \leftarrow \begin{pmatrix} m \\ n \end{pmatrix} \\ i \leftarrow i + 1 \end{array} \right. \\ L \end{array} \right.$$

$$L := \text{Locate}(bdog, \text{cond})$$

$$d090 := \frac{B}{255} \qquad d00 := \frac{A}{255} \qquad i := 0..39$$

$$d0090 := \frac{D}{255} \qquad d0000 := \frac{C}{255}$$

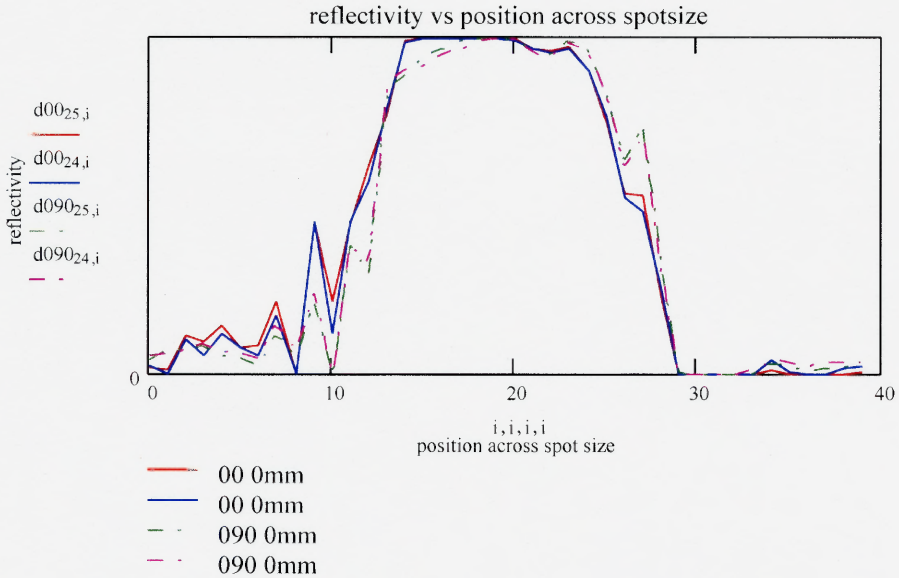

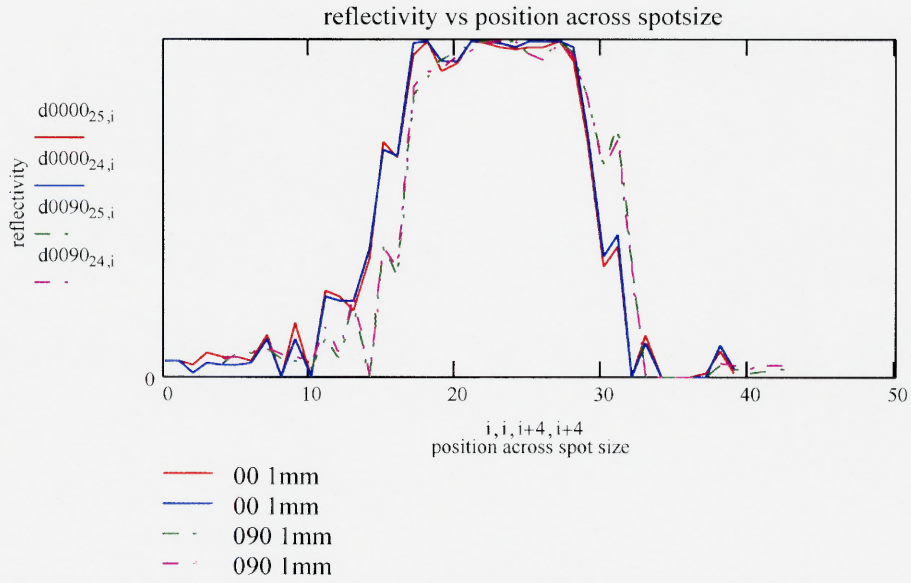


condi := 1

$$\text{minus}(x, y, \text{condi}) := \left| \begin{array}{l} i \leftarrow 0 \\ Q \leftarrow 0 \\ \text{for } m \in 0..\text{rows}(x) - 1 \\ \quad \text{for } n \in \text{condi}..\text{cols}(x) - 1 \\ \quad\quad \left(Q_{m,n} \leftarrow x_{m,n-\text{condi}} - y_{m,n}\right) \\ Q \end{array} \right.$$

q1 := minus(d00, d090, 1)

$$\text{plus}(x, y, \text{condi}) := \left| \begin{array}{l} i \leftarrow 0 \\ P \leftarrow 0 \\ \text{for } m \in 0..\text{rows}(x) - 1 \\ \quad \text{for } n \in 0..\text{cols}(x) - \text{condi} - 1 \\ \quad\quad \left(P_{m,n} \leftarrow x_{m,n+\text{condi}} - y_{m,n}\right) \\ P \end{array} \right.$$

q2 := plus(d0000, d0090, 4)

i := 0.. 39

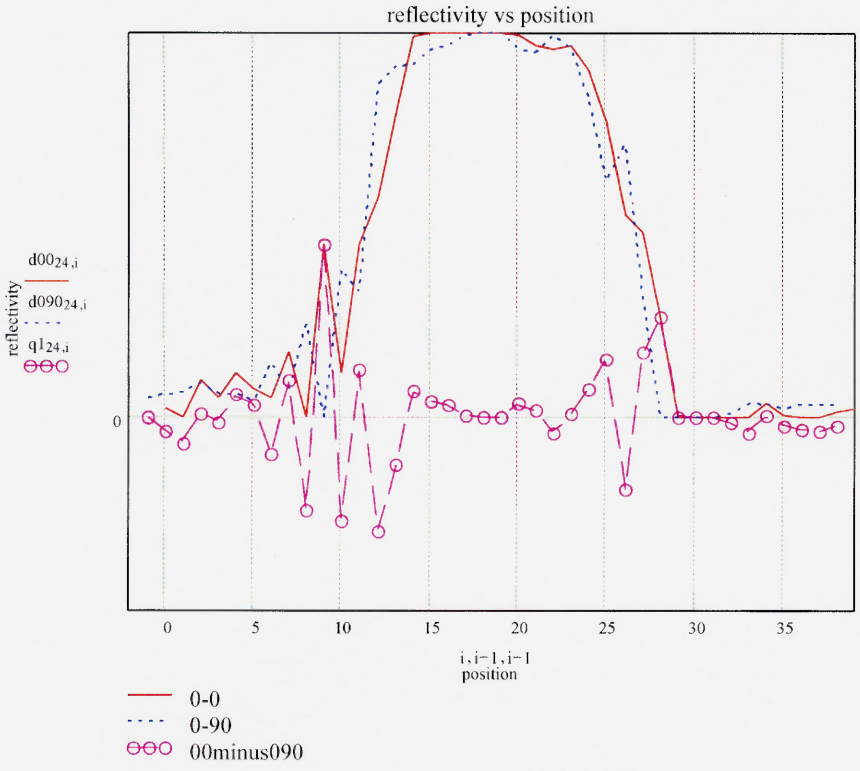


i := 0.. 39

i := 0.. 39

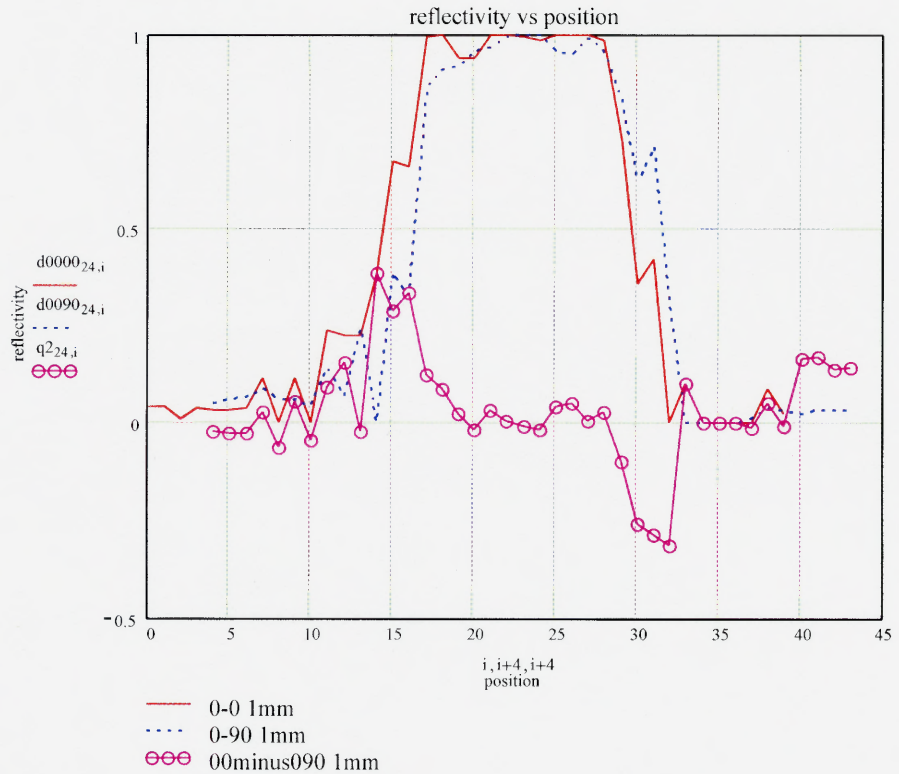

# APPENDIX B

## LABVIEW PROGRAM FOR AUTOMATED DATA ACQUISITION

Labview programs written for Stanford Research SR510 lock-in amplifier, EG&G lock-in amplifier, Klinger stepper motor controller and its accompanying translation stages.

sr510 eg&g klinger.vi

Front Panel

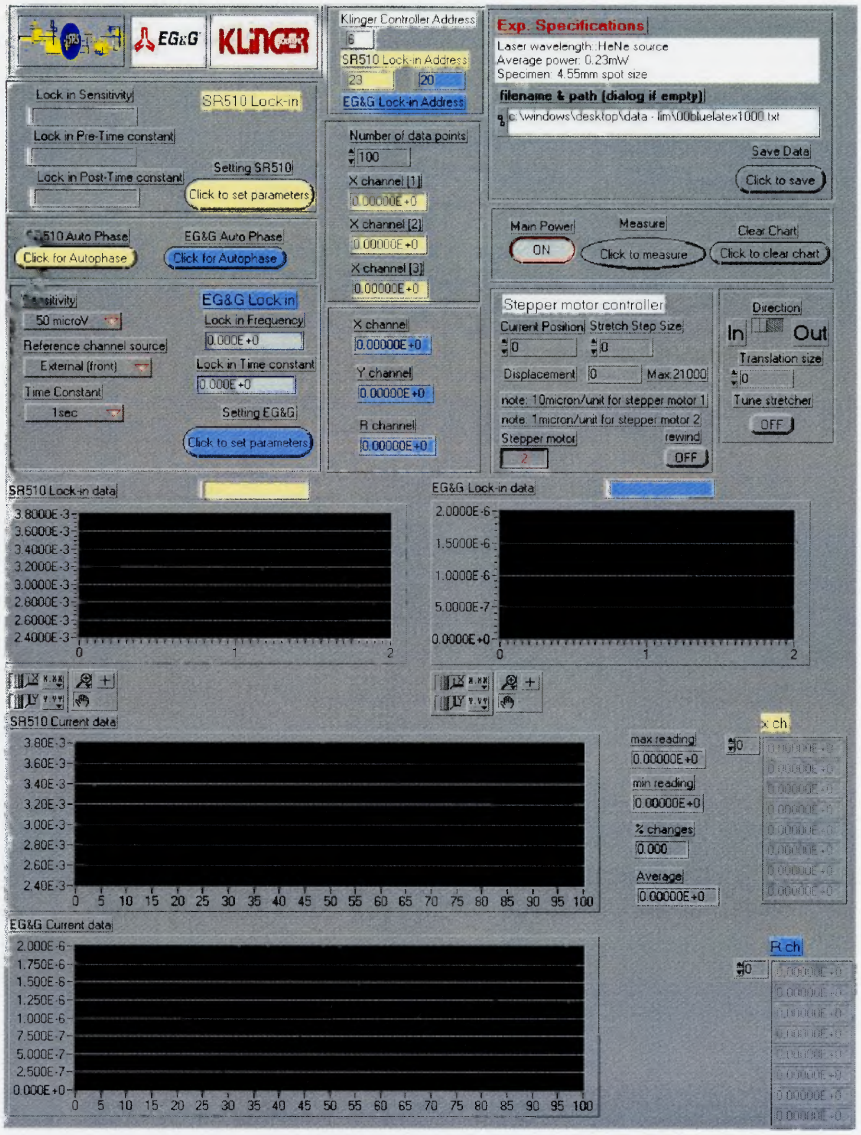

Block Diagram

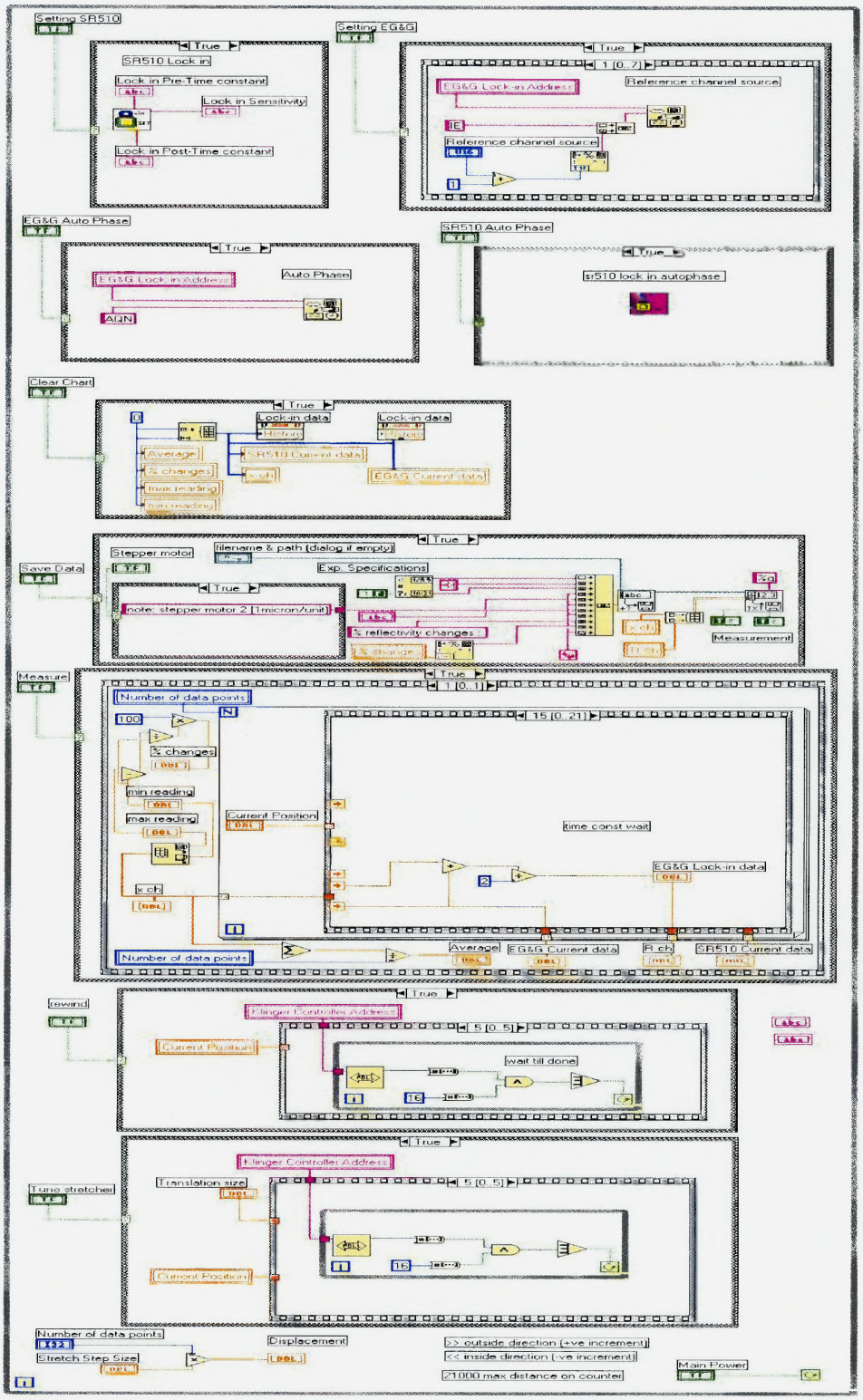


False

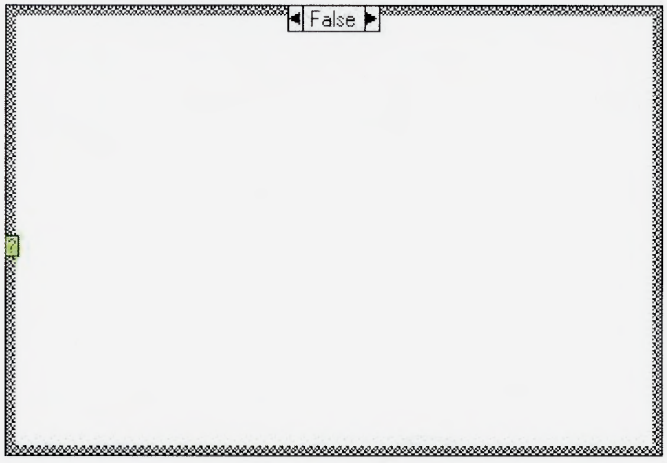
False

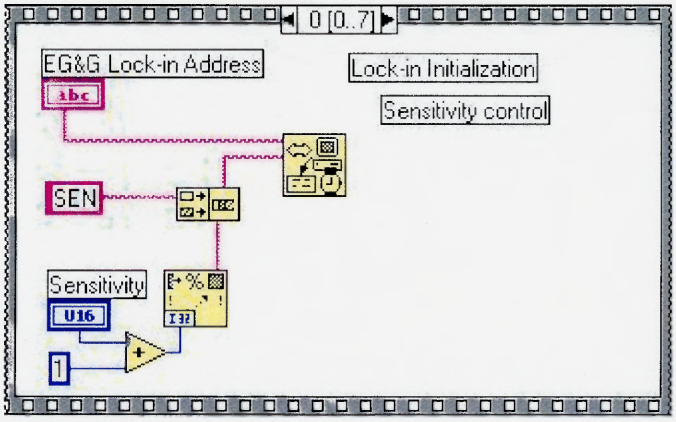
0 [0..7]
EG&G Lock-in Address
abc
Lock-in Initialization
Sensitivity control
SEN
Sensitivity
U16
I32
1

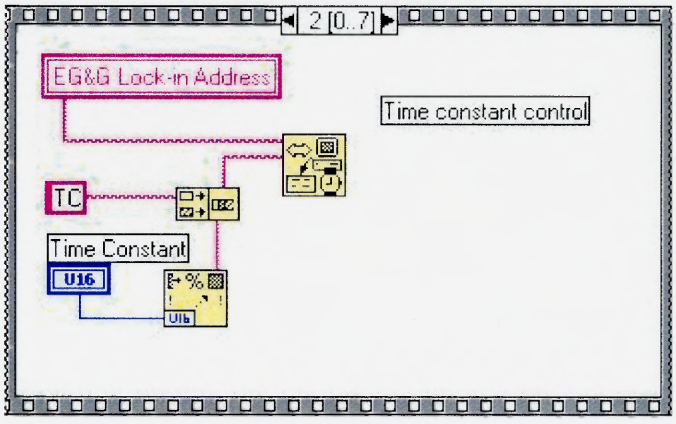
2 [0..7]
EG&G Lock-in Address
Time constant control
TC
Time Constant
U16
U16

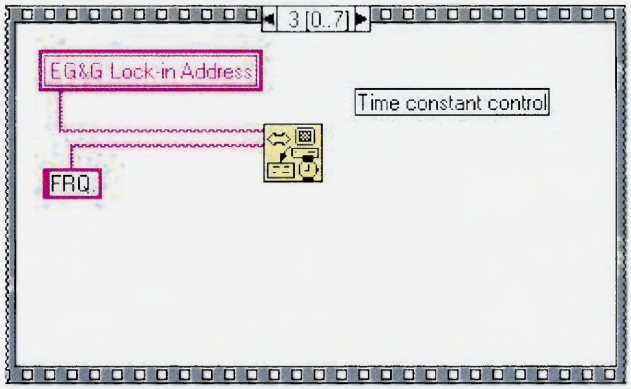
3 [0..7]
EG&G Lock-in Address
Time constant control
FRQ.

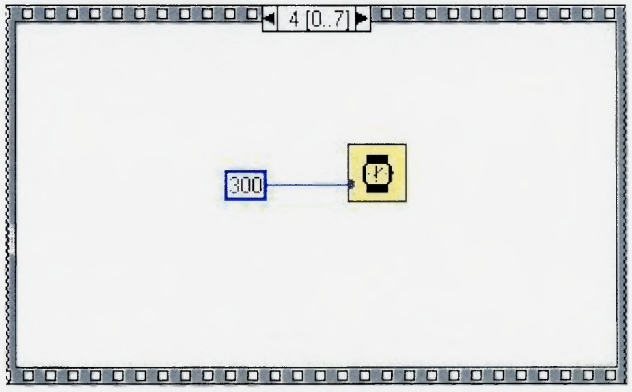
4 [0..7]
300

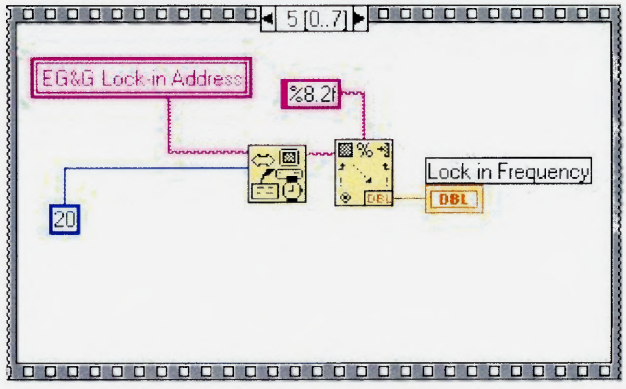
5 [0..7]
EG&G Lock-in Address
%8.2f
Lock in Frequency
DBL
20

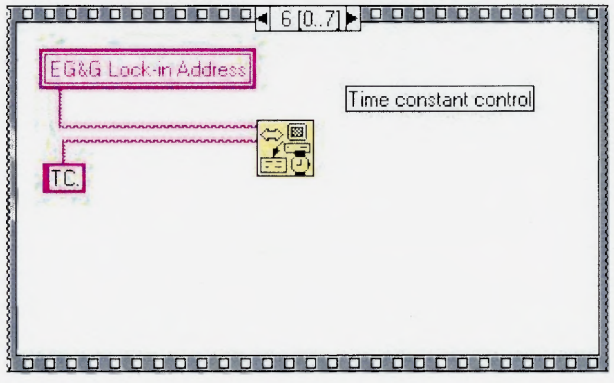
6 [0..7]
EG&G Lock-in Address
Time constant control
TC.

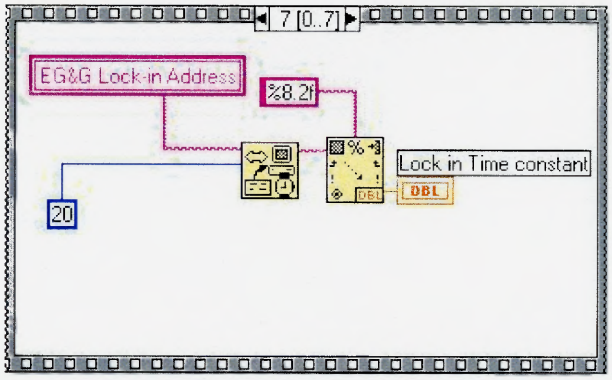
7 [0..7]
EG&G Lock-in Address
%8.2f
Lock in Time constant
DBL
DBL
20

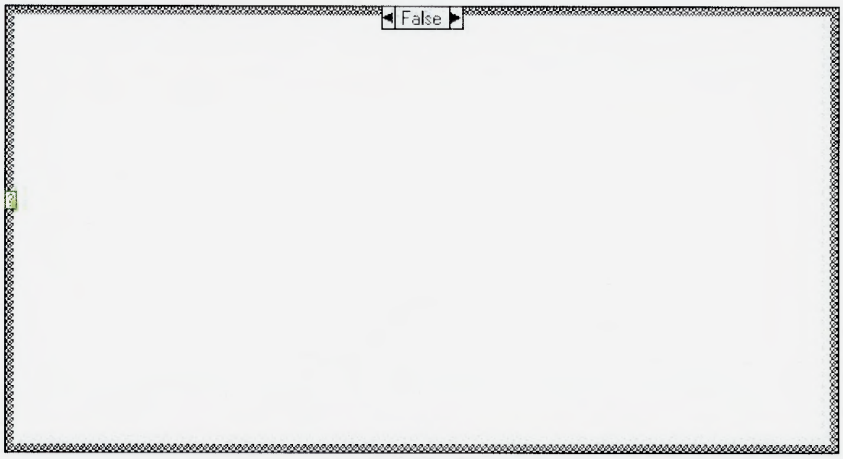
False

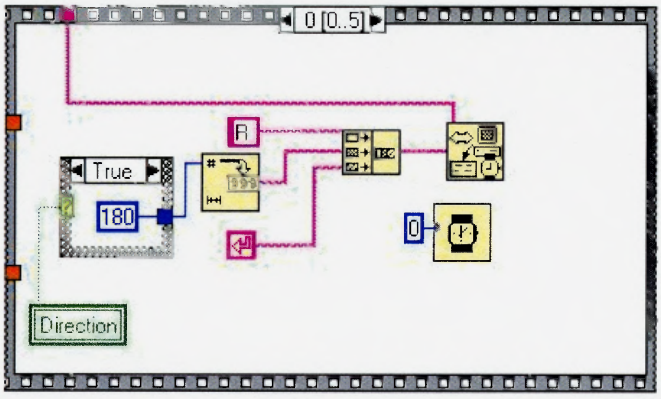
0 [0..5]
R
True
180
0
Direction


False
245

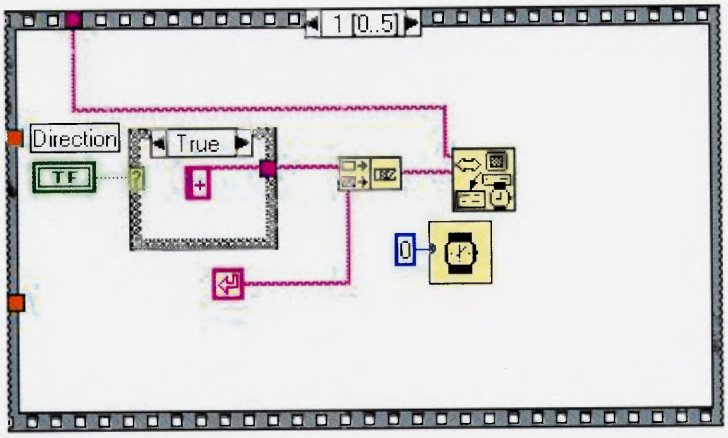
1 [0..5]
Direction
TF
True
0

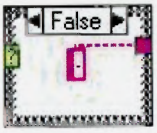
False

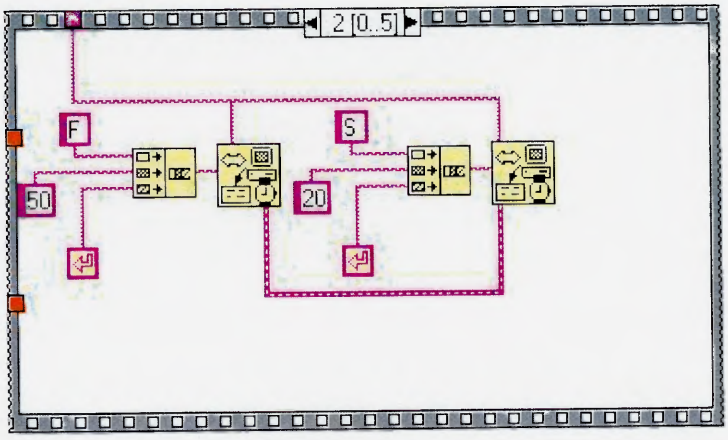
2 [0..5]
F
50
S
20

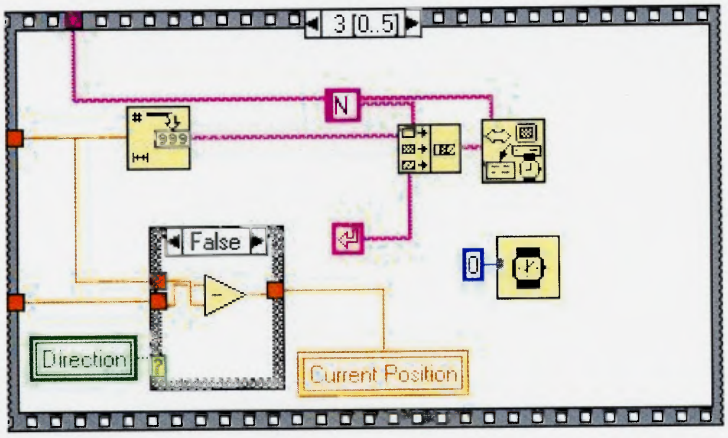
3 [0..5]
N
999
False
0
Direction
Current Position

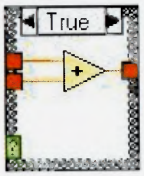
True

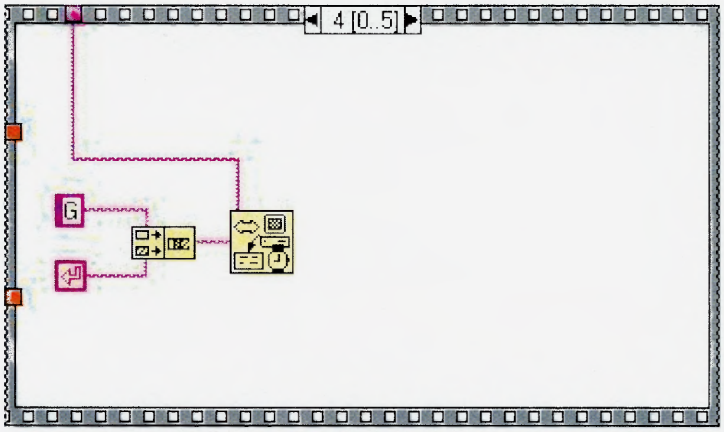
4 [0..5]
G

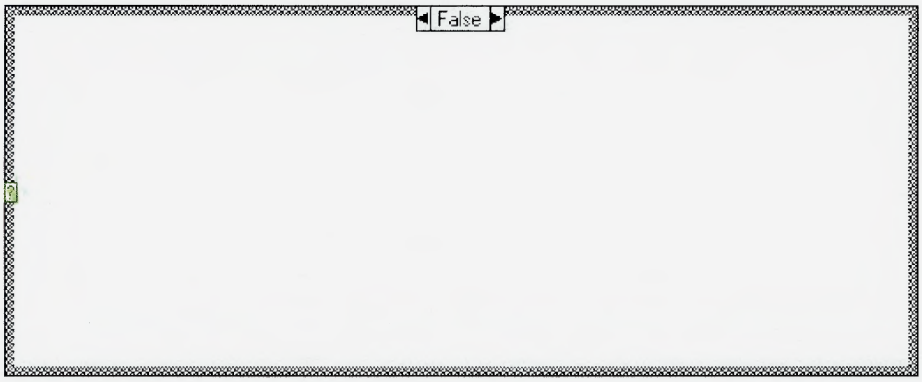
False

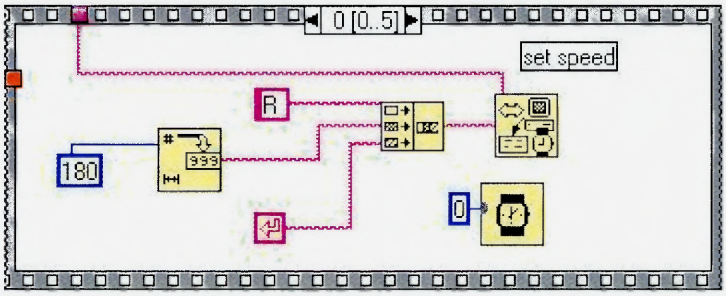
0 [0..5]
set speed
R
180
0

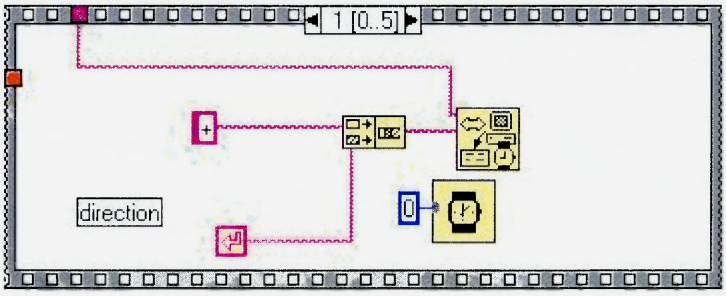
1 [0..5]
direction
0

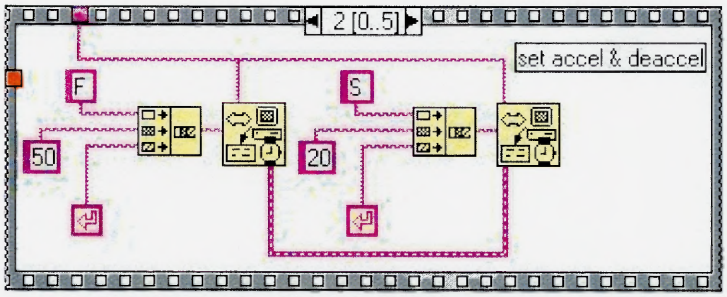
2 [0..5]
set accel & deaccel
F
50
S
20

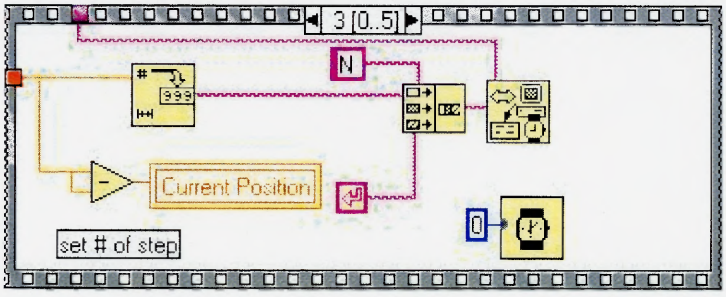
3 [0..5]
N
999
Current Position
set # of step
0

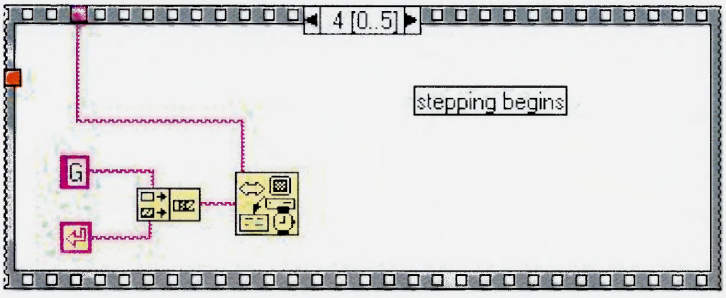
4 [0..5]
stepping begins
G

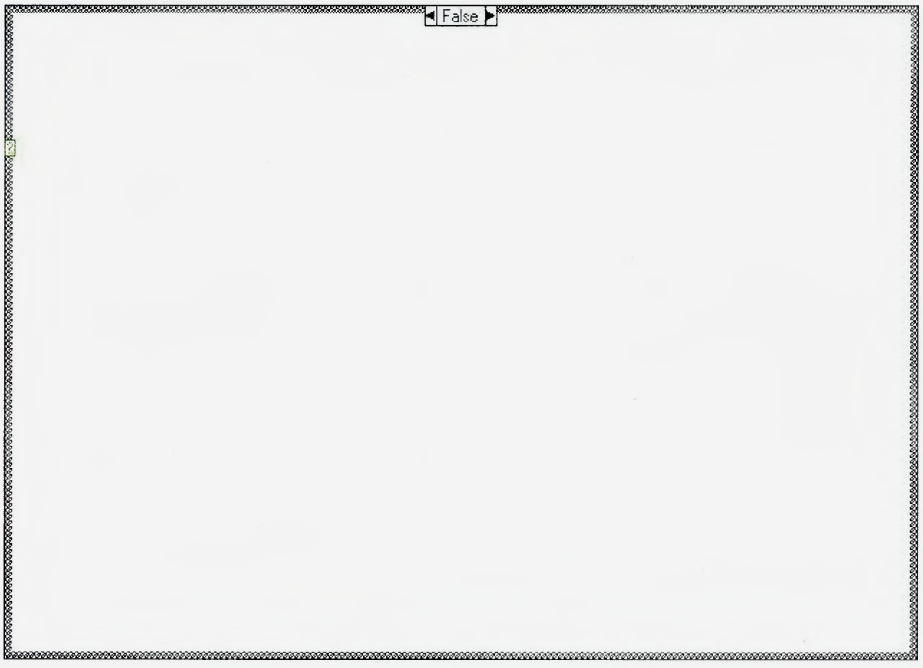
False

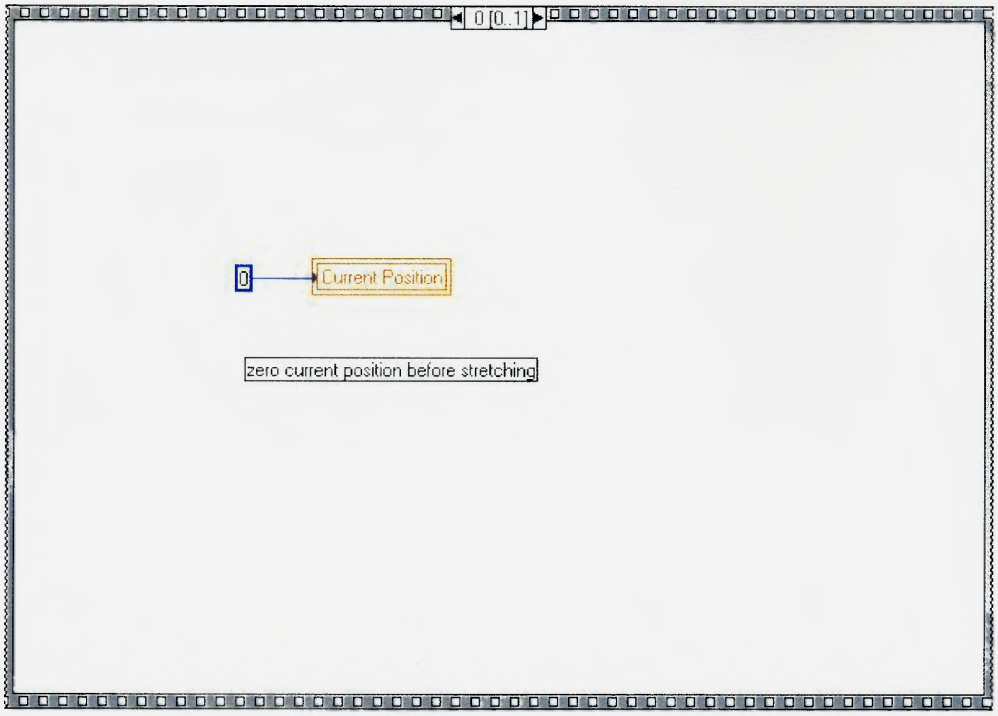
0 [0..1]
0
Current Position
zero current position before stretching

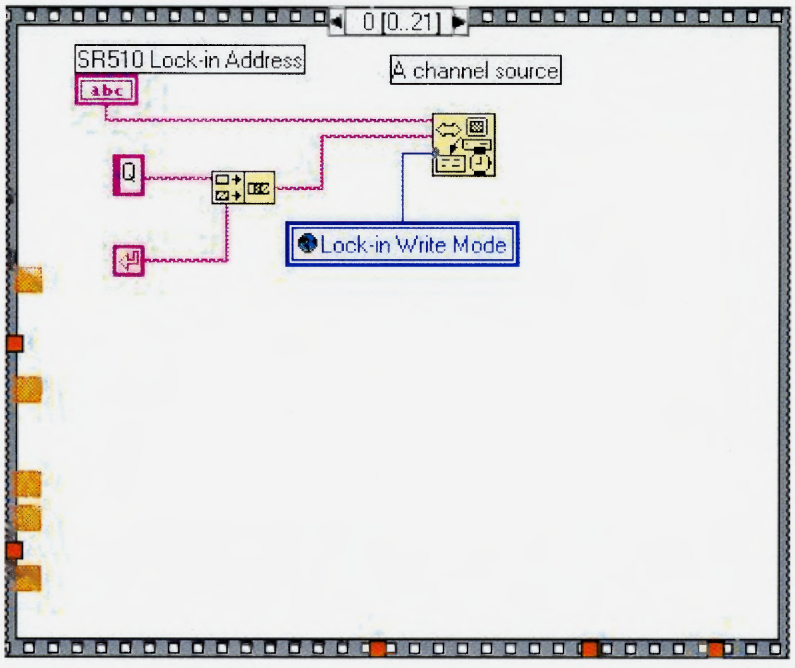
0 [0..21]
SR510 Lock-in Address
abc
A channel source
Q
Lock-in Write Mode

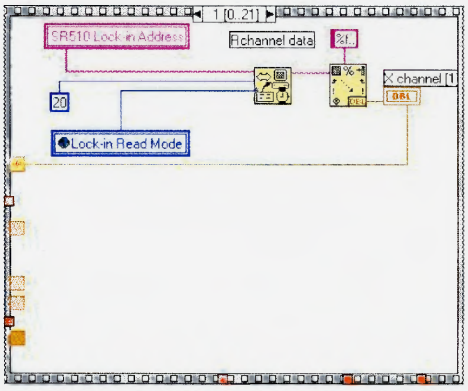
1 [0..21]
SR510 Lock-in Address
R channel data
%f
X channel [1]
DBL
20
Lock-in Read Mode

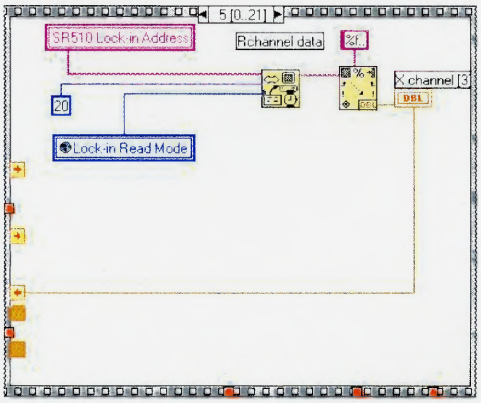
5 [0..21]
SR510 Lock-in Address
R channel data
%f
X channel [3]
DBL
20
Lock-in Read Mode

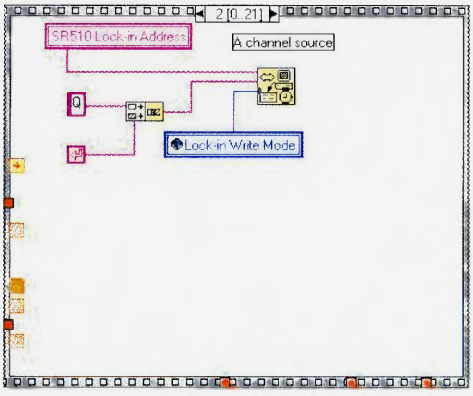
2 [0..21]
SR510 Lock-in Address
A channel source
Q
Lock-in Write Mode

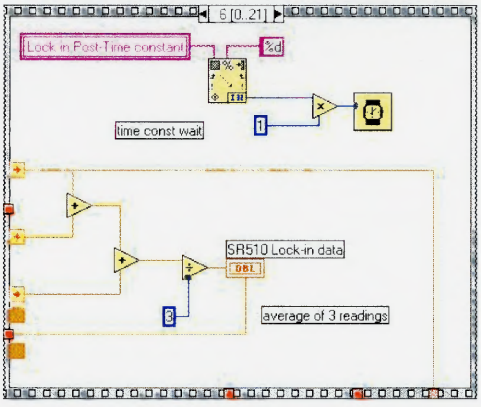
6 [0..21]
Lock-in Post-Time constant
%d
time const wait
1
SR510 Lock-in data
DBL
3
average of 3 readings

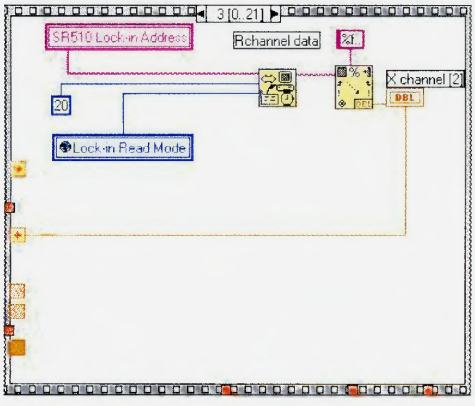
3 [0..21]
SR510 Lock-in Address
R channel data
%f
X channel [2]
DBL
20
Lock-in Read Mode

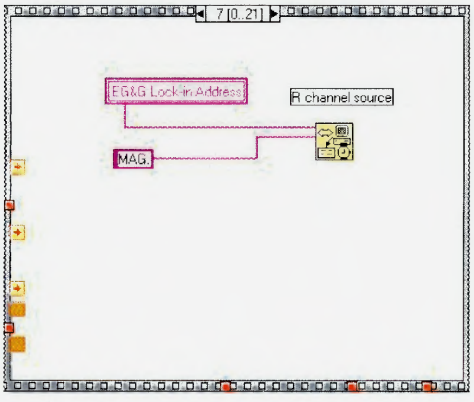
7 [0..21]
EG&G Lock-in Address
R channel source
MAG

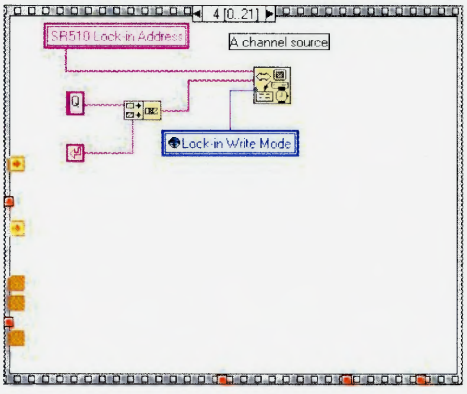
4 [0..21]
SR510 Lock-in Address
A channel source
Q
Lock-in Write Mode

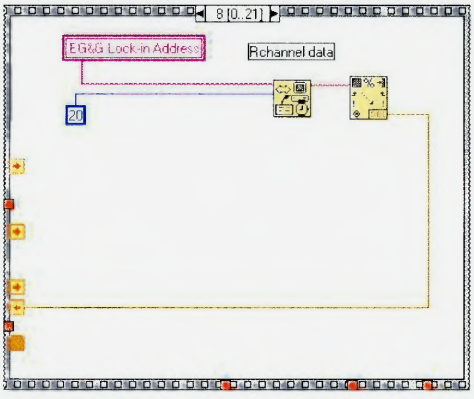
8 [0..21]
EG&G Lock-in Address
R channel data
20

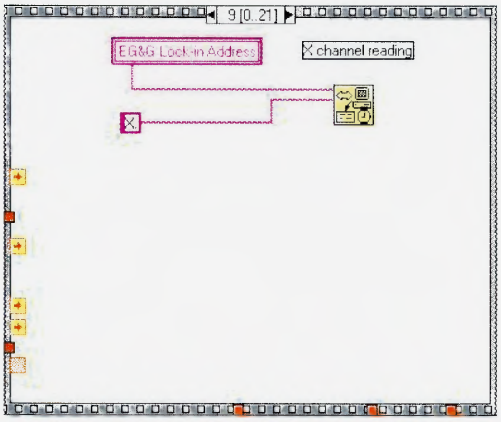
9 [0..21]
EG&G Lock-in Address
X channel reading
X

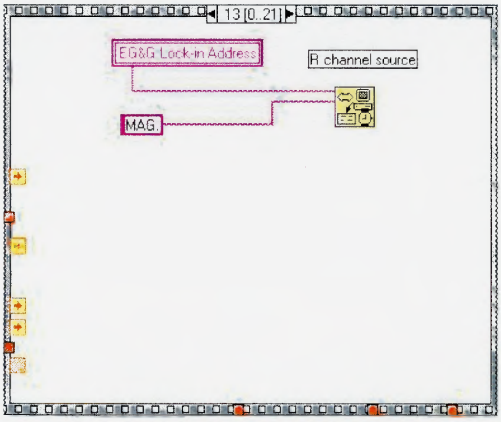
13 [0..21]
EG&G Lock-in Address
R channel source
MAG.

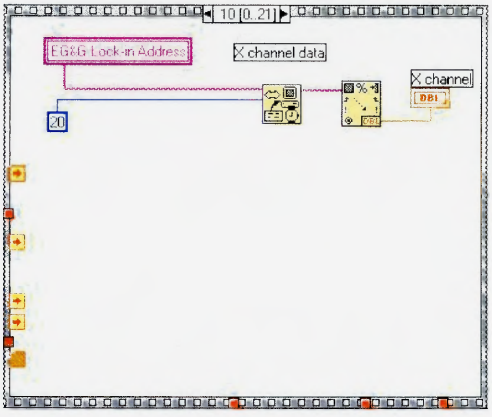
10 [0..21]
EG&G Lock-in Address
X channel data
X channel
DBL
20

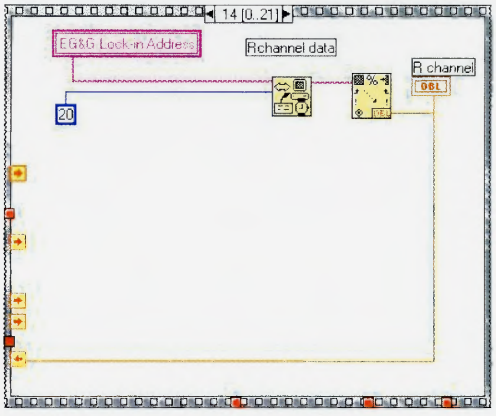
14 [0..21]
EG&G Lock-in Address
Rchannel data
R channel
DBL
20

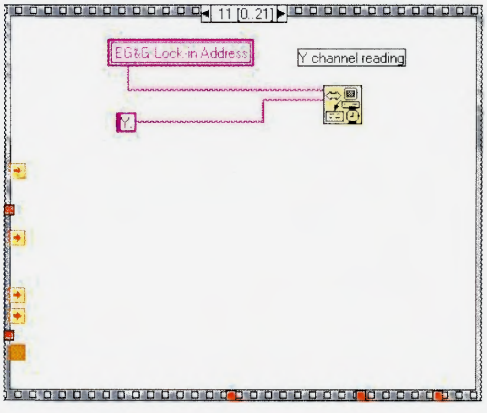
11 [0..21]
EG&G Lock-in Address
Y channel reading
Y

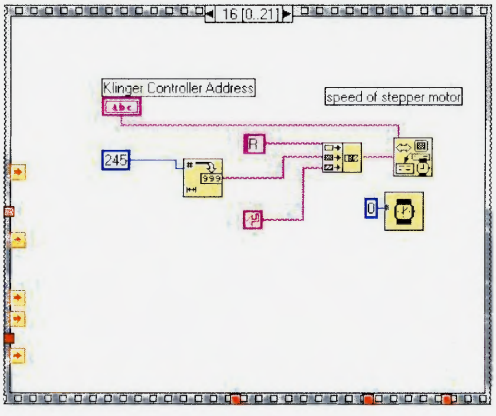
16 [0..21]
Klinger Controller Address
speed of stepper motor
245
0

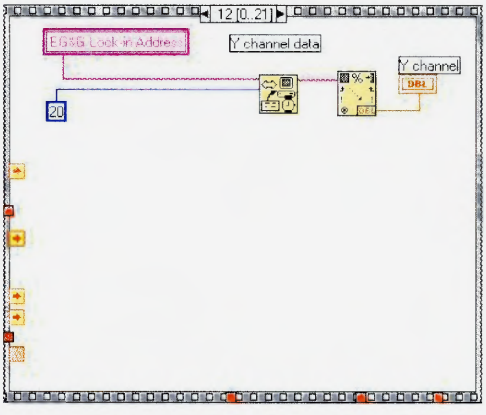
12 [0..21]
EG&G Lock-in Address
Y channel data
Y channel
DBL
20

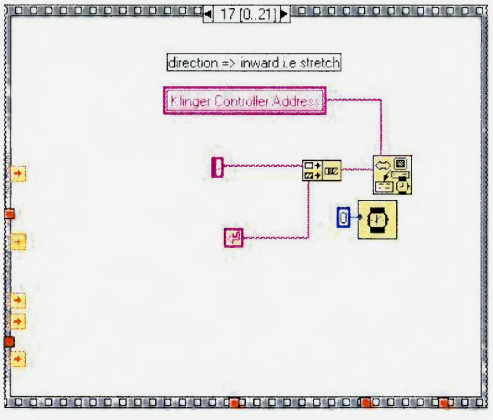
17 [0..21]
direction => inward i.e stretch
Klinger Controller Address
0

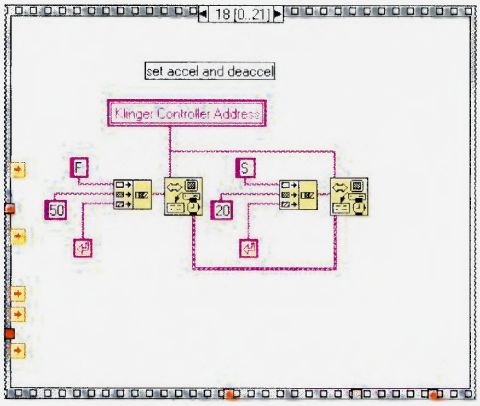
18 [0..21]
set accel and deaccel
Klinger Controller Address
F
50
S
20

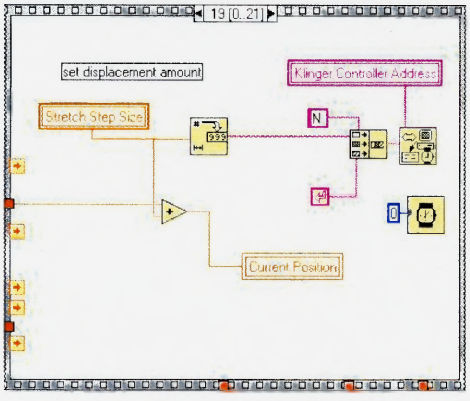
19 [0..21]
set displacement amount
Klinger Controller Address
Stretch Step Size
N
0
Current Position

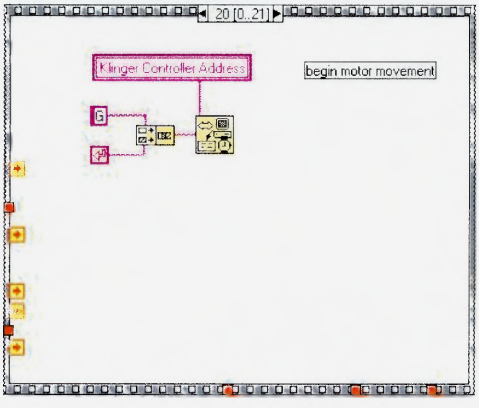
20 [0..21]
Klinger Controller Address
begin motor movement
G

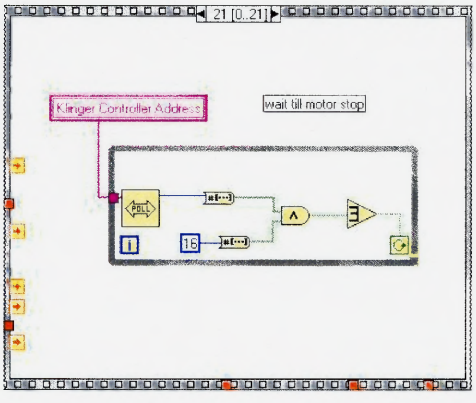
21 [0..21]
Klinger Controller Address
wait till motor stop
1
16


False

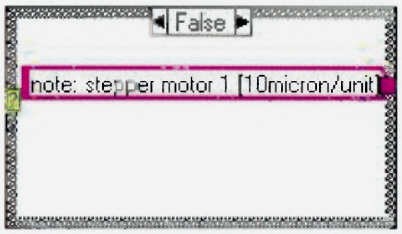
False
note: stepper motor 1 [10micron/unit]


False

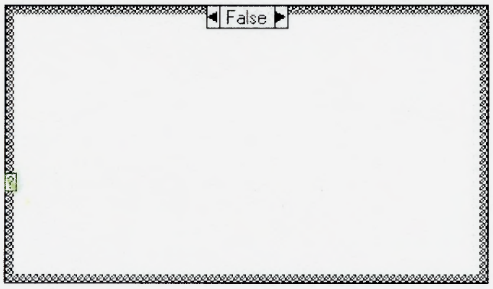
False

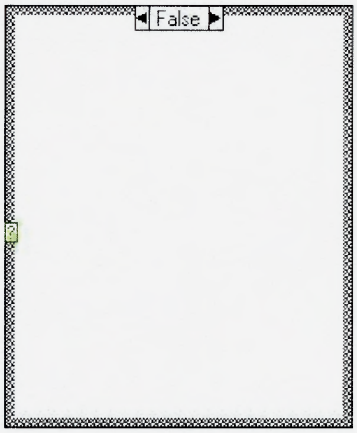
False

Lock in autophase.vi

Front Panel

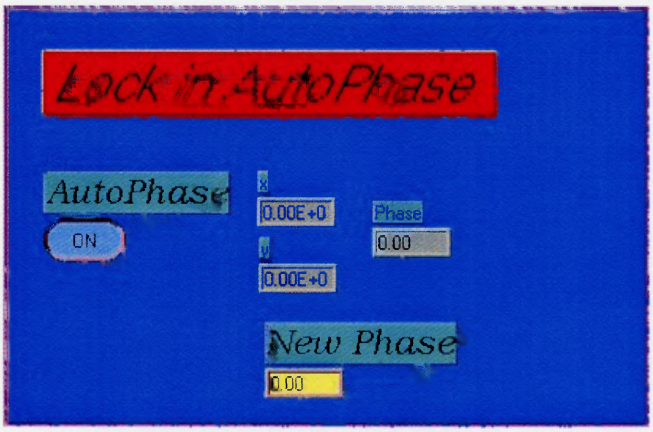


Block Diagram

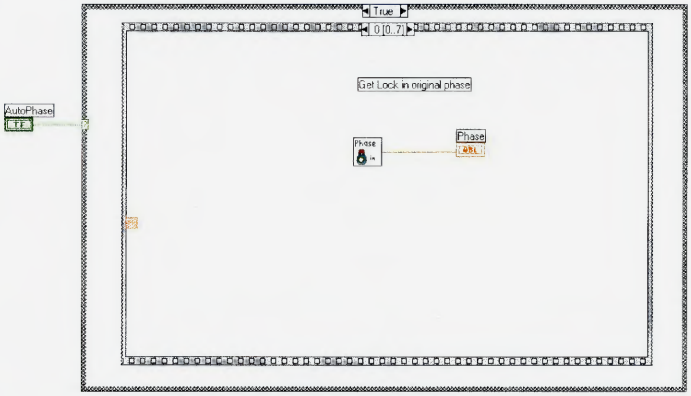


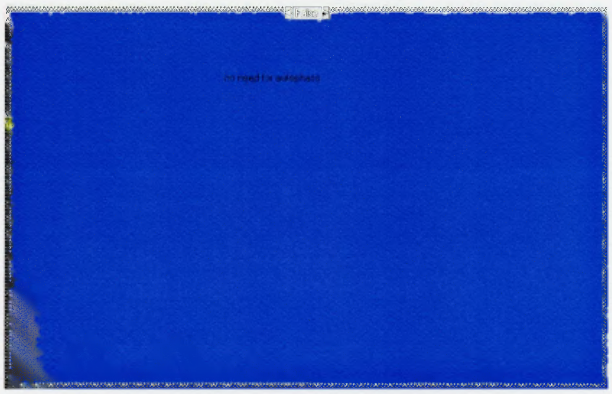

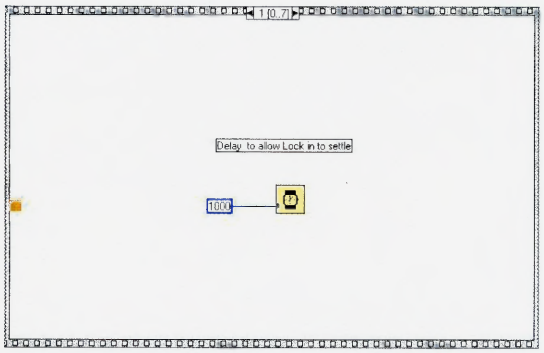
1 [0..7]
Delay to allow Lock in to settle
1000

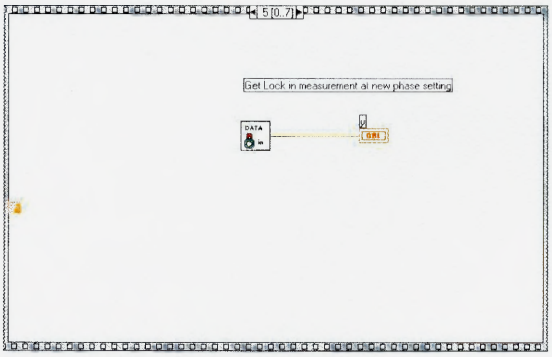
5 [0..7]
Get Lock in measurement at new phase setting
DATA
GBL

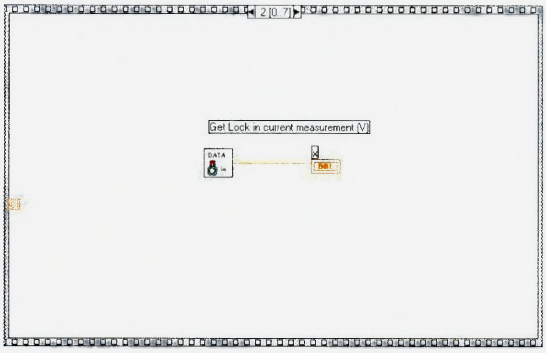
2 [0..7]
Get Lock in current measurement (V)
DATA
GBL

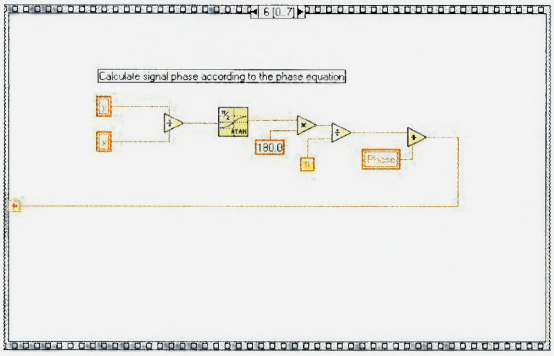
6 [0..7]
Calculate signal phase according to the phase equation
180.0
Phase

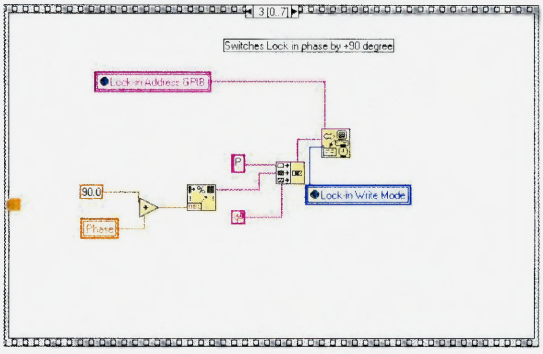
3 [0..7]
Switches Lock in phase by +90 degree
Lock-in Address GPIB
90.0
Phase
Lock-in Write Mode

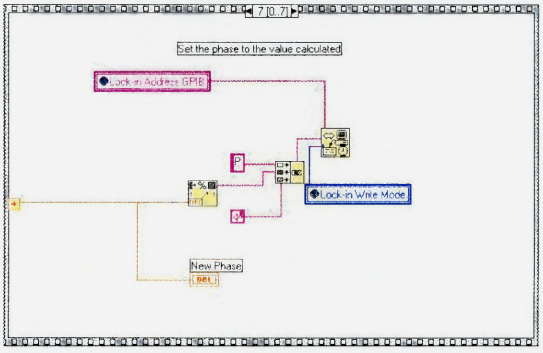
7 [0..7]
Set the phase to the value calculated
Lock-in Address GPIB
Lock-in Write Mode
New Phase
GBL

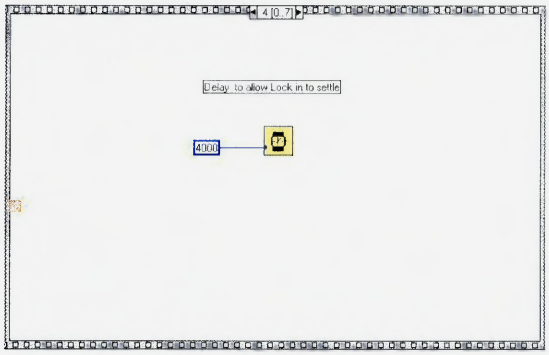
4 [0..7]
Delay to allow Lock in to settle
4000

Lock in phase data.vi

Connector Pane


Front Panel

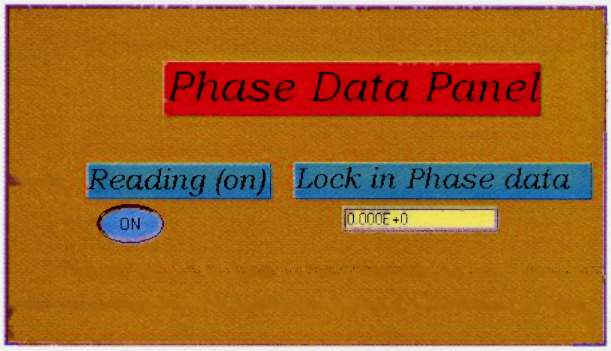


Block Diagram

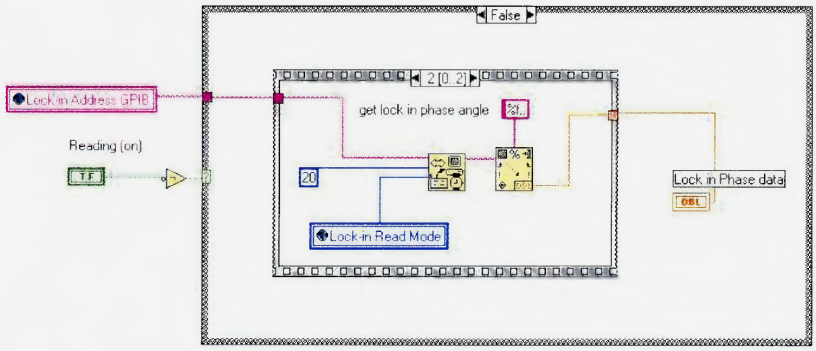


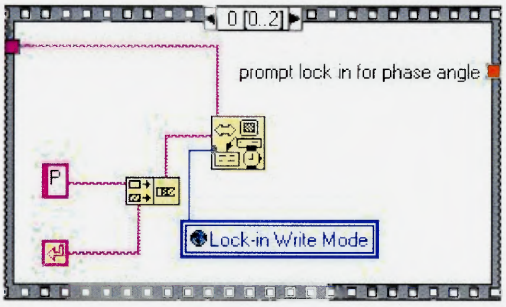

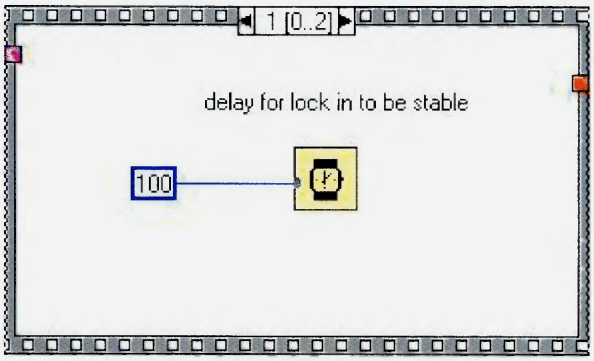



Lock in global variables.vi

Connector Pane


Front Panel

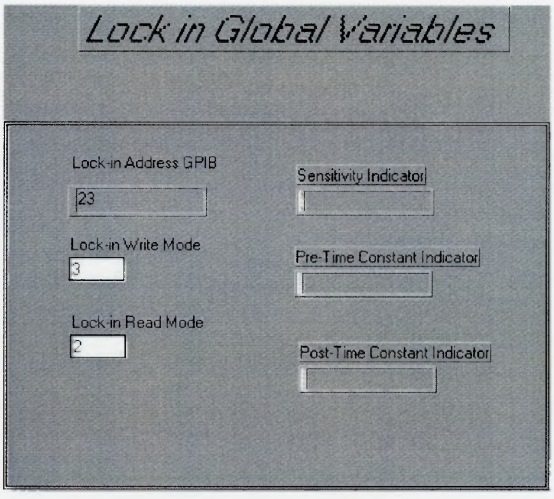

Lock in measurement data.vi

Connector Pane


Front Panel

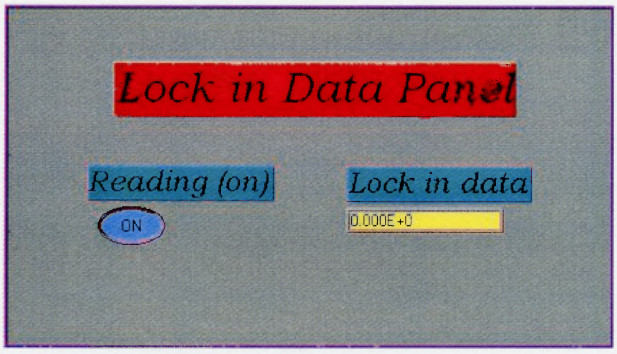


Block Diagram

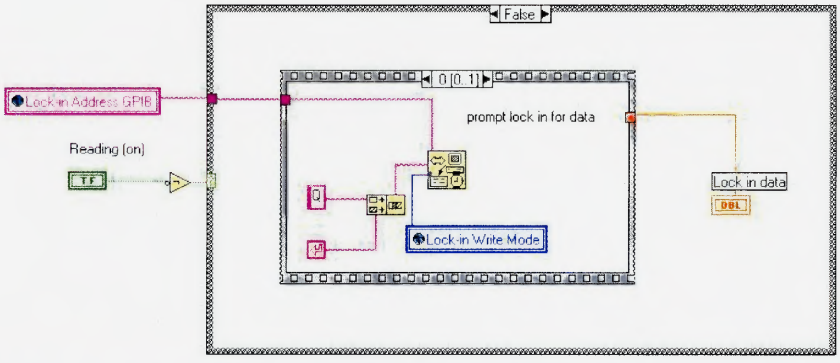


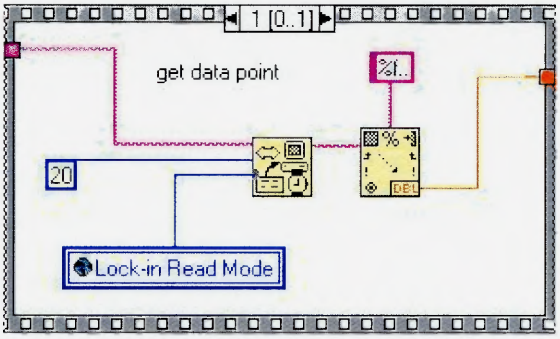

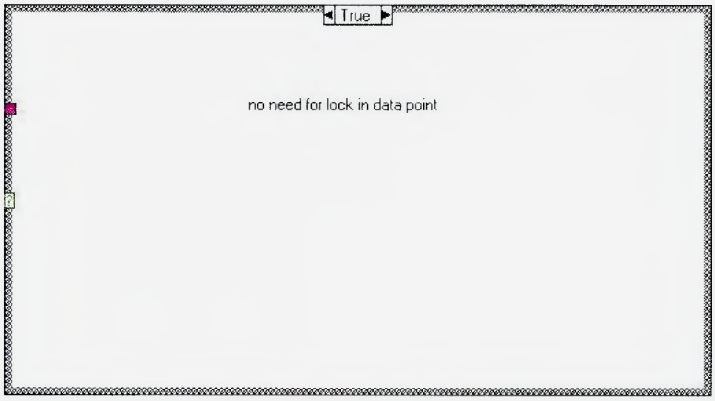


Lock in setting panel.vi

Connector Pane

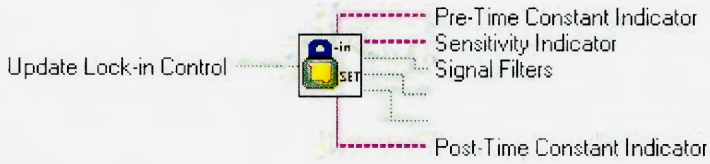


Front Panel

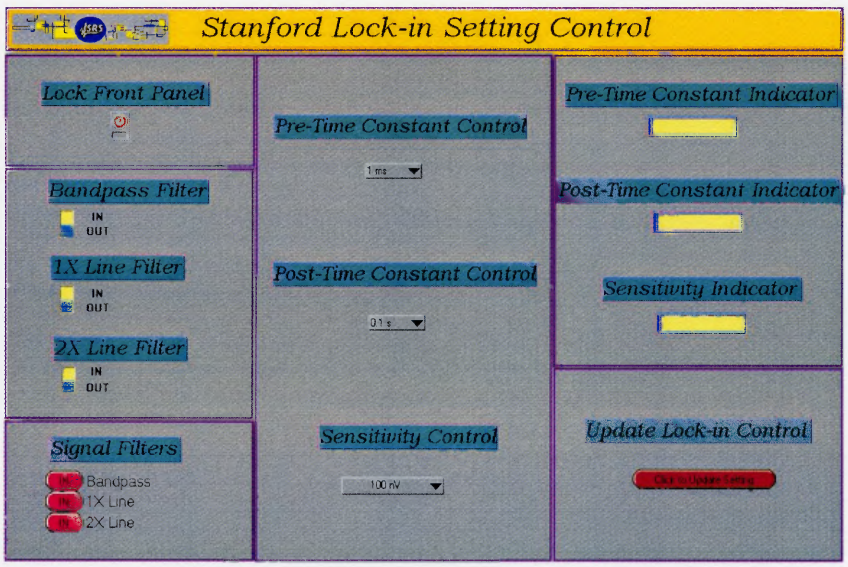

Block Diagram

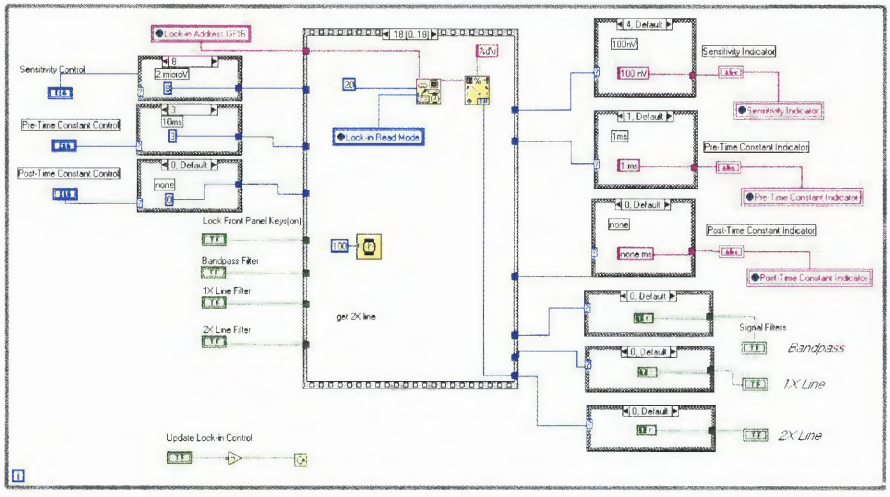


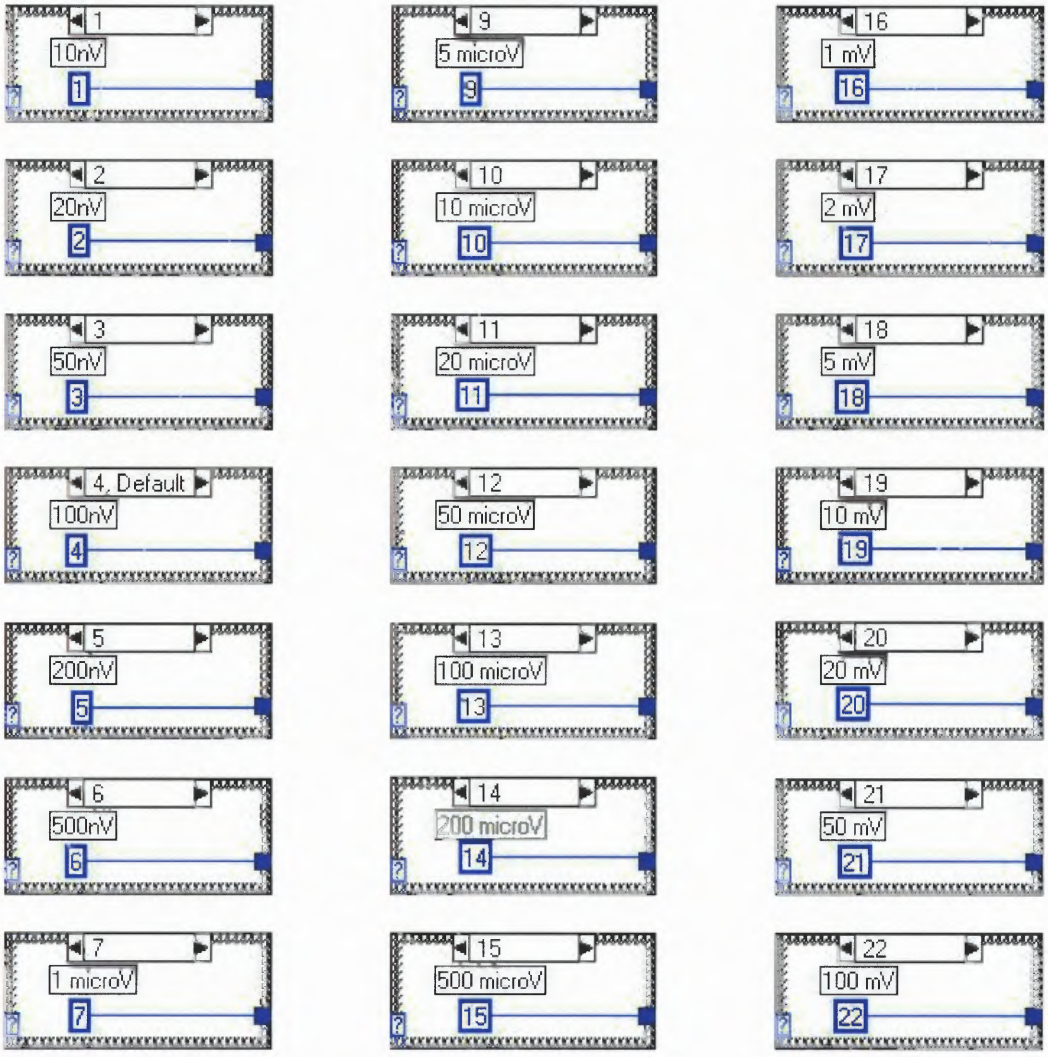

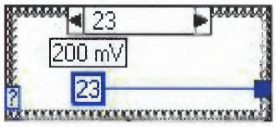
23
200 mV
23

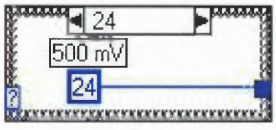
24
500 mV
24

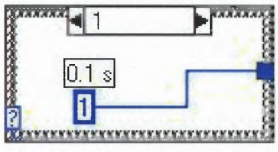
1
0.1 s
1

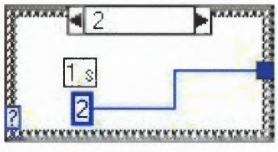
2
1 s
2

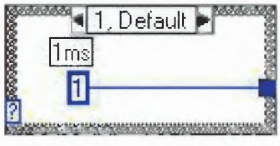
1, Default
1ms
1

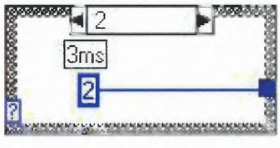
2
3ms
2

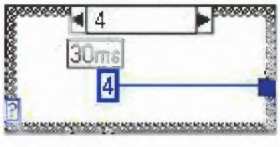
4
30ms
4

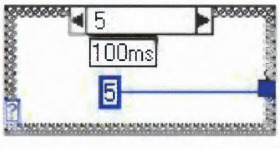
5
100ms
5

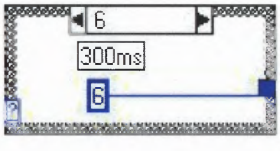
6
300ms
6

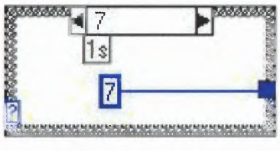
7
1s
7

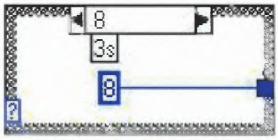
8
3s
8

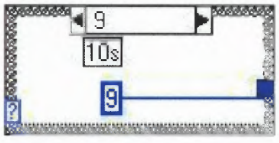
9
10s
9

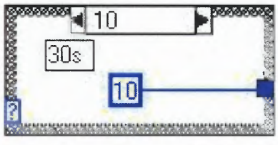
10
30s
10

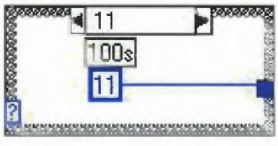
11
100s
11

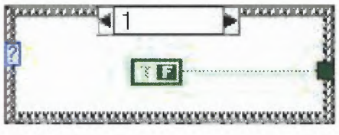
1

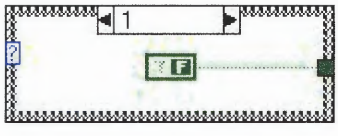
1

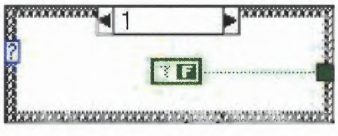
1

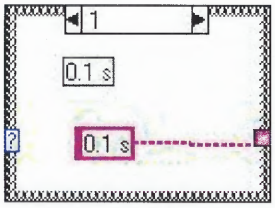
1
0.1 s
0.1 s

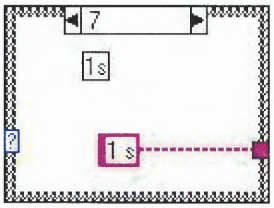
7
1s
1 s

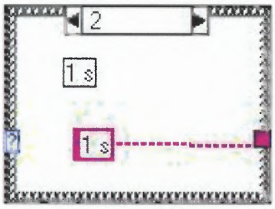
2
1 s
1 s

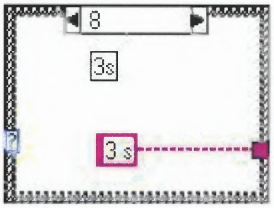
8
3s
3 s

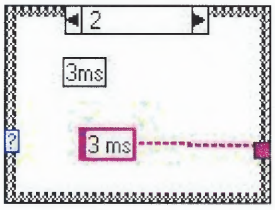
2
3ms
3 ms

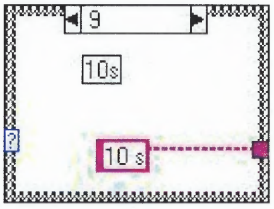
9
10s
10 s

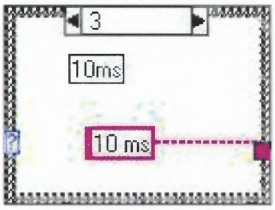
3
10ms
10 ms

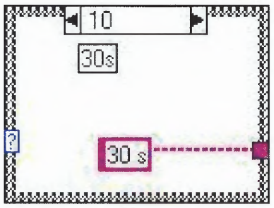
10
30s
30 s

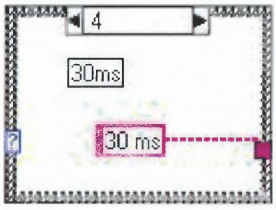
4
30ms
30 ms

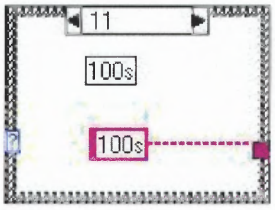
11
100s
100s

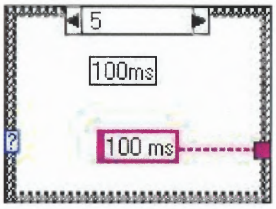
5
100ms
100 ms

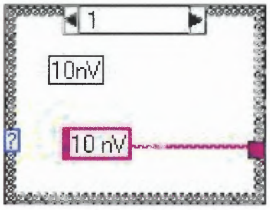
1
10nV
10 nV

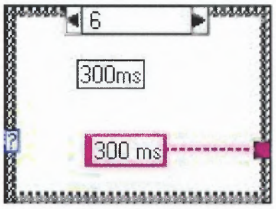
6
300ms
300 ms

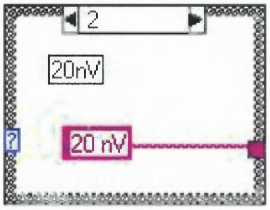
2
20nV
20 nV

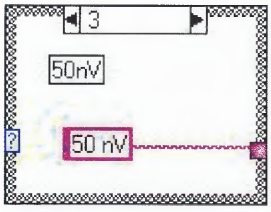
3
50nV
50 nV

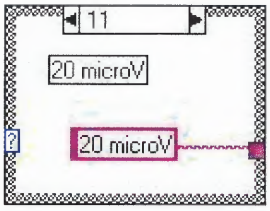
11
20 microV
20 microV

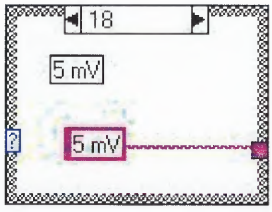
18
5 mV
5 mV

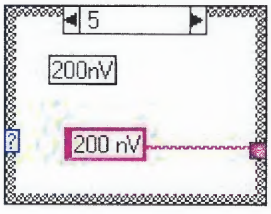
5
200nV
200 nV

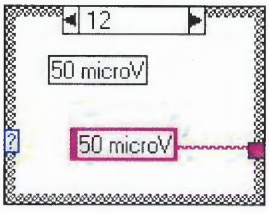
12
50 microV
50 microV

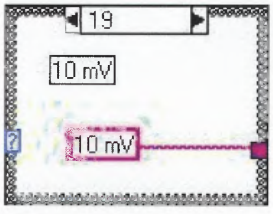
19
10 mV
10 mV

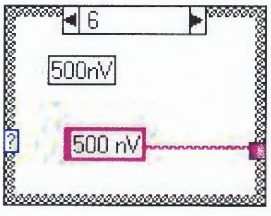
6
500nV
500 nV

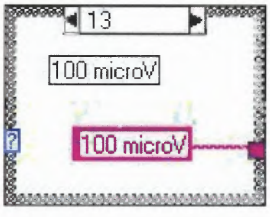
13
100 microV
100 microV

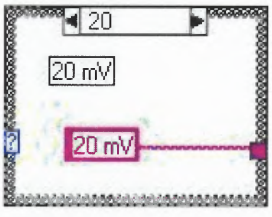
20
20 mV
20 mV

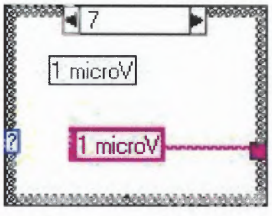
7
1 microV
1 microV

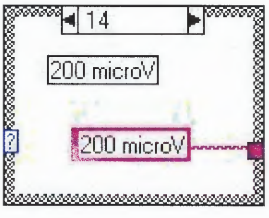
14
200 microV
200 microV

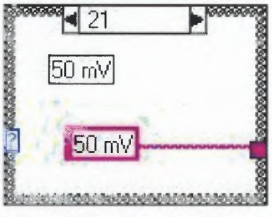
21
50 mV
50 mV

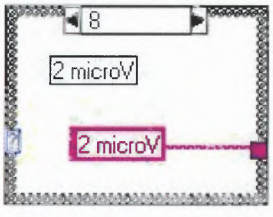
8
2 microV
2 microV

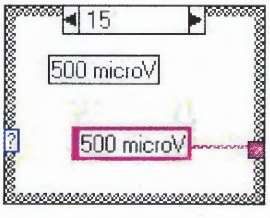
15
500 microV
500 microV

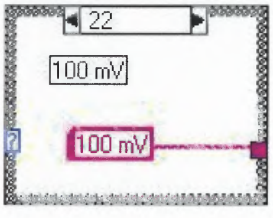
22
100 mV
100 mV

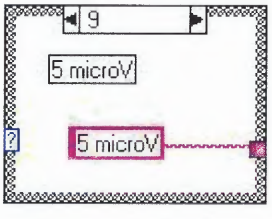
9
5 microV
5 microV

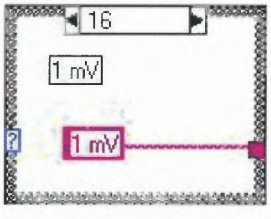
16
1 mV
1 mV

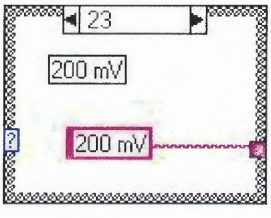
23
200 mV
200 mV

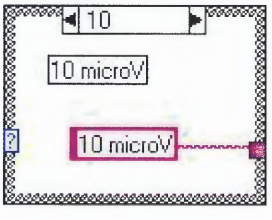
10
10 microV
10 microV

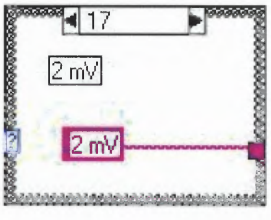
17
2 mV
2 mV

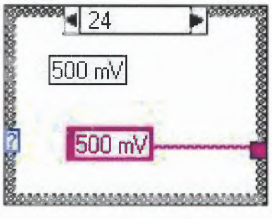
24
500 mV
500 mV

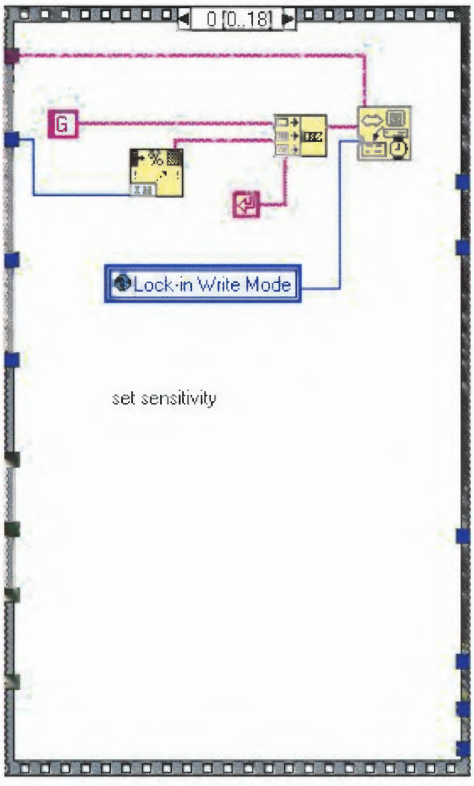
0 [0..18]
G
Lock-in Write Mode
set sensitivity

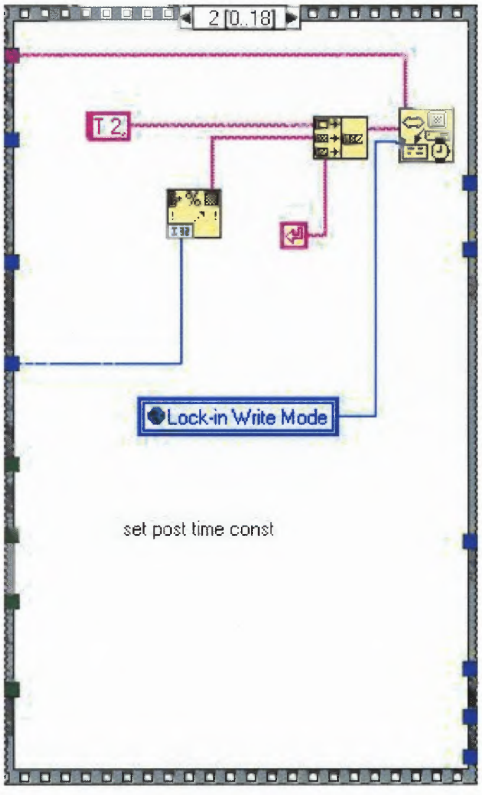
2 [0..18]
T 2
Lock-in Write Mode
set post time const

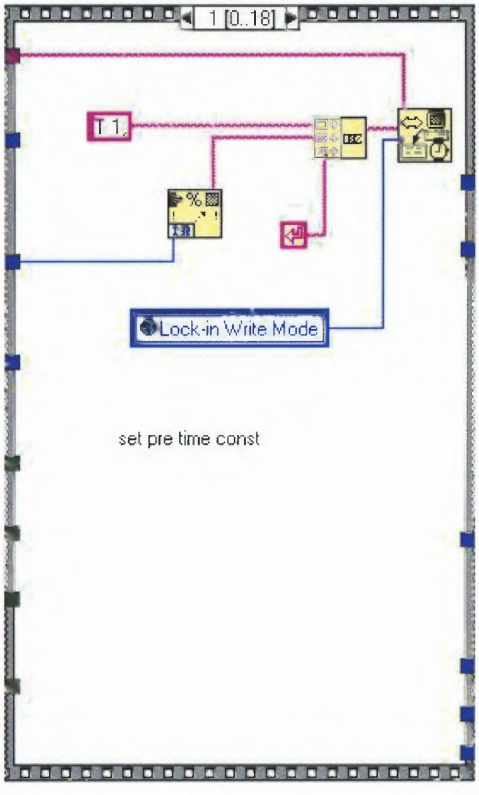
1 [0..18]
T 1
Lock-in Write Mode
set pre time const

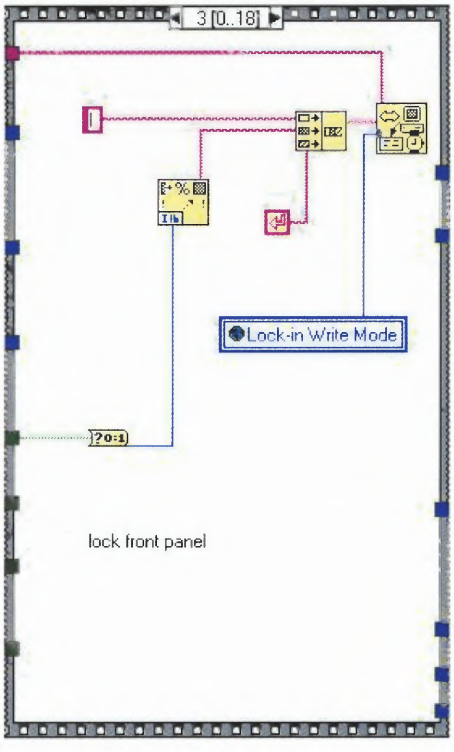
3 [0..18]
I
Lock-in Write Mode
lock front panel

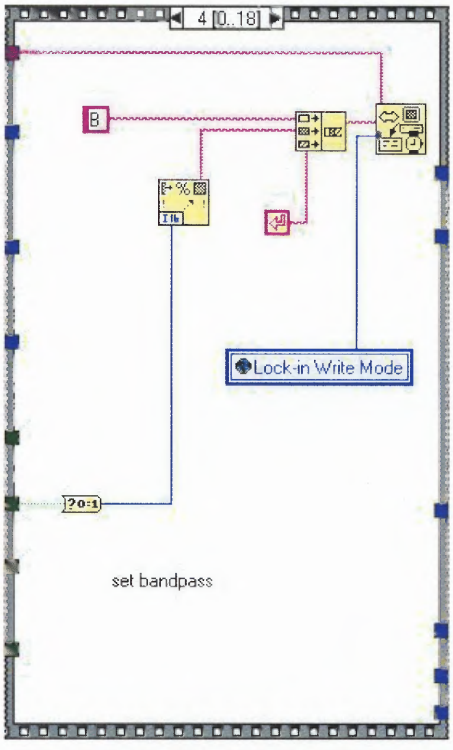
4 [0..18]
B
Lock-in Write Mode
?0:1
set bandpass

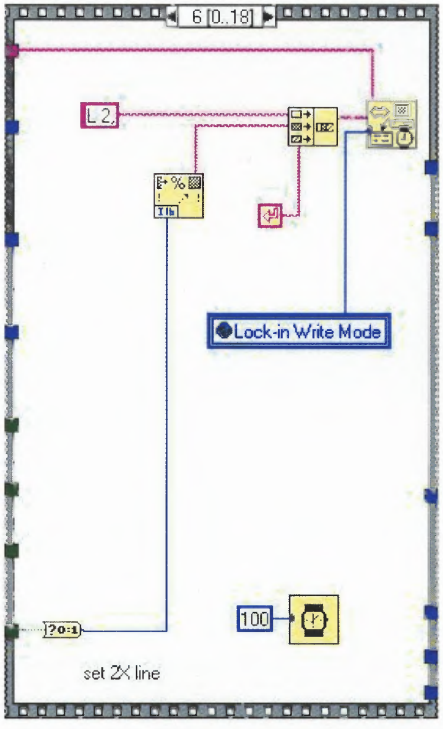
6 [0..18]
L 2.
Lock-in Write Mode
?0:1
100
set 2X line

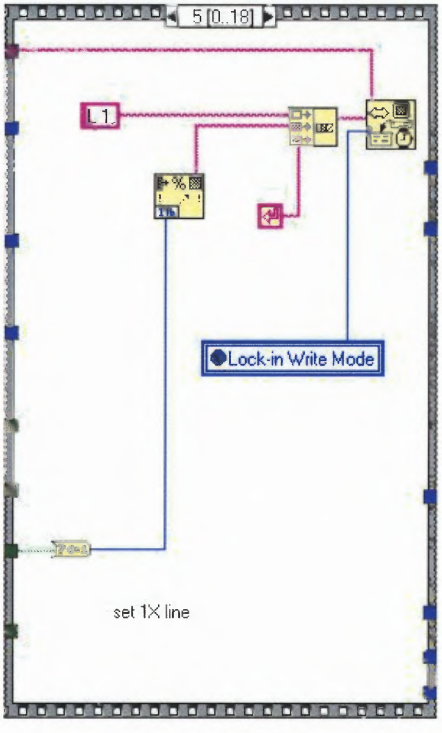
5 [0..18]
L 1.
Lock-in Write Mode
?0:1
set 1X line

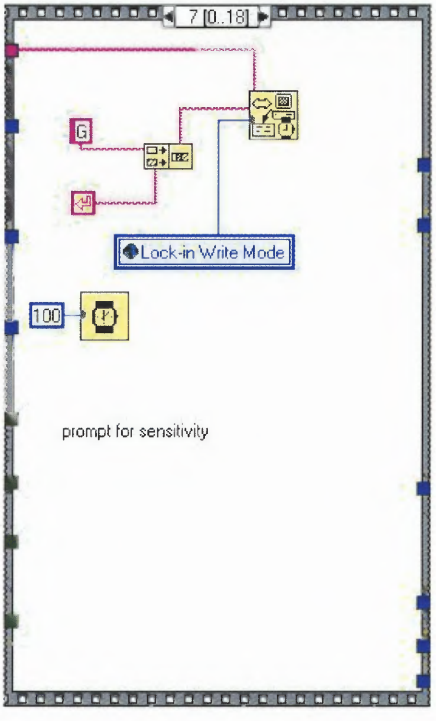
7 [0..18]
G
Lock-in Write Mode
100
prompt for sensitivity

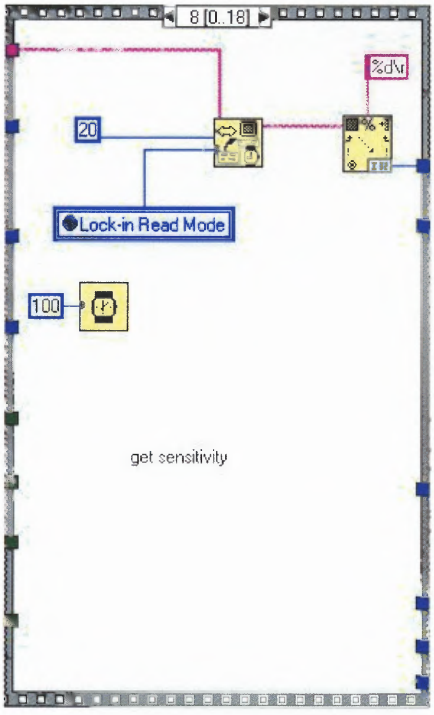
8 [0..18]
%d\r
20
Lock-in Read Mode
100
get sensitivity

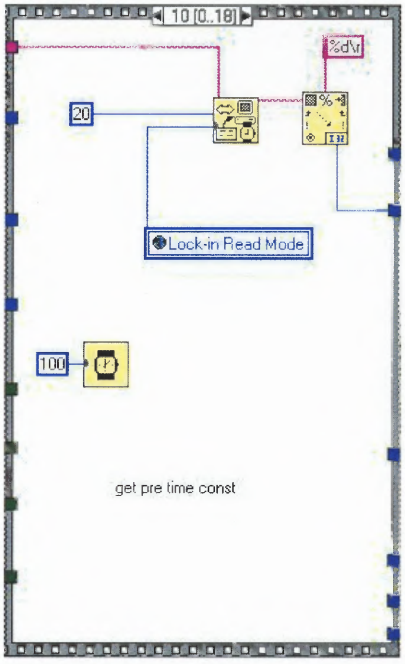
10 [0..18]
%d\r
20
Lock-in Read Mode
100
get pre time const

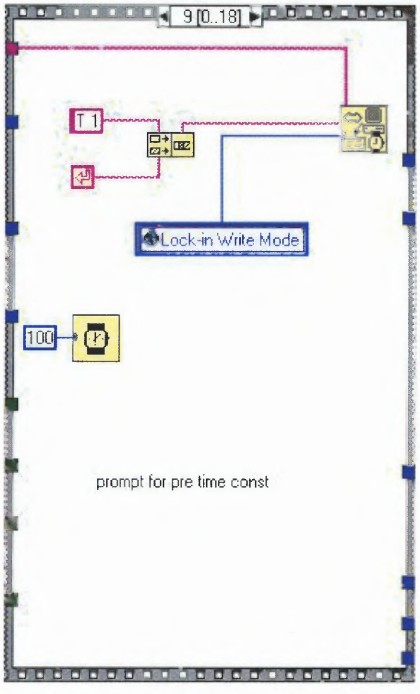
9 [0..18]
T 1
Lock-in Write Mode
100
prompt for pre time const

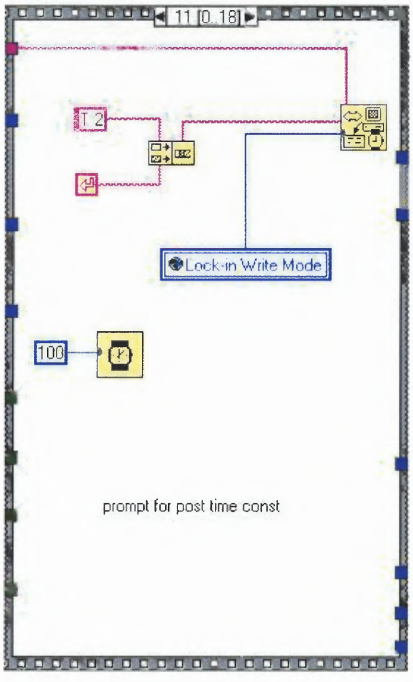
11 [0..18]
T 2
Lock-in Write Mode
100
prompt for post time const

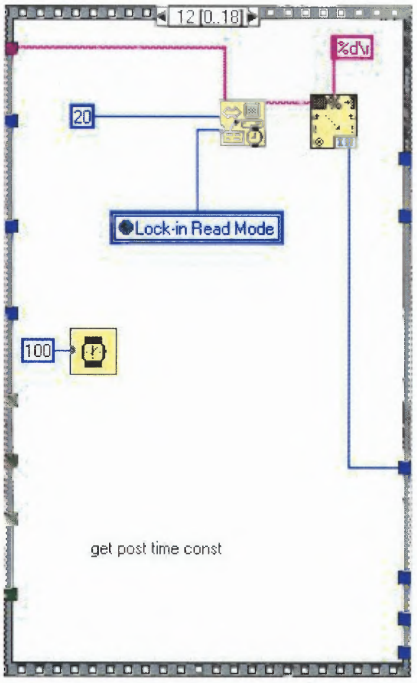
12 [0..18]
%dV
20
Lock-in Read Mode
100
get post time const

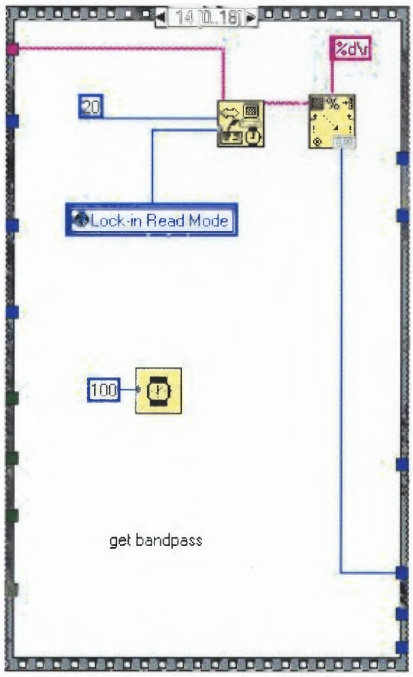
14 [0..18]
%dV
20
Lock-in Read Mode
100
get bandpass

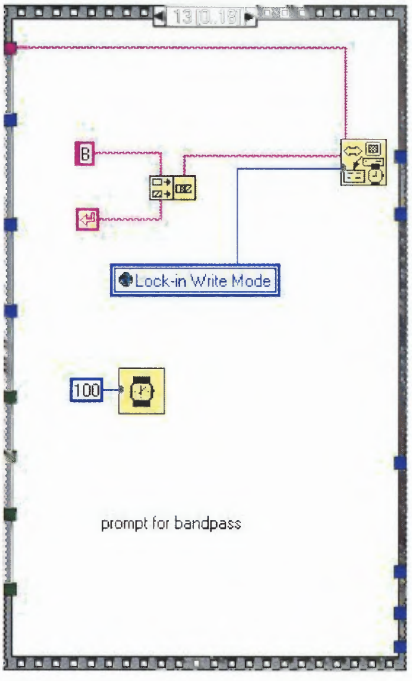
13 [0..18]
B
Lock-in Write Mode
100
prompt for bandpass

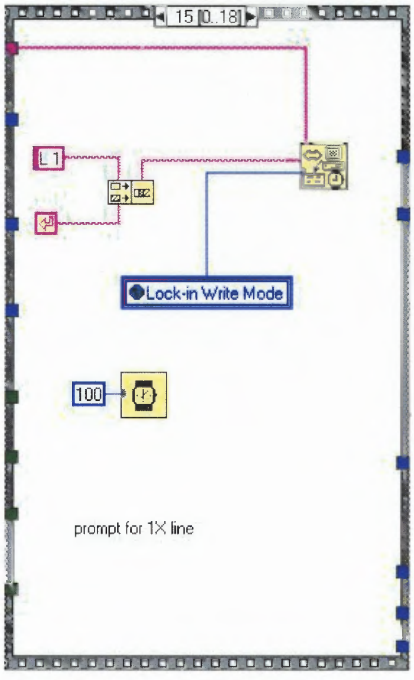
15 [0..18]
L 1
Lock-in Write Mode
100
prompt for 1X line

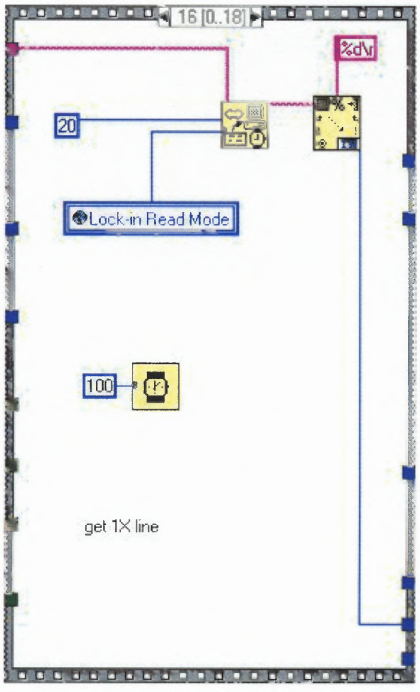
16 [0..18]
%d\r
20
Lock-in Read Mode
100
get 1X line

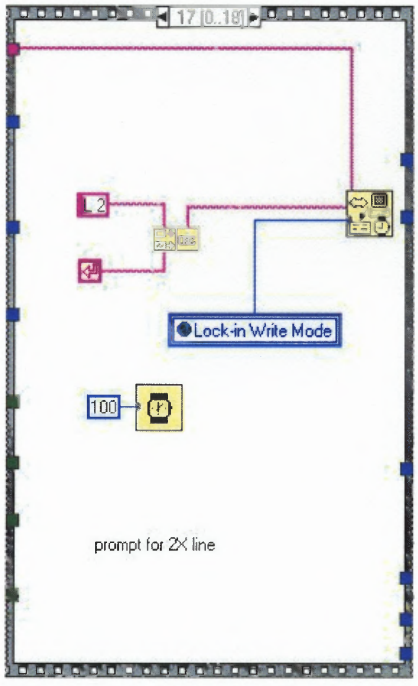
17 [0..18]
L2
Lock-in Write Mode
100
prompt for 2X line

sr510 lockin newport .vi

Front Panel

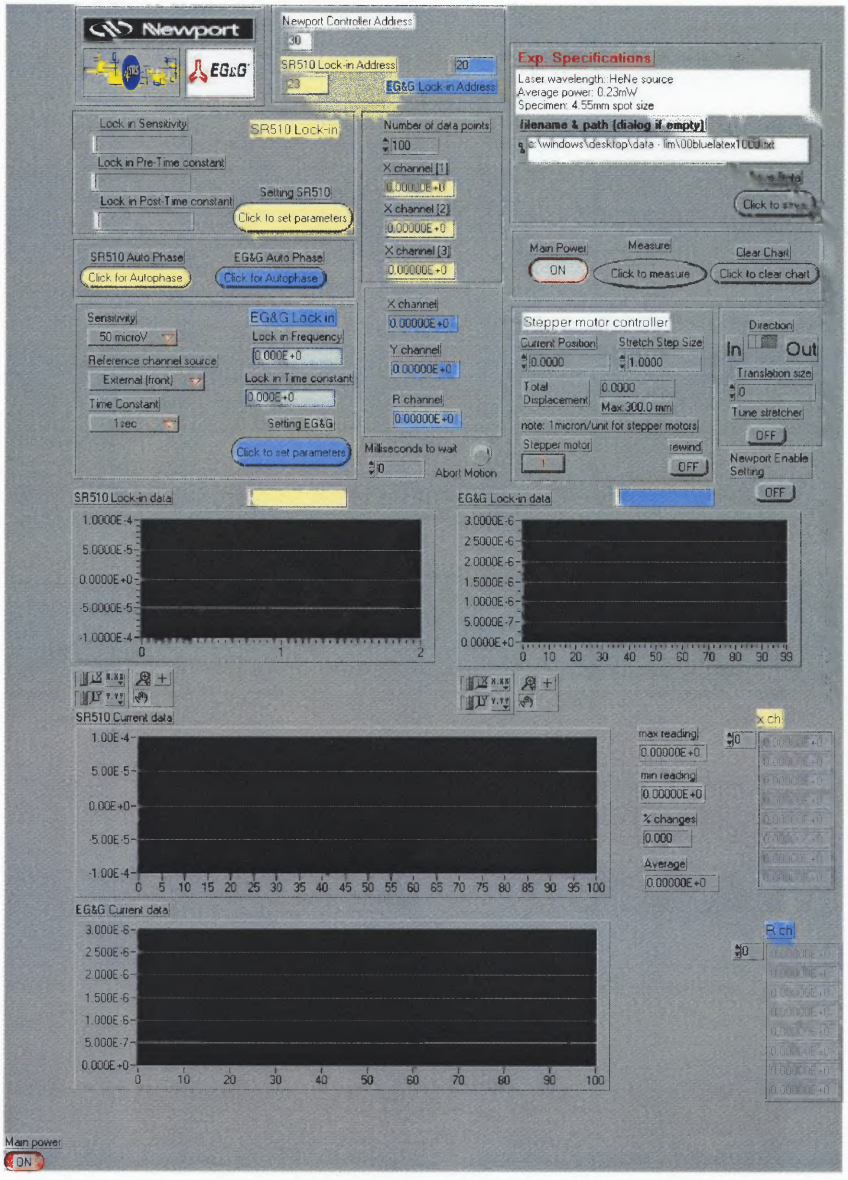


Block Diagram

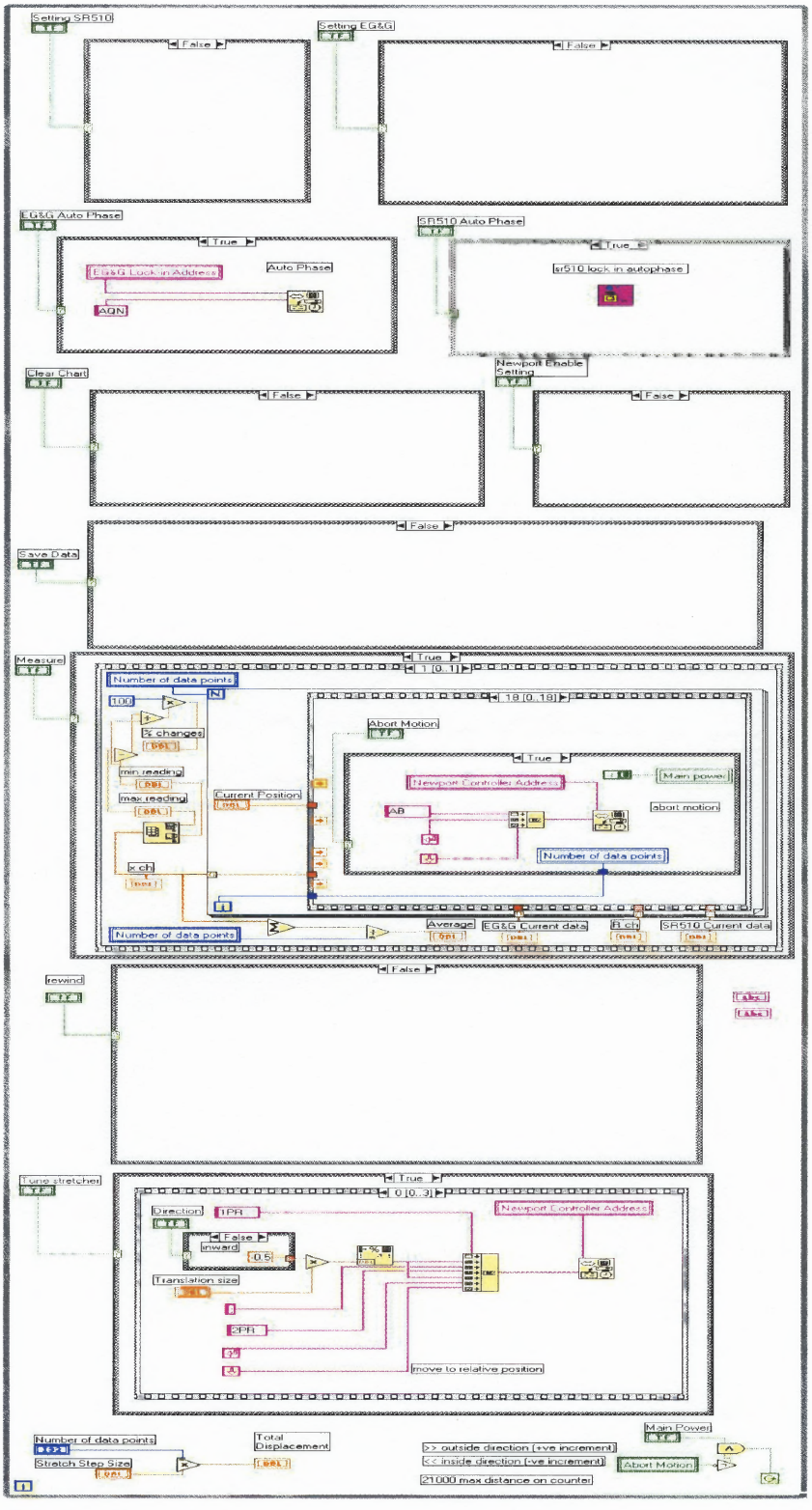
Setting SR510
False
Setting EG&G
False
EG&G Auto Phase
True
EG&G Lock-in Address
Auto Phase
AQN
SR510 Auto Phase
True
sr510 lock in autophase
Clear Chart
False
Newport Enable Setting
False
False
Save Data
Measure
True
1 [0..1]
Number of data points
100
% changes
min reading
max reading
Current Position
18 [0..18]
Abort Motion
True
Newport Controller Address
Main power
abort motion
AB
Number of data points
k ch
Number of data points
Average
EG&G Current data
R ch
SR510 Current data
rewind
False
Tune stretcher
True
0 [0..3]
Direction
1PR
Newport Controller Address
False
inward
0.5
Translation size
2PR
move to relative position
Number of data points
Stretch Step Size
Total Displacement
Main Power
>> outside direction (+ve increment)
<< inside direction (-ve increment)
21000 max distance on counter
Abort Motion

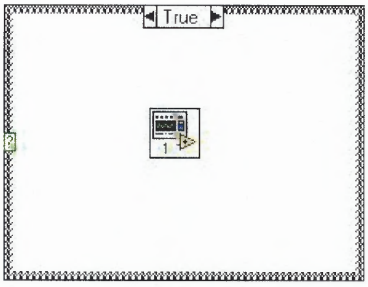
True

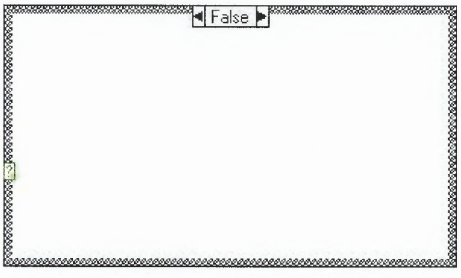
False

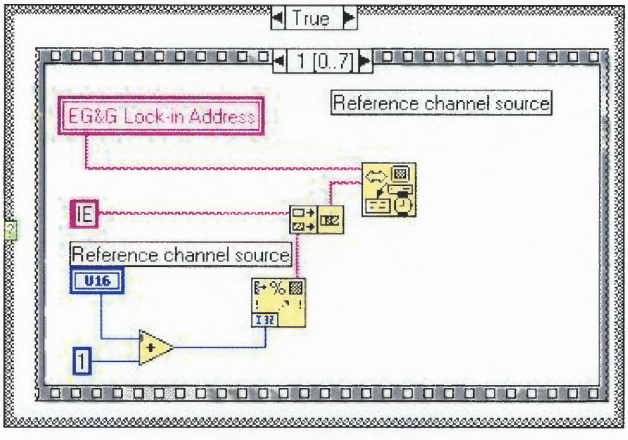
True
1 [0..7]
EG&G Lock-in Address
Reference channel source
IE
Reference channel source
U16
1

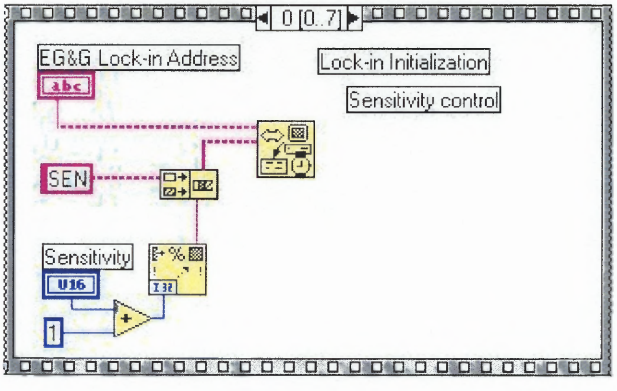
0 [0..7]
EG&G Lock-in Address
abc
Lock-in Initialization
Sensitivity control
SEN
Sensitivity
U16
1

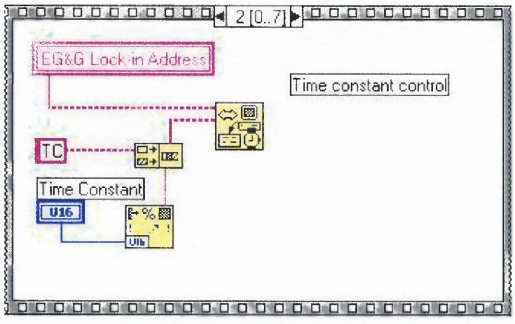
2 [0..7]
EG&G Lock-in Address
Time constant control
TC
Time Constant
U16

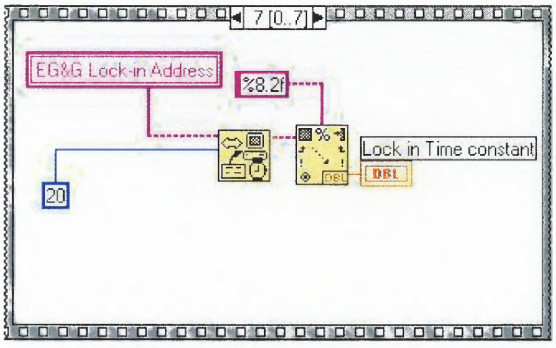
7 [0..7]
EG&G Lock-in Address
%8.2f
Lock in Time constant
DBL
20

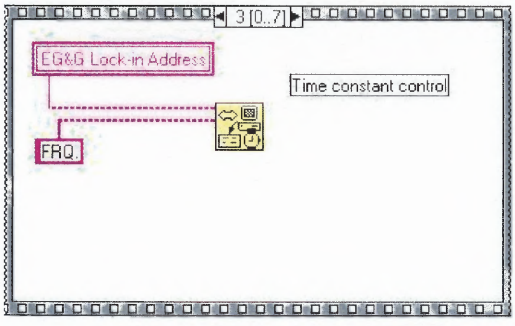
3 [0..7]
EG&G Lock-in Address
Time constant control
FRQ.

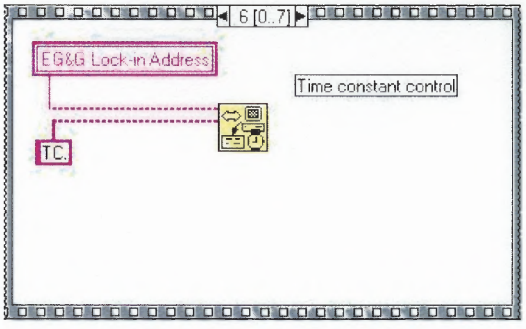
6 [0..7]
EG&G Lock-in Address
Time constant control
TC.

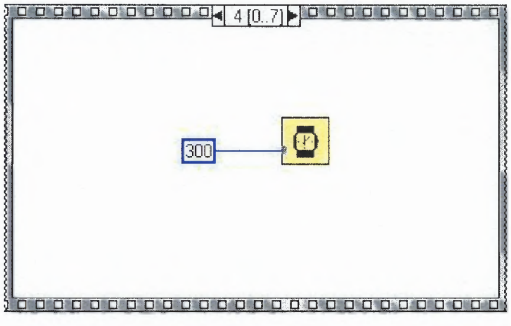
4 [0..7]
300

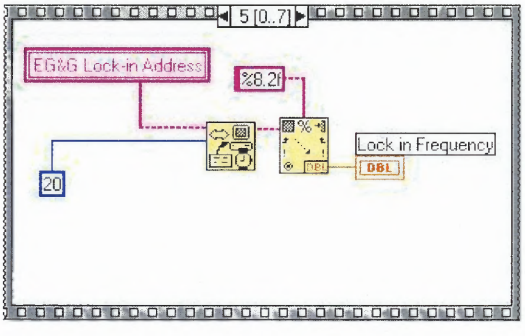
5 [0..7]
EG&G Lock-in Address
%8.2f
Lock in Frequency
DBL
20

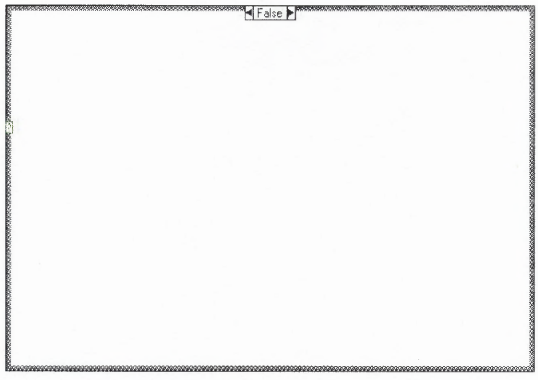
False

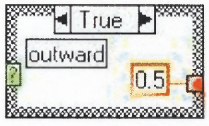
True
outward
0.5

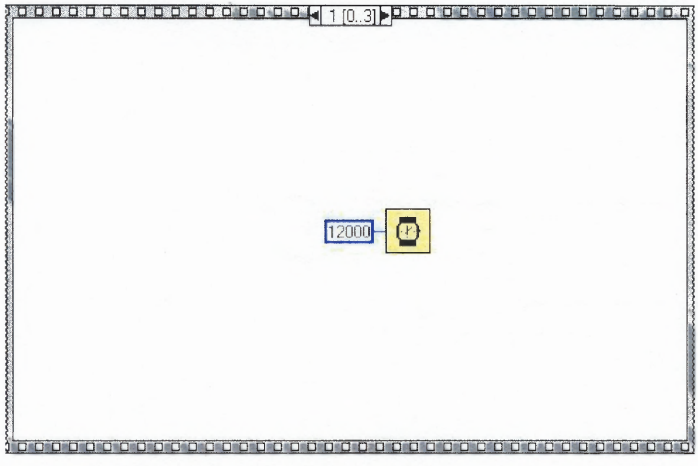
1 [0..3]
12000

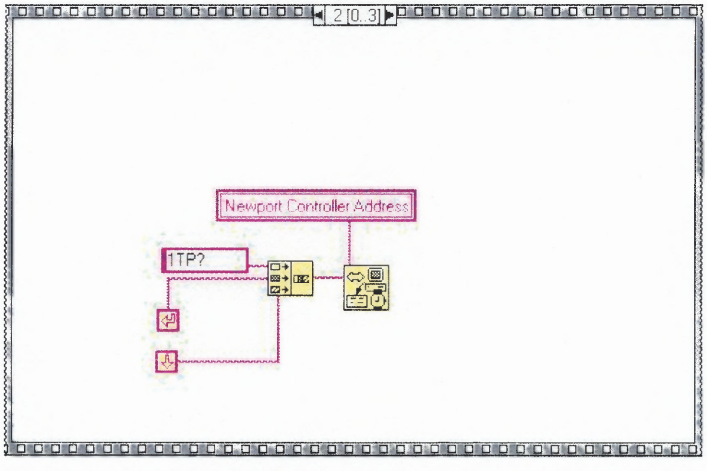
2 [0..3]
Newport Controller Address
1TP?

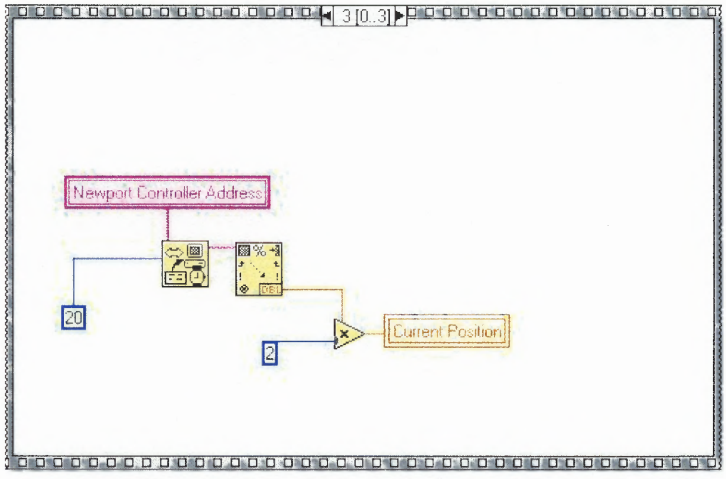
3 [0..3]
Newport Controller Address
20
2
Current Position

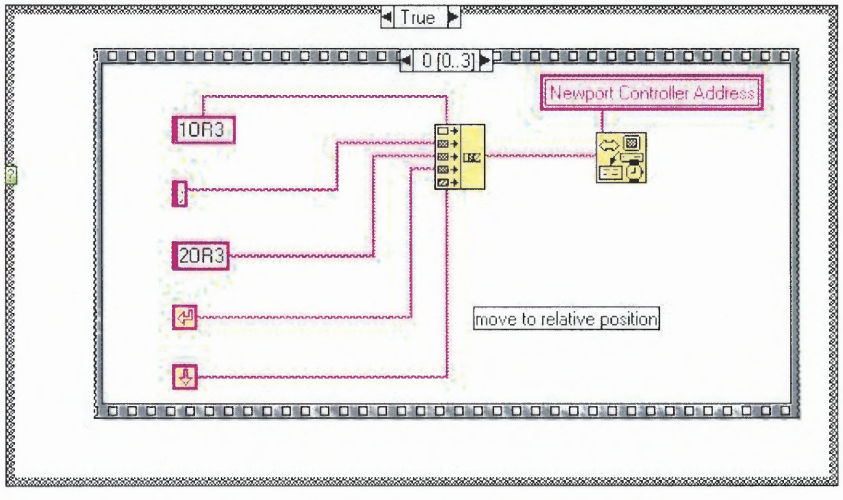
True
0 [0..3]
Newport Controller Address
10R3
20R3
move to relative position

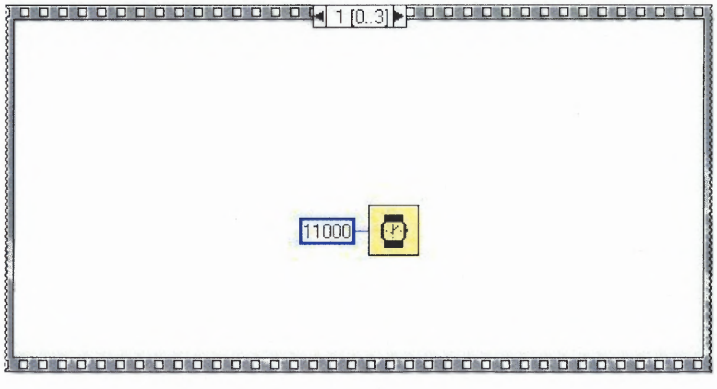
1 [0..3]
11000

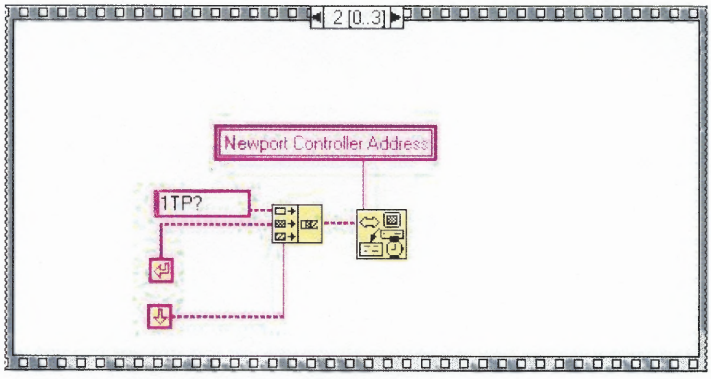
2 [0..3]
Newport Controller Address
1TP?

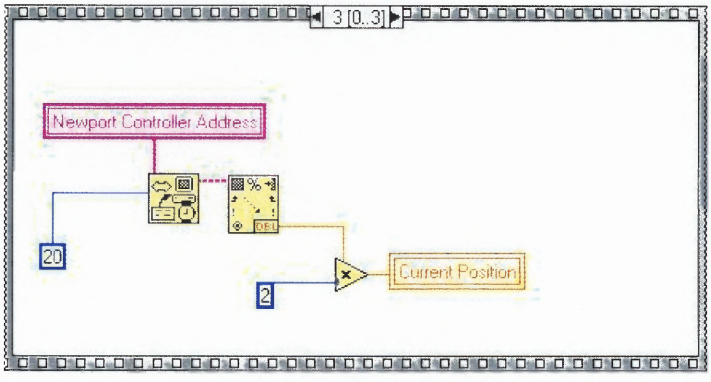
3 [0..3]
Newport Controller Address
20
2
Current Position

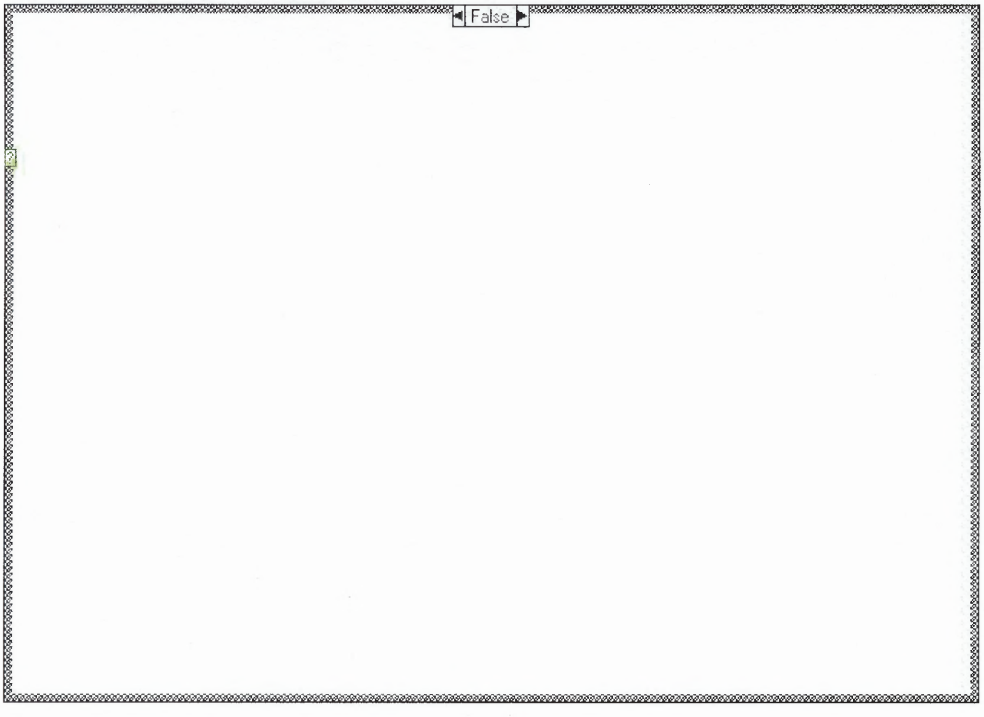
False

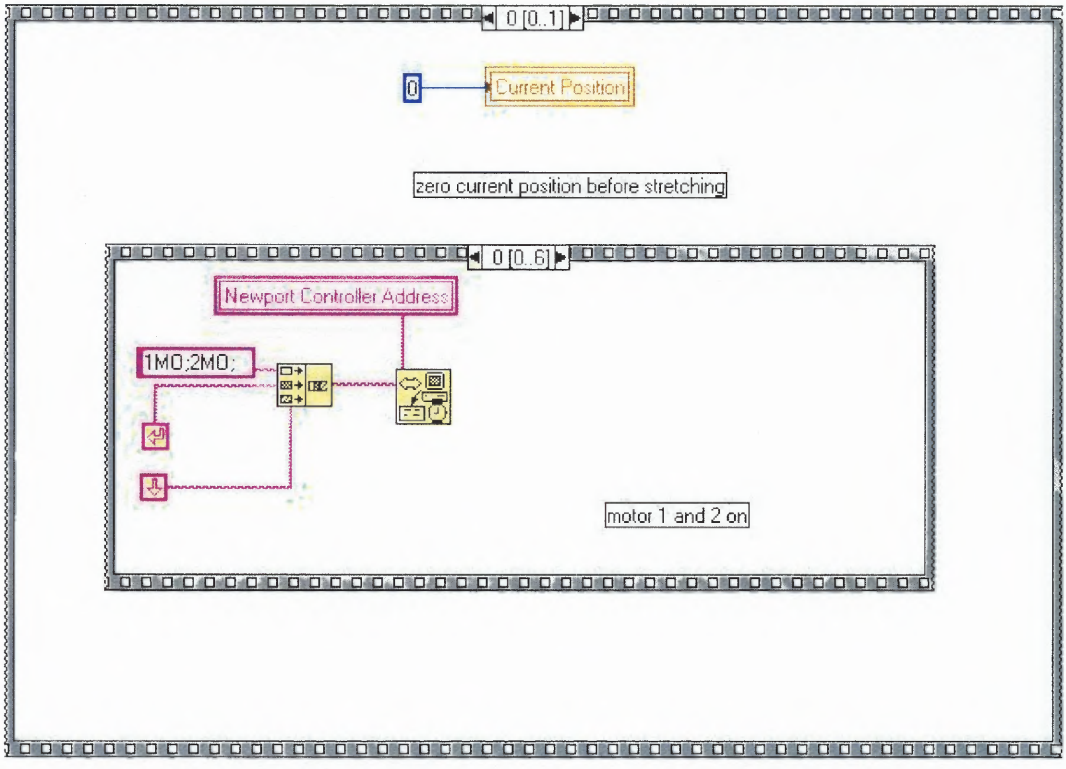
0 [0..1]
0
Current Position
zero current position before stretching
0 [0..6]
Newport Controller Address
1MO;2MO;
motor 1 and 2 on

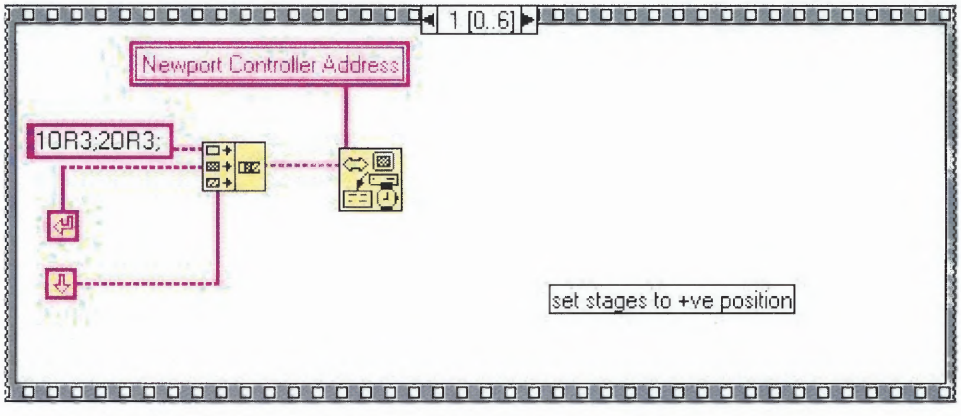
1 [0..6]
Newport Controller Address
1OR3;2OR3;
set stages to +ve position

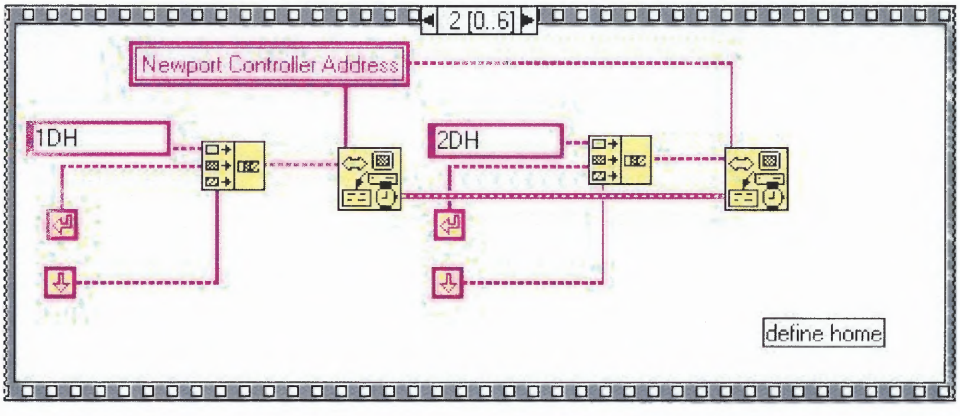
2 [0..6]
Newport Controller Address
1DH
2DH
define home

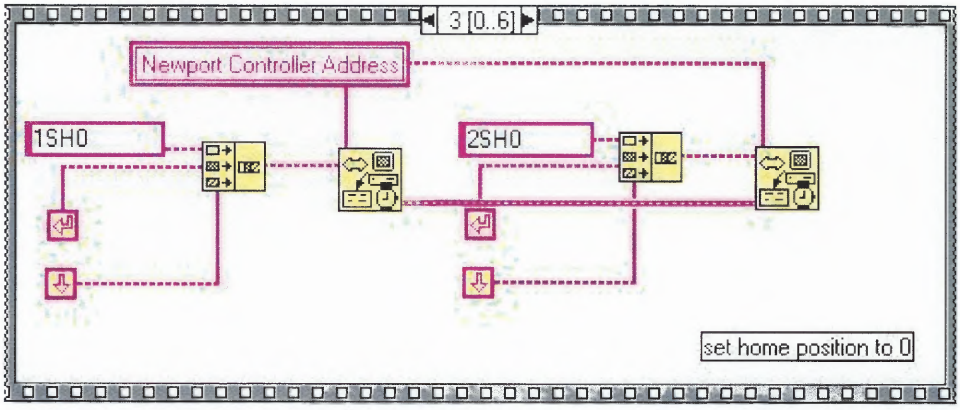
3 [0..6]
Newport Controller Address
1SH0
2SH0
set home position to 0

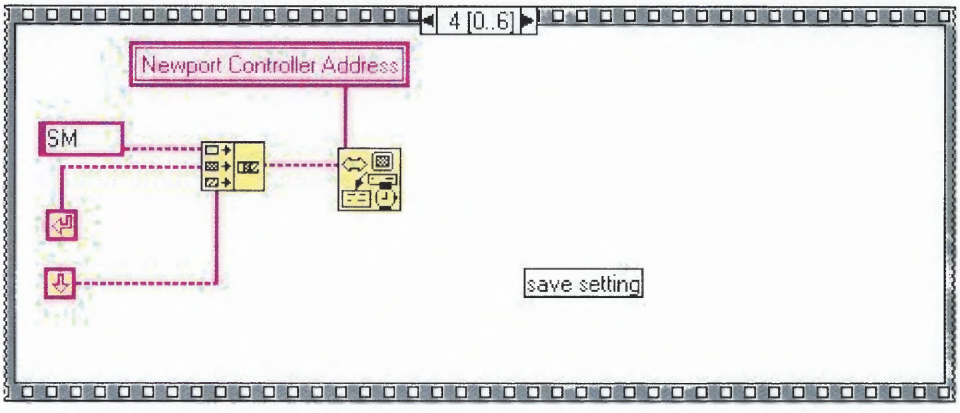
4 [0..6]
Newport Controller Address
SM
save setting

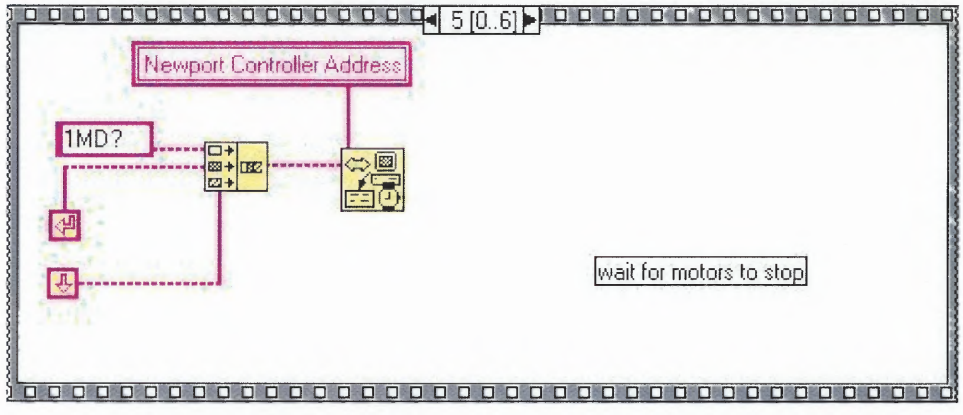
5 [0..6]
Newport Controller Address
1MD?
wait for motors to stop

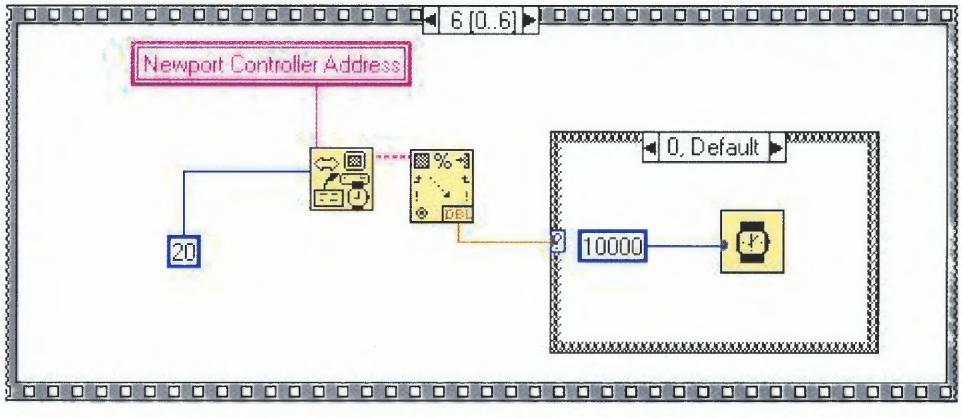
6 [0..6]
Newport Controller Address
0, Default
20
10000

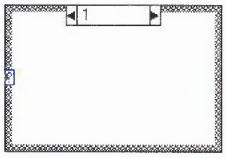
1

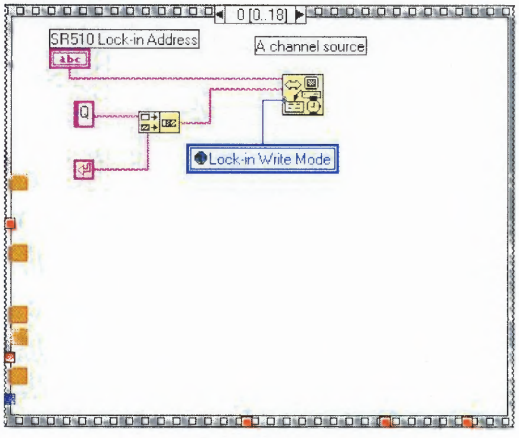
0 [0..18]
SR510 Lock-in Address
A channel source
Q
Lock-in Write Mode

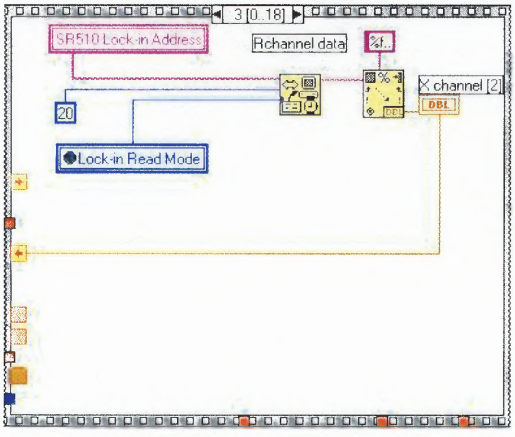
3 [0..18]
SR510 Lock-in Address
Rchannel data
%f..
X channel [2]
DBL
20
Lock-in Read Mode

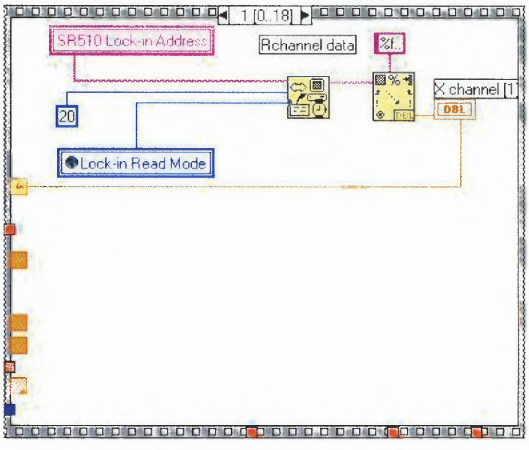
1 [0..18]
SR510 Lock-in Address
Rchannel data
%f..
X channel [1]
DBL
20
Lock-in Read Mode

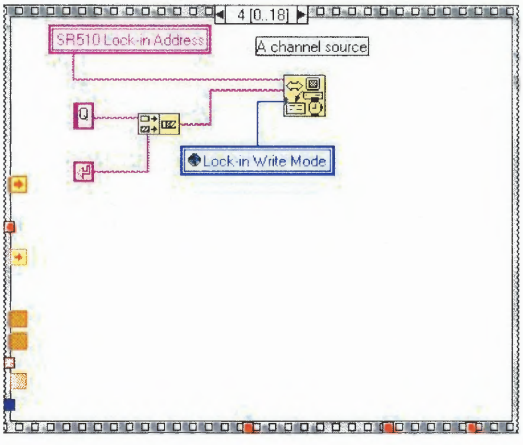
4 [0..18]
SR510 Lock-in Address
A channel source
Q
Lock-in Write Mode

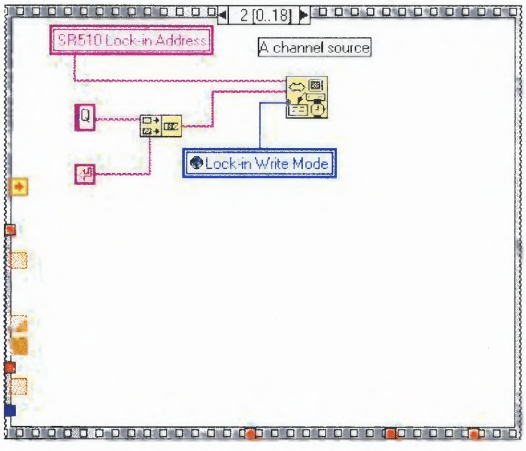
2 [0..18]
SR510 Lock-in Address
A channel source
Q
Lock-in Write Mode

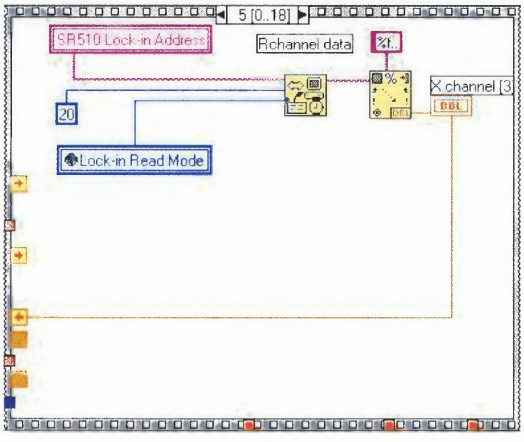
5 [0..18]
SR510 Lock-in Address
Rchannel data
%f..
X channel [3]
DBL
20
Lock-in Read Mode

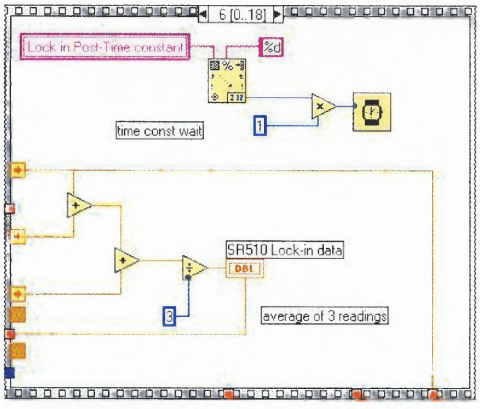
6 [0..18]
Lock in Post-Time constant
%d
time const wait
1
SR510 Lock-in data
DBL
3
average of 3 readings

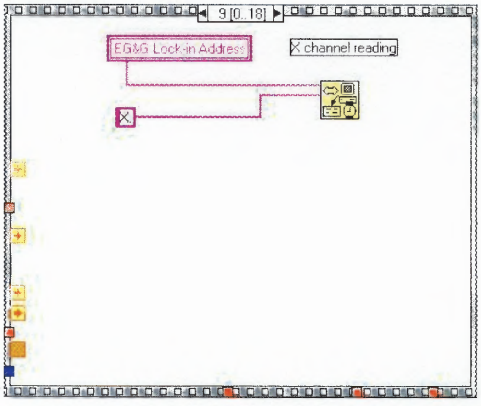
9 [0..18]
EG&G Lock-in Address
X channel reading
X

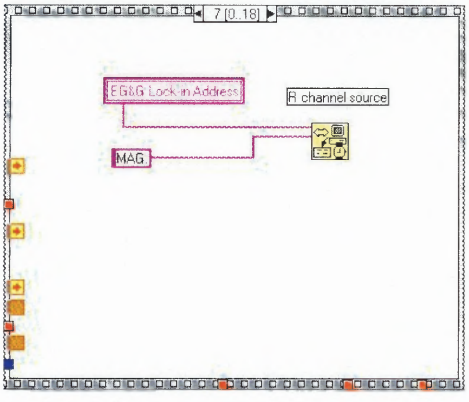
7 [0..18]
EG&G Lock-in Address
R channel source
MAG

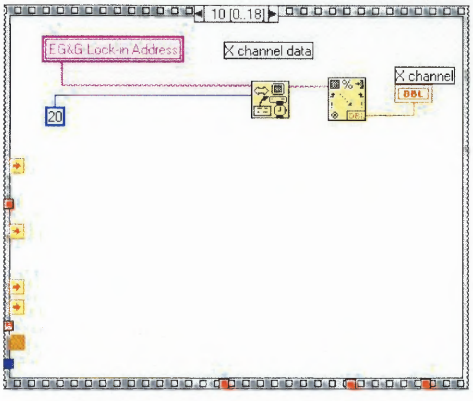
10 [0..18]
EG&G Lock-in Address
X channel data
X channel
DBL
20

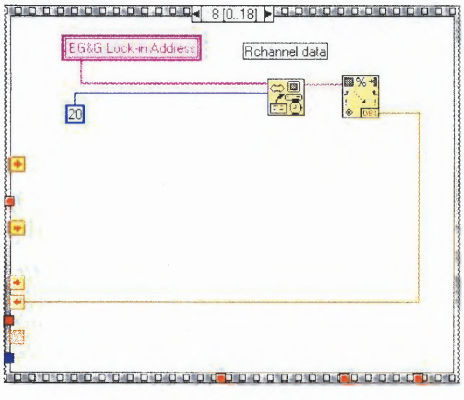
8 [0..18]
EG&G Lock-in Address
Rchannel data
20

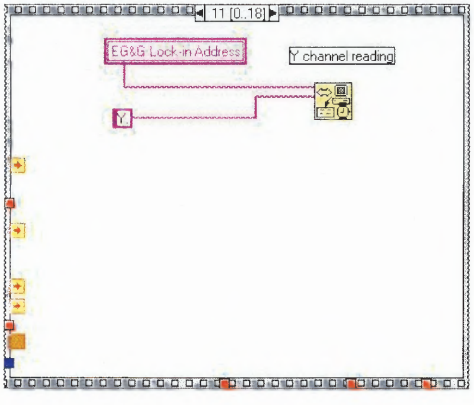
11 [0..18]
EG&G Lock-in Address
Y channel reading
Y

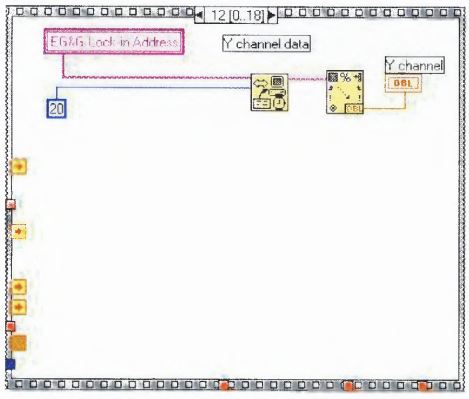
12 [0..18]
EG&G Lock-in Address
Y channel data
Y channel
DBL
20

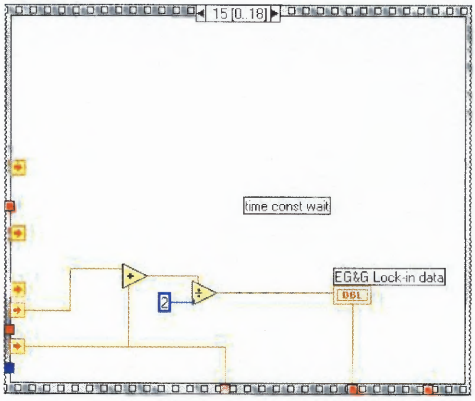
15 [0..18]
time const wait
EG&G Lock-in data
DBL
2

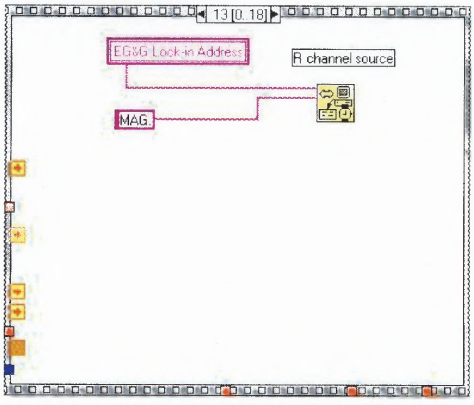
13 [0..18]
EG&G Lock-in Address
R channel source
MAG

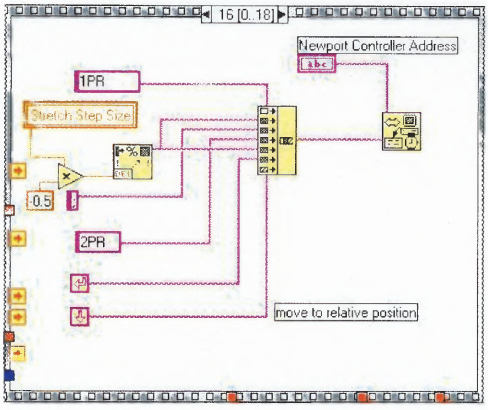
16 [0..18]
Newport Controller Address
1PR
Stretch Step Size
0.5
2PR
move to relative position

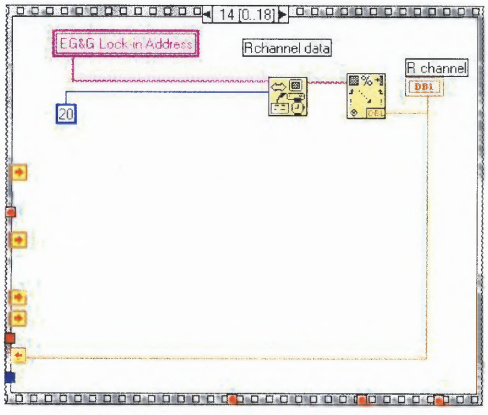
14 [0..18]
EG&G Lock-in Address
Rchannel data
R channel
DBL
20

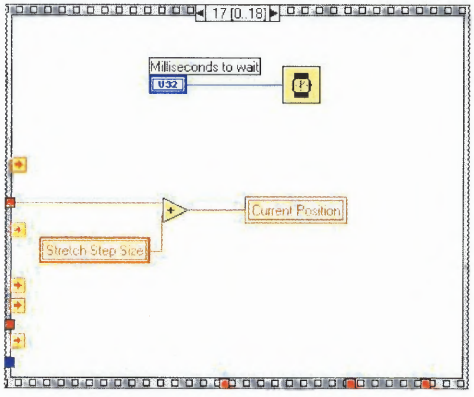
17 [0..18]
Milliseconds to wait
U32
Current Position
Stretch Step Size

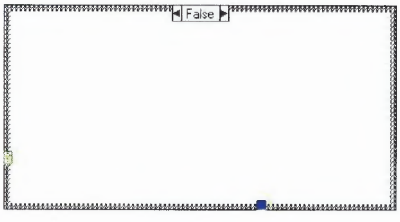
False

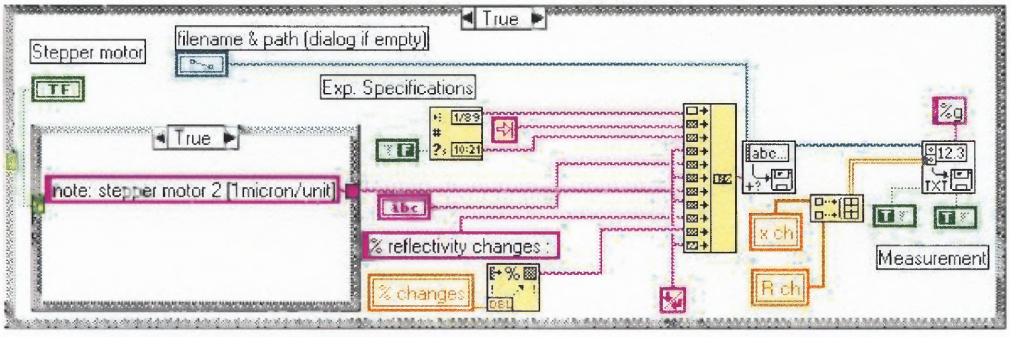
True
Stepper motor
filename & path (dialog if empty)
TF
Exp. Specifications
True
note: stepper motor 2 [1micron/unit]
% reflectivity changes :
% changes
x ch
R ch
Measurement

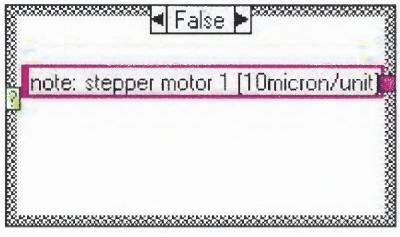
False
note: stepper motor 1 [10micron/unit]

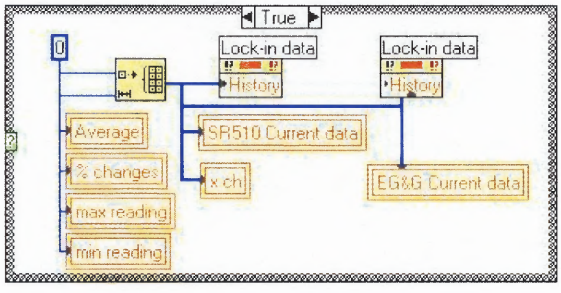
True
0
Lock-in data
History
Lock-in data
History
Average
% changes
max reading
min reading
SR510 Current data
x ch
EG&G Current data

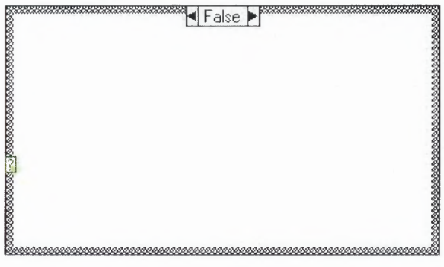
False

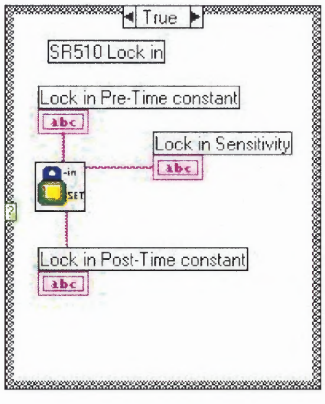
True
SR510 Lock in
Lock in Pre-Time constant
Lock in Sensitivity
Lock in Post-Time constant

## BIBLIOGRAPHY


[1] A. J. Welch, and M. J. C. van Gemert, "Optical-Thermal Response of Laser-Irradiated Tissue", Plenum, New York, 1995.

[2] J. F. Federici, N. Guzelsu, H. C. Lim, G. Jannuzzi, T. Findley, H. R. Chaudhry, and A. B. Ritter, "Non-invasive Light Reflection Technique for Measuring Soft-Tissue Stretch", *Appl. Optics* **38**, 6653-6660 (1999).

[3] S. G. Demos, and R. R. Alfano, "Optical Polarization Imaging", *Appl. Optics* **36**, 150-155 (1997).

[4] R. R. Anderson, "Polarized Light Examination and Photography of the Skin", *Archives of Dermatology* **127**, 1000- 1005 (1991).

[5] E. Fariza, T. O'Day, A. E. Jalkh and A. Medina, "Use of Cross-Polarized Light in Anterior Segment Photography," *Archives of Ophthalmology* **107**, 608-610, (1989).

[6] J. Philp, N. J. Carter and C. P. Lenn, "Improved Optical Discrimination of skin with polarized Light," *Journal of Society of Cosmetic Chemistry* **39**, 121-132, (1988).

[7] S. L. Jacques, J. R. Roman and K. Lee, "Imaging Superficial Tissues with Polarized Light", *Lasers in Surgery and Medicine* **26**, 119-129, (2000).

[8] M. B. Ostermeyer, D. V. Stephensen, L. Wang L and S. L. Jacques, "Nearfield Polarization Effects on Light Propagation in Random Media", Sevick-Muraca E, Benaron D, ed., OSA TOPS on biomedical optical spectroscopy and diagnostics, Vol. **3**, 20-25, Washington DC: Optical Society of America (1996).

[9] S. C. Yin, W. R. Tomkins, K. L. Petterson, and M. Intaglietta, "A Video Dimension Analyzer", *IEEE Trans. Biomed. Eng.* **19**, 376- 385 (1972).

[10] W. P. Smutz, M. Drexler, L. J. Berglund, E. Growney, and K. N. An, "Accuracy of a Video Strain Measurement System", *J. Biomechanics* **29**, 813-817 (1996).

[11] J. D. Humphrey, "Mechanics of the Arterial Wall: Review and Directions", *Crit. Rev. Biomed. Eng.* **23**, 1-162 (1995).

[12] R. R. Anderson and J. A. Parish, "Optical Properties of Human Skin," in *The Science of Photomedicine*, J. D. Regan and J. A. Parrish, ed. Plenum, New York, 1982, pp. 147–194.

[13] J. B. Dawson, D. J. Barker, D. J. Ellis, E. Grassam, J. A. Cotterill, G. W. Fisher, and J. W. Feather, "A Theoretical and Experimental Study of Light Absorption and Scattering by In-vivo Skin", *Phys. Med. Biol.* **25**, 695-709 (1980).

[14] J. C. M. Van Gemert, S. L. Jacques, H. J. C. M. Sterenborg, and W. M. Star, "Skin Optics", *IEEE Transac. Biomed. Engng.* **36**, 1146-1154 (1989).

[15] P. H. Andersen, and P. Bjerring, "Spectral Reflectance of Human Skin in vivo", *Photodermatol. Photoimmunol. Photomed.* **7**, 5-12 (1990).

[16] P. H. Andersen, and P. Bjerring, "Noninvasive Computerized Analysis of Skin Chromophores in vivo by Reflectance Spectroscopy", *Photodermatol. Photoimmunol. Photomed.* **7**, 249-257 (1990).

[17] W. F. Cheong, S. A. Prahl, and A. J. Welch, "A Review of the Optical Properties of Biological Tissues", *IEEE J. Quantum Electro.* **26**, 2166-2185 (1990).

[18] B. C. Wilson, and S. L. Jacques, "Optical Reflectance and Transmittance of Tissues: Principles and Applications", *IEEE J. Quant. Electron.* **26,** 2186-2199 (1990).

[19] S. L. Jacques, "The Role of skin Optics Diagnostic and Therapeutic Uses of Lasers", in *"Lasers in Dermatolgy"* ed. by R. Steiner, R. Kaufmann, M. Landthaler, and O. Braun-Falco, Springer-Verlag , Berlin, 1991, pp 1-21.

[20] H. Zeng, C. MacAulay, B. Palcic, and D. I. McLean, "A Computerized Auto fluorescence and Diffuse Reflectance Spectroanalyser System for in vivo Skin Studies", *Phys. Med. Biol.* **38**, 231-240 (1993).

[21] Y. P. Sinichkin, S. P. Uts, and E. A. Pilipenko, "Spectroscopy of Human Skin in vivo: 1. Reflection Spectra", *Physical Optics* **80**, 228-234 (1996).

[22] P. Bjerring, and P. H. Andersen, "Skin Reflectance", *Spectrophotometry. Photodermatol. Photoimmunol. Photomed.* **4**, 167-171 (1987).

[23] R. R. Alfano, S. G. Demos, and S. K. Gayen, "Advances in Optical Imaging of Biomedical Media", *Imag. Brain Struc. Func.*, **820**, 248-270 (1997).

[24] T. Gibson, " Physical Properties of Skin" in *Plastic Surgery Vol.1 General Principles.* ed. by J. G. McCarthy, W. B. Saunders Co., Philadelphia pp. 207-220 ( 1990).

[25] C. Cacou, J. M. Anderson, and I. F. K. Muir, "Measurement of Closing Force of Surgical Wounds and Relation to the Appearances of Resultant Scars", *Med. & Bio. Eng. & Comp.* **32**, 638-642 (1994).

[26] C. Cacou, and I. F. K. Muir, "Effects of Plane Mechanical Forces in Wound Healing in Humans", *J. R. Coll. Surg. Edinb.* **40**, 38-41 ( 1995).

[27] W. F. Larabee, G. A. Holloway, and D. Sutton, "Wound Tension and Blood Flow in Skin Flaps", *Ann. Otol. Rhinol. Laryngol.* **93**, 112-115 (1984).

[28] H. R. Chaudhry, B. Bukiet, M. Siegel, T. Findley, A. B. Ritter, and N. Guzelsu, "Optimal Patterns for Suturing Wounds", *J. Biomechanics* **31** , 653-662 (1998).

[29] B. Chretien-Marquet, V. Caillou, D. H. Brasnu, S. Bennaceur, and T. Buisson, "Description of Cutaneous Excision and Suture Using a Mathematical Model", *Plastic and Reconstructive Surgery* **103,** 145-150, (1999).

[30] D. M. Flynn, G. D. Peura, P. Grigg, and A. H. Hoffman, "A Finite Element Based Method to Determine the Properties of Planar Soft Tissue", *J. of Biomechanical Engineering* **120**, 202-210, (1998).

[31] P. H. DeHoff, and J. E. Key, "Application of the finite Element Analysis to Determine Forces and Stresses in Wound Closing", *J. of Biomechanics* **14,** 549-554 (1981).

[32] A. Manios, J. Katsantonis, A. Tosca, C. N. Skulakis, and D. Tsiftsis, "The Finite Element Method ads a Research and Teaching Tool in the Analysis of Local Skin Flaps", *Dermatological Surgery* **22**, 1029-1034, (1996).

[33] A. Vexler, I. Polyansky, and R. Gorodetsky, "Evaluation of Skin Viscoelasticity and Anisotropy by Measurement oh Speed of Shear Wave Propagation with Viscoelasticity Skin Analyzer", *J. of Investigative Dermatology* **113**, 732-739 (1999).

[34] Y. Lanir, and Y. C. Fung, "Two-dimensional Mechanical Properties of Rabbit Skin-I. Experimental System", *J. of Biomechanics* **7**, 29-34 (1974).

[35] Y. Lanir, and Y. C. Fung, "Two-Dimensional Mechanical Properties of Rabbit Skin-II. Experimental Results", *J. of Biomechanics* **7**, 171-182, (1974).

[36] M. Viatour, F. Henry, and G. E. Pierard, "A Computerized Analysis of Intrinsic Forces in the Skin", *Clinical & Experimental Dermatology* **20**, 308-312 (1995).

[37] H. Chaudhry, B. Bukeit, T. Findley, and A. Ritter, "Evaluation of Residue Stress in Rabbit Skin and the Relevant Material Constants", *J. Theor. Biol.* **192**,191 (1998).

[38] M. Weston, K. Rhee, and J. Tarbell, "Compliance and Diameter Mismatch Affect the Wall Shear Rate Distribution Near an end to end Anastomsosis", *J. Biomech.* **29**,187 (1996).

[39] S. Sidhu, R. Stanton, S. Shahidi, J. Chu, S. Chew, and P. Campbell, "Initial Experience of Vocal Cord Evaluation using Grey-scale, Real-time, B-mode Ultrasound", ANZ Journal of Surgery, **71**, 737-739, (2001).

[40] Y. Lanir, and Y. C. Fung, "2-D Mechanical Properties of Rabbit Skin – Experimental System", *J. Biomech.* **7**, 29-34 (1998).

[41] J. Downs, H. R. Halperin, J. Humprey, and F. Yin, "An Improved Video-based Computer Tracking System for Soft Tissue Biomaterials Testing", *lEEE Trans. Biomed. Engng.* **37**, 903-907 (1990).

[42] A. A. Derwin, L. J. Soslowsky, W. D. K. Green, and S. H. Elder, "A New Optical System for Determining of Deformation and Strains: Calibration Characteristics and Experimental Results", *J. Biomech.* **27**, 1277-1285 (1994).

[43] K. M. Kwan, H-C. L. Timothy, and S.L-Y. Woo, "On the Viscoelastic properties of the Anteromedial Bundle of the Anterior Cruciate Ligament", *J. Biomech.* **26**, 447-452 (1993).

[44] M. O'Donnell, A. Skovoroda, B. M. Shapo, and S. Y. Emelianov, "Internal Displacement and Strain Imaging using Ultrasonic Speckle Tracking", *lEEE Trans. Ultrason. Ferroelect. Freq. Cont.* **41**, 314 (1994).

[45] L. Pan, L. Zan, and F. S. Foster, "Ultrasonic and Viscoelastic Properties of Skin under Transverse Mechanical Stress in vitro", *Ultrasound Med. Biol.* **24**, 995 (1998).

[46] I. Sarkany, "Method for Studying the Microtopography of Skin", *British J. cf Dermatology* **74**, 254-259 (1962).

[47] T. H. Cook, "Profilometry of the Skin: A useful tool for the Substantation of Cosmetic Efficacy", *J. Soc. Cf Cosmetic Chemists* **31**, 339-359 (1980).

[48] M. Assoul, T. Galal, and J. Mignot, " Cutaneous Relief Measurement using a Wide Range Automatic Profilometer", *Bioeng. & the Skin* **3**, 109-112 (1987).

[49] L. Thrane, "Optical Coherence Tomography: Modeling and Applications", Ph.D. thesis, Technical University of Denmark, Risø National Laboratory, May 2001, pp. 76.

[50] J. M. Bennett, "Measurement of the rms Roughness, Autocovariance Function and other Statistical Properties of Optical Surfaces using an FECO Scanning Interferometer", *Appl. Opt.* **15**, 2705 (1976).

[51] P. Beckmann, "Scattering of Light by Rough Surfaces", Progr. Opt. **6**, 55 (1967).

[52] P. Beckmann, and A. Spizzichino, "The Scattering of Electromagnetic Waves from Rough Surfaces", Pergamon, Oxford (1963).

[53] R. A. Sprague, "Surface Roughness Measurement using White Light Speckle", *Appl. Opt.* **11**, 2811 (1972).

[54] J. Ohtsubo, H. Fujii, and T. Asakura, "Surface Roughness Measurement by using Speckle Pattern", *Jap. J. Appl. Phys. Suppl.* **14(1)**, 293 (1975).

[55] A. J. Welch, and M. J. C. van Gemert, "Optical-Thermal Response of Laser-Irradiated Tissue", Plenum, New York, 1995, pp. 5.

[56] A. G. Ferdman and I. V. Yannas, "Scattering of Light from Histologic Sections: A New Method for the Analysis of Connective Tissue," *J. Invest. Dermatol.*, **100,** 710–716 (1993).

[57] B. Jahne, "Digital Image Processing: Concept, Algorithms, & Scientific Applications", 4th ed., Springer, 1997, Chap 1-8 and 10-11.

[58] Mosby's Medical Encyclopedia CDROM Ver.1.0 for Windows, The Times Mirror Co.

[59] R. R. Anderson and J. A. Parrish, "The optics of human skin," *J. Invest. Dermatol.*, **77,** 13–19 (1981).

[60] V. V. Tuchin, "Lasers and Fiber Optics in Biomedicine," *Laser Phys.*, **3,** 767–820 (1993).

[61] E. Hecht, *Optics*, 3rd ed. Addison Wesley, Reading, Mass., 1997.

[62] B. D. Cameron, M. J. Rakovic, M. Mehrubeoglu, G. Kattawar, S. Rastegar, L. V. Wang, and G. L. Cote, "Measurement and Calculation of the Two-dimensional Backscattering Mueller Matrix of a Turbid Medium," *Opt. Lett.* **23,** 485–487 (1998).

[63] N. Guzelsu, T. W. Findley, J. F. Federici, H. R. Chaudhry, and A. B. Ritter, "Apparatus and Method for Noninvasive Measurement of Stretch," U.S. Patented 1998.

[64] P. L. Williams and R. Warwick, eds., *Gray's Anatomy*, 36th ed. Saunders, Philadelphia, Pa., 1980, pp. 1216–1226.

[65] J. Ferguson and J. C. Barbenel, "Skin Surface Patterns and the Directional Mechanical Properties of the Dermis," in *Bioengineering and the Skin*, R. Marks and P. A. Payne, eds. MTP, Lancaster, Pa., 1981, pp. 83–92.

[66] M. Assoul, M. Zahidi, P. Corcuff, and J. Mignot, "Three-dimensional Measurements of Skin Surface Topography by Triangulation with a New Laser Profilometer," *J. Med. Eng. Technol.* **18,** 11–21 (1994).

[67] H. Miyazaki, Y. Hasegawa, and K. Hayashi, "A Newly Designed Tensile Tester for Cells and its Application to Fibroblasts - Investigations with the Scanning Acoustic Microscope", *J. of Biomech.*, **33**, 97-104(8) (2000).

[68] A. R. Weeks Jr, "Fundamentals of Electronic Image Processing", IEEE Press 1996, Chap 3 and 6.

[69] C. B. Mcvay, "Surgical Anatomy", 6th ed. Vol. 1, W. B. Saunders Co., 1984, pp. 486.

[70] A. R. Moritz, "The Pathology and Pathogenesis of Cutaneous Burns: An Experimental Study", *Am. J. Pathol.* **23**, 915 (1947).

[71] A. T. Schomacker, A. Torri, D. R. Sanison, R. L. Sheridan, and N. S. Nishioka, "Biodistribution of Indocyanine Green in a Porcine Burn Mode: Light and Flourescene Microscopy", J. Trauma, **43**, 813 (1997).

[72] E. E. Peacock, Jr., and I. K. Cohen, "Wound Healing," in *Plastic Surgery Volume 1: General Principles*, J. G. McCarthy, ed. Saunders, Philadelphia, Pa., 1990, pp. 161–181.

[73] R. K. Daniel and C. L. Kerrigan, "Principles and Physiology of Skin Flap Surgery," in *Plastic Surgery Volume 1: General Principles*, J. G. McCarthy, ed. Saunders, Philadelphia, Pa., 1990, pp. 275–328.

[74] L. C. Argenta and E. D. Austad, "Principles and Techniques of Tissue Expansion," in *Plastic Surgery Volume 1: General Principles*, J. G. McCarthy, ed. Saunders, Philadelphia, Pa., 1990, pp. 475–507.

[75] S. L. Jacques, C. A. Alter, and S. A. Prahl, "Angular Dependence of He-Ne Laser light scattering by Human Dermis", *Lasers in Life Sciences* **1**, 309 (1987).

[76] T. Asakura, "Speckle Metrology", Academic press, Inc , 1978, Chap. 3.

[77] C. A. Glasbey, "Image Analysis for the Biological Sciences, Statistics in Practice", Wiley & Sons, 1998, Chap 5.

[78] S. Umbaugh, "Computer Vision and Image Processing", Prentice Hall, 1998, Chap 1-4.

[79] J. M. Pereira, J. M. Mansour, B. R. Davis, "Dynamic Measurement of the Viscoelastic Properties of Skin", *J. of Biomech.* **24**, 157-162 (1991).

[80] R. Reihsner, B. Balogh, E. J. Menzel, "Two Dimensional Elastic Properties of Human Skin in Terms of an Incremental Model at the In-vivo Configuration", *Medical Engineering and Physics* , **17**, 304-313 (1995).

[81] S. Makki, J. C. Barbenel, P. Agache, "A Quantitative Method for the Assessment of the Microtopography of Human Skin", *Acta Dermatovener (Stockholm),* **59,** 285-291 (1979).

[82] D. Iliev, U. Hinnen, P. Elsner, "Skin Bioengineering Methods in Occupational Dermatology", *Skin Bioengineering Techniques and Applications in Dermatology and Cosmetology.* Current Problem in Dermatology. Ed. By Elsner P, Barel AO, Brardesca E, Gabard B, SerupJ. , Basel, Karger, **26**, pp. 145-150 (1998).

[83] P. Elsner, "Skin Elasticity", *Bioeng. of the Skin: Methods and Instr.* Ed.by Berardesca E, Elsner P, Wilhelm K P, Maibach HI. CRC Press Baco Raton, 1995, pp.53-64.

[84] A. O. Barel, R. Lambrecht, P. Clarys, "Mechanical Function of the Skin: State of the Art", *Skin Bioeng. Tech. & Appl. in Dermatology and Cosmetology,* Current Problem in Dermatology. Ed. By Elsner P, Barel AO, Brardesca E, Gabard B, SerupJ. , Basel, Karger, **26**, 1998, pp. 69-83.

[85] N. Nikkels-Tassoudji, F. Henry, C. Pierard-Franchimont, G. E. Pierard, "Computerized Evaluation of Skin Stiffening in Scleroderma", *Eurpean J.l of Clinical Invest.* **26**, 457-460 (1996).

[86] H. Dobrev, "In vivo Study of Skin Mechanical Properties in Scleredema of Buschke", *Acta Derm. Venereol.* **28,** 103-106 (1998).

[87] S. Robbins, V. Kumar, "Basic Pathology", 4th ed., W. Saunders, Philadephia, 1987.

[88] F. N. Ghadially, "Ultrastructural Pathology of the Cell and Matrix", 3rd ed., Butterworth, Boston, 1988.